Room Temperature Sulfur Battery Cathode Design and Processing Techniques

By

Rachel Carter

Dissertation

Submitted to the Faculty of the

Graduate School of Vanderbilt University

in partial fulfillment of the requirements

for the degree of

DOCTOR OF PHILOSOPHY

in

Mechanical Engineering

May, 2017

Nashville, Tennessee

Approved:

Cary Pint, Ph.D.

Rizia Bardhan, Ph.D.

Peter Pintauro, Ph.D.

Jason Valentine, Ph.D.

Greg Walker, Ph.D.

Dedication

This dissertation is lovingly dedicated to my grandfather, Donald L. Kinser, Ph. D., a constant source of inspiration and unwavering support.

ACKNOWLEDGMENTS

First and foremost I would like to thank my advisor, Dr. Cary Pint, for carefully and patiently molding me into the researcher I am now. Your passion for new ideas truly inspires me, and your incredible work ethic and skill in technical communication continually motivates me to improve myself. Thank you for assisting in the successful publication of my work. I couldn't have done it without you. Further, I thank my dissertation committee: Dr. Rizia Bardhan, Dr. Peter Pintauro, Dr. Jason Valentine and Dr. Greg Walker for agreeing to give their time for the improvement of my dissertation and for their helpful feedback on my research over the past 4 years.

I would like to thank the members of the Pint lab, past and present, who have engaged in invaluable scientific discussions and contributed experimentally to my work. I'd specifically like to thank Dr. Shahana Chatterjee for introducing me to the art of transmission electron microscopy, a characterization technique that I thoroughly enjoyed throughout my graduate career, Dr. Landon Oakes for help in developing the isothermal vapor infiltration technique that enabled much of this dissertation, Adam Cohn for helping me fabricate my first battery, Anna Douglas for allowing me to fumble through training you as a grad student after completing only one year myself and for becoming one of my very best friends, Mengya Li for always brightening my day and delivering a satisfying reaction to every situation and for diligently carrying on my legacy of sulfur batteries in the group, Nitin Muralidharan for always providing the best constructive criticism and for many thought provoking conversations, and Keith Share, Kate Moyer and Deanna Schauben for their wonderful friendship. Further I'd like to thank Evan Gordon, high

school student, who co-authored a publication with me in my second year and Dennis Ejorh, NSF REU, who assisted in material fabrication for the demonstration of some of the lab's first sulfur batteries.

Further, I would like the to thank Dr. Rizia Bardhan for graciously allowing the use of her laboratory equipment, instrumental to much of my dissertation work, and for her invaluable mentorship during my graduate career. I would also like to thank the Bardhan group for sharing their workspace and helping with the use of their equipment. I would especially like to thank May Ou for bringing welcomed distractions to our lab and for being such an incredible friend.

I extend thanks to the Maschmann group for developing hierarchical carbon nanotube scaffolds, utilized for a portion of this work.

I thank the VINSE staff: Dr. Hmelo, Dr. Schmidt, Dr. Koktysh, and Dr. McBride for training me and supporting my use of the VINSE facilities, and VINSE for supporting me with TN Score funding and a graduate fellowship.

Thank you to my family for their emotional and financial support throughout my lengthy career as a student. Thank you to my grandfather, Dr. Donald Kinser, for inspiring me to be a scientist and to stick it out for the Ph.D. Thank you to my mother, Cynthia Kinser, J.D. for teaching me the value of education and always supporting my every endeavor.

Finally, I extend the deepest thanks to my fiancé, Nicholas Murray. for supporting me through the ups and downs of graduate school and for teaching me not to take myself so serious. I'm forever grateful to have you in my life and can't wait to begin our new chapter together in Washington D.C.

TABLE OF CONTENTS

Page

LIST OF TABLES

Table Page

LIST OF FIGURES

LIST OF PUBLICATIONS

Portions of this dissertation have been drawn from the following publications:

1. R. Carter, L. Oakes, A. Cohn, J. Holzgrafe, H.F. Zarick, S. Chatterjee, R. Bardhan, and C.L. Pint, "Solution assembled single walled carbon nanotube foams; Superior performance in supercapacitors, lithium ion, and lithium air batteries," Journal of Physical Chemistry C 118, 20137-20151 (2014).

2. R. Carter, S. Chatterjee, E. Gordon, K. Share, W.R. Erwin, A.P. Cohn, R. Bardhan, and C.L. Pint, "Corrosion resistant three-dimensional nanotextured silicon for water photo-oxidation," Nanoscale 7, 16755-16762 (2015).

3. R. Carter, D. Ejorh, K. Share, A.P. Cohn, A. Douglas, N. Muralidharan, T. Tovar, and C.L. Pint, "Surface oxidized mesoporous carbons derived from porous silicon as dual polysulfide confinement and anchoring cathodes in lithium sulfur batteries," Journal of Power Sources 330, 70-77, (2016).

4. R. Carter, L. Oakes, A. Douglas, N. Muralidharan, A.P. Cohn, and C.L. Pint, "A sugar derived room temperature sodium sulfur battery with long term cycling stability," Nano Letters, 17, 1863-1869 (2017)

5. R. Carter, L. Oakes, N. Muralidharan, A.P. Cohn, A. Douglas, and C.L. Pint, "Polysulfide anchoring mechanism revealed by atomic layer deposition of V2O5 and sulfur filled carbon nanotubes for lithium-sulfur batteries," ACS Applied Materials and Interfaces, 9, 7185-7192 (2017).

6. R. Carter, L. Oakes, N. Muralidharan, and C.L. Pint, "Isothermal sulfur condensation into carbon scaffolds: Improved loading, performance, and scalability for lithium sulfur battery cathodes," accepted, Journal of Physical Chemistry C (2017).

7. R. Carter, B.Davis, L. Oakes, M. Maschmann, and C. L. Pint, "Site-Selective Vapor Infiltration of Hierarchical Carbon Nanotube Arrays for High Areal Capacity Lithium-Sulfur Battery Cathodes," submitted to Nanoscale.

8. R. Carter, N. Muralidharan, A. P. Cohn, B. Schmidt, B. Maruyama, M. Durstock, and C. L. Pint, "Core/Shell Nickel/Nickel Hydroxide Nanofoam for High Performance Pseudocapacitve Electrodes," in preparation.

9. R. Carter, A. P. Cohn, N. Muralidharan, L. Oakes, K. Share, and C. L. Pint, "*In-situ* Raman and UV-vis spectroscopic investigation of discharge behavior in room temperature sodium sulfur batteries," in preparation.

Chapter 1

Introduction

1.1 Motivation

1.1.1Broader Context

As the population grows and energy demand increases, climate change threatens causing energy storage research to focus on fulfilling the requirements of two major energy sectors with next generation batteries: (1) portable energy and (2) stationary storage.[1] Where portable energy can decrease transportation-related harmful emissions and enable advanced next-generation technologies,[1] and stationary storage can facilitate widespread deployment of renewable energy sources, alleviating the demand on fossil fuels and lowering emissions.[2]

Portable energy can enable zero-emission transportation and can deploy portable power in advanced electronics across fields including medical and defense.[3] Currently fully battery powered cars are limited in driving distance, which is dictated by the energy density and weight of the state-of-the-art Li-ion battery, and similarly advancement of portable electronics is significantly hindered by heavy batteries with short charge lives. In attempt to enable advanced portable energy, significant research is aiming to improve the conventional Li-ion batteries and explore beyond Li-ion battery chemistries[4] with the primary goal of demonstrating higher energy density to enable lighter weight cells with longer battery life.

Further, with the inherent intermittency challenges of our most prominent renewable energy sources, wind and solar, discovery of batteries capable of cost effectively and reliably balancing the generation of the renewable energy sources with the real-time energy demand is required for grid scale viability.[2] Stationary storage will provide load leveling to renewable resources by storing excess energy at peak generation and delivering stored excess during periods of lower generation. This application demands highly abundant, low-cost active materials and long-term cycle stability, since infrastructure costs (combined with the renewable) must compete with burning natural gas.[4] Development of a battery with these characteristics will require exploration of chemistries beyond the Li-ion battery for a system consisting of low cost active materials and promising device performance.

1.1.2 Limitations of Advanced Li-ion Batteries

The conventional Li-ion battery consists of a lithium metal-oxide cathode (lower energy electrode) and graphite anode (higher energy electrode) separated by an electron-inhibiting, ion-transporting polymer separator wetted with a lithium salt containing organic, liquid electrolyte (Figure 1.1). The graphite and lithium metal oxide components are typically slurry cast into electrodes from a powder form with conductive carbon additives and polymer binders.

As the device, fully discharged on fabrication, is externally charged with constant current (constant flow of electrons into the high energy anode), the cathode is oxidized and Li^+ ions shuttle across the cell to intercalate into the graphite anode, where the ion is reduced and stored.[3] The balanced charge reaction for the popular lithium cobalt oxide (LCO) system is shown as equation 1.

$$6C + 2LiCoO_2 \rightarrow LiC_6 + 2Li_{0.5}CoO_2 \quad (1)$$

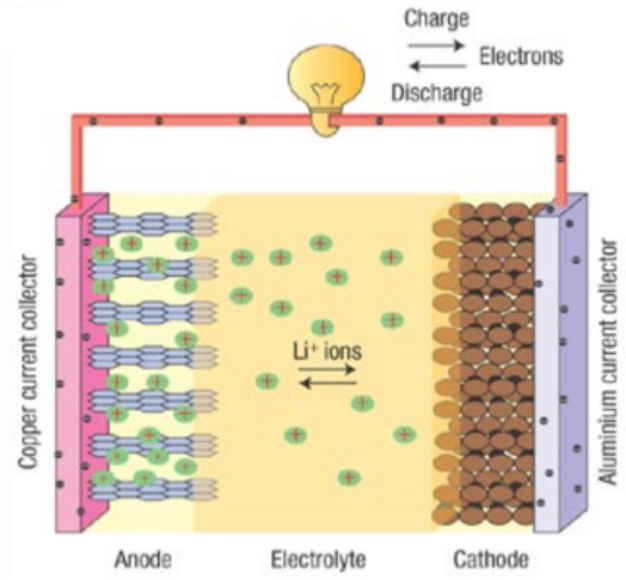

Figure 1.1- Schematic representation of a conventional Li-ion battery with metal oxide cathode and graphite anode separated by lithium salt containing electrolyte. Image reproduced from Scrosati *et al*.[5] with permission from Nature Publication Group.

This system, possessing layered structures at both electrodes is referred to as an intercalation battery and subsequently requires significant mass and volume in the cell at each electrode to host the shuttling Li^+ ions, limiting the cell's mass and volume performance (see Appendix A for details on theoretical performance and battery characterization). Specifically in the LCO system, on fabrication, 1 lithium is stored in every heavy metal oxide unit but only half of these are extracted during charge, to enable structural rigidity (equation 1). Further, at complete charge, only 1 lithium is stored for every six carbon atoms. However, the intercalation mechanism enables a high degree of stability with commercial cells demonstrating over 15,000 cycles.

The energy density of the Li-ion battery (theoretical maximum of 387Wh/kg for the conventional cell) can be enhanced by realizing higher operating voltage metal oxides at the cathode or replacing the graphite host at the anode with smaller, lighter-weight materials.[1] High voltage cathodes that can deliver reaction voltages approaching 5V (conventional 3-4V) can enhance energy density by about 30% but struggle with electrolyte stability. At the anode, the most commonly investigated graphite replacement is low voltage, alloying silicon, which can store 3.5 Li-ions per silicon atom but is challenged by brittle fractures, as a result of the 300% volume expansion, limiting the cyclability.[1] Alternatively, researchers are exploring the complete elimination of the anode host by enabling pristine lithium metal plating at the anode from the ions initially stored in the cathode.[6] This approach is limited by challenges with reversibility and safety of the pure alkali metal anode. However, even with the complete elimination of anode material in the conventional Li-ion battery, only a two-fold increase in cell energy density can be obtained, since the mass and volume specific performance of the cell is ultimately limited by the metal oxide cathode. Although the 2X improvement (~750Wh/kg) will prove exceedingly valuable in the immediate future,[7] significantly greater energy density enhancement is demanded for batteries to truly compete with the internal combustion engine (>13,000 Wh/kg) and enable advanced portable applications like practical all-electric vehicles and aerospace applications.[8] Further, when considering lowering the cost of the Li-ion battery, the system is again limited by the metal oxide cathode, that typically contains expensive transition metals and requires high temperature solid-state reaction synthesis.[9]

1.1.3 Sulfur Battery Chemistries

Considering the emerging beyond Li-ion battery chemistries (Figure 1.2), sulfur conversion batteries show the most promise for effectively demonstrating the traits desired for the two most demanded applications of batteries: portable energy and stationary storage.[10] For portable applications lithium sulfur (Li-S) batteries will provide impressive energy density enhancement, and for stationary storage, sodium sulfur (Na-S) batteries will enable exceptionally low active material cost.

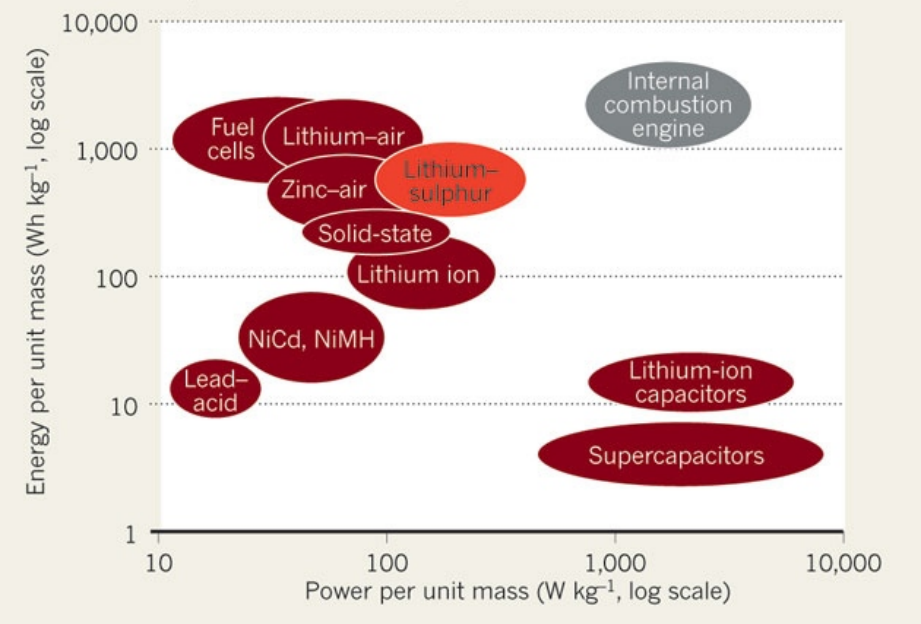

Figure 1.2- Ragone comparison of various popular energy storage technologies revealing lithium sulfur batteries as a promising candidate to replace the Li-ion battery and compete with the combustion engine. Image reproduced from Noorden *et al*. [11] with permission from Nature Publication Group.

Lithium sulfur batteries have emerged as the most promising next generation battery to succeed the Li-ion battery, boasting over 6X increase in energy density (2567 Wh/kg vs. 387 Wh/kg) and significant advancements over the past 10 years, enabling the first few promising commercial demonstrations of the batteries (Sion Power, Oxis Energy, Orange Energy).[3] Although the lithium-air battery is lauded for the highest theoretical energy density (11,400 Wh/kg), approaching that of burning fossil fuels (>30X the Li-ion), it, unlike Li-S, remains far from commercial viability with minimal demonstration of cyclability in the literature.[11] Replacing the Li-ion battery in a state-of-the-art battery-powered car with a Li-S battery of the same weight, will enhance driving distances to 1500 miles, enabling 24 hours of uninterrupted travel between charges (at ~60mph), significantly enhancing the practicality of battery powered vehicles. Although high sulfur conversion has been demonstrated with Li-S to support this estimated driving distance enhancement, efforts remain to lower the passive host material mass and volume and to enhance the cycle life of the cells to prevent need for frequent battery replacement.[12]

The 6X increase in energy density, enabled by Li-S batteries, will allow deployment of portable energy with significantly reduced weight or significantly enhanced battery life. This thesis focuses on demonstrating close to theoretical behavior of the lithium sulfur system with minimal host material to realize the full energy density enhancement promised by the conversion chemistry.[13] Further, although cost is less of a concern in these portable applications, the use of low-cost and environmentally friendly sulfur as active material in the system is desirable, and if the system is further modified to replace the alkali ion with the larger but 14X more abundant sodium ion, the resulting

battery will function on exceptionally low cost active materials, providing the fundamental requirement of grid-scale stationary storage.[14]

The sodium-sulfur system promises half the energy density of the lithium-sulfur system, as a result of the larger ion size, but still possesses 3X the theoretical energy density of Li-ion (1400 vs. 387 Wh/kg).[10] Here the low raw materials cost of the sodium-sulfur system is fundamentally ideal for a grid scale application, so demonstration of reliability is favored to dramatic energy density enhancement.[4] Long cycle life, low cost room-temperature sodium sulfur batteries have not yet been obtained because of significant cell-level challenges, limiting publications on this system to less than 50 to date. However, interest in this system has rapidly accelerated recently with the demand for stationary storage, and it is speculated that understanding of alkali sulfur conversion, gained from the Li-S system, can enable more rapid development of the room temperature Na-S battery. Based on these system-level assessments, my research enables high energy density lithium sulfur batteries with acceptable cycle life for portable applications and reliable, ultra-long cycle life, room-temperature sodium-sulfur batteries for stationary storage.

1.2 Lithium Sulfur Batteries

1.2.1 Mechanism

The lithium sulfur (Li-S) battery, which is mechanistically different than the intercalation Li-ion battery, is referred to as a conversion battery, since chemical bonds are formed and broken in each cycle. In its most primitive form, the battery possesses a

lithium metal anode and elemental sulfur cathode isolated by a polymer separator wetted with lithium salt containing, organic, liquid electrolyte (Figure 1.3).[15] This system is fully charged on fabrication (lithium in the high energy state at the metallic anode), and as it is discharged, or constant current is drawn from the anode, the lithium metal is oxidized, releasing Li^+ ions into the electrolyte. The Li^+ ions shuttle across the cell to the sulfur cathode, where each sulfur, reduced to S^{2-}, is fully converted to Li_2S. The balanced discharge reaction is shown as equation 2.

$$2Li + S \rightarrow Li_2S \qquad 2$$

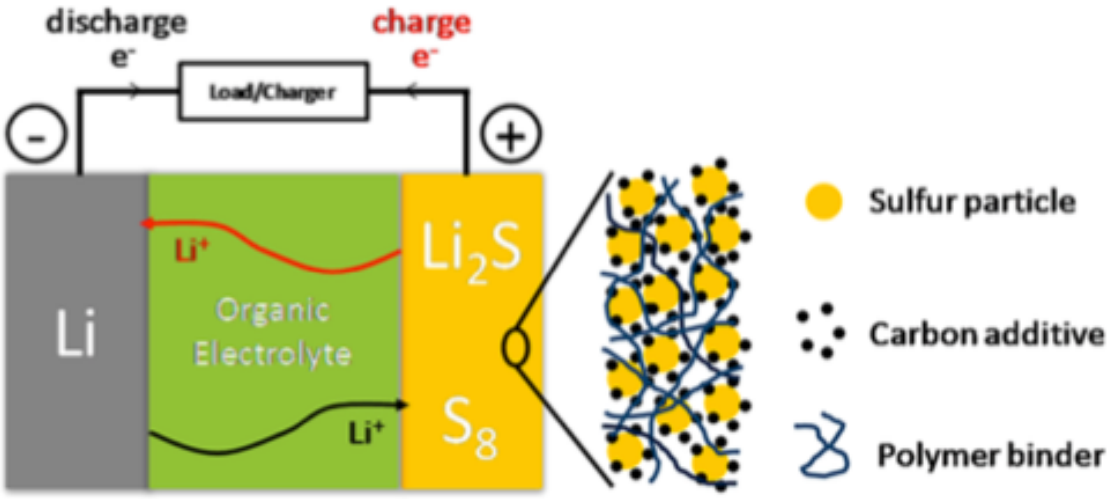

Figure 1.3- Schematic representation of the lithium sulfur battery with charge process color-coded red and discharge process black. Image reproduced from Manthriam et al.[15] with permission from the American Chemical Society.

The conversion behavior enables significantly enhanced energy density (2567 Wh/kg compared to 387 Wh/kg in Li-ion) with two electrons transferred for every low-density sulfur atom or two lithiums stored at each sulfur atom.[3]

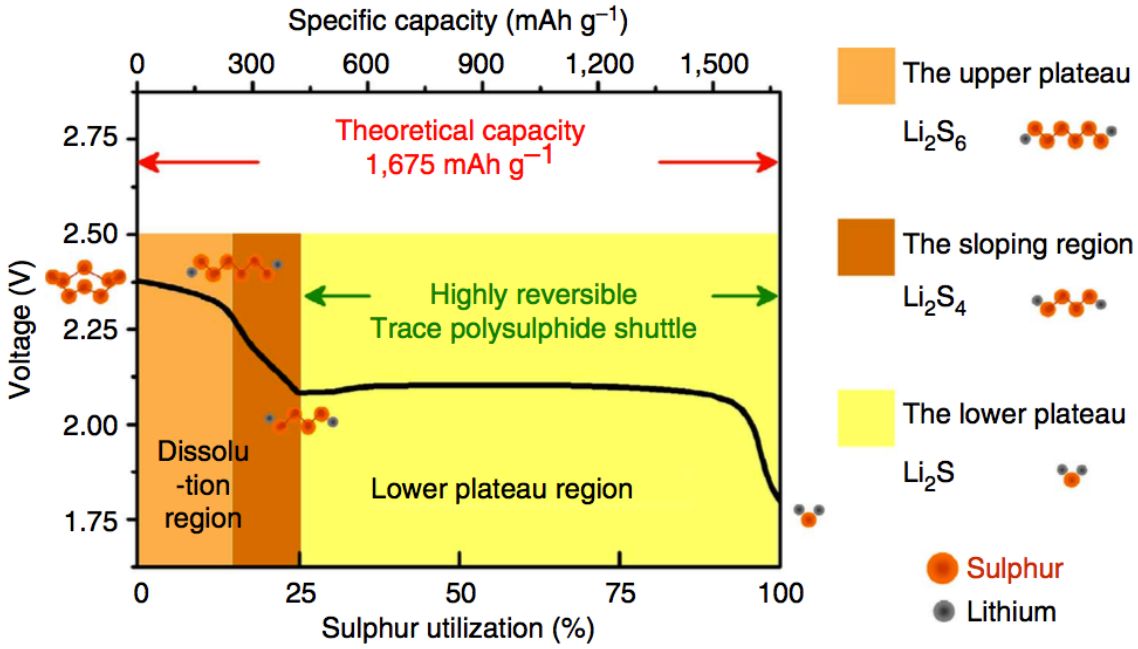

Figure 1.4- Lithium sulfur battery discharge behavior with two distinct voltage plateaus as polysulfide products form where notably the produces formed in the initial plateau are soluble in the battery electrolyte and the final products in the lower voltage region are insoluble. Image reproduced from Su *et al*.[4] with permission from Nature Publication Group.

Since elemental sulfur inherently arranges in S_8 rings or chains, the conversion is observed incrementally at each member of the chain until the final product is produced (Li_2S_8, Li_2S_6, Li_2S_4, Li_2S_2, Li_2S), resulting in the observation of distinct intermediate discharge products referred to as polysulfides.[3] These intermediate products give rise to the characteristic two-step discharge curve, observed with Li-S batteries (Figure 1.4), due

to differing solubility of the products in the system electrolyte. The first 3 products (Li_2S_x $8 \leq x \leq 4$) are soluble in the battery electrolyte and the final products (Li_2S_y $4 < y \leq 2$) are insoluble.[16] Explanation of the battery discharge curve and complete battery characterization is found in the Appendix A.

1.2.2 Challenges

Although the conversion behavior enables high theoretical energy density, poor energy retention over cycling is the most challenging feature of a lithium sulfur battery system. If sulfur is simply slurry cast with conductive additives and polymer binders (Figure 1.3) in the way conventional Li-ion battery electrodes are fabricated, rapid decay is observed with complete device failure in as little as 50 cycles.[17] This failure is primarily attributed to the solubility of the high-order polysulfides formed in the upper voltage plateau of the discharge (Figure 1.4). Without proper confinement and effective charge transfer to the solubilized species, the polysulfides can dissipate from the electrode and become electrically isolated or worse- deposit at the lithium metal anode during charging, where spontaneous conversion to insulating Li_2S deactivates the metallic anode.[18] This polysulfide shuttling failure mechanism requires careful electrode design, where material consideration and innovative processing techniques prove exceedingly valuable for providing the cycle life stability required for commercial viability.

The electrically insulating nature of the active sulfur and poor cycling retention demonstrated by the system requires use of a passive material to host the active species through the conversion process, and the two-step discharge behavior dictates the two main design considerations for the host. The solubility of the upper voltage discharge products (high order polysulfides) requires a host capable of containing the solubilized species

close enough to the host for the incremental charge transfer to occur and for prevention of active material loss. The insulating nature of the insoluble, lower voltage discharge product (Li_2S), which is 80% larger than the sulfur predecessor, requires a highly conductivity, high surface area host. Here the host must effectively accommodate deposition of the large volume product and deliver electrical current to the entirety of the electrode, for complete reversal on the subsequent charge.[16] Further, since host material will remain passive to the energy storage mechanism, the weight and volume contribution should be kept as low as possible.[18]

1.2.4 Previous Research

With considerable interest in enabling longer cycle life Li-S batteries, several electrode design strategies have emerged including: externally fixed interlayers,[19-20] microporous confinement,[21-24] nanoscale encapsulation,[25-41] and polysulfide binding.[42-46] These strategies are illustrated in Figure 1.5. The first of these design strategies deploys an additional component in-between the cathode and battery separator, meant to trap solubilized high order polysulfide species to prevent anode deactivation, as shown in Figure 1.5A.[19-20] However the interlayer component introduces excess mass and weight to the cell and does not provide charge transfer to the species moved from the host to the interlayer, deactivating this material from the system.

The second main approach utilizes microporous confinement (Figure 1.5B), where sulfur is stored in the interior of pores ~0.5nm in diameter, confining sulfur chain lengths below S_4 for complete elimination of high order polysulfide production during operation.[21-24] Here the smaller chain sulfur still fully converts to the Li_2S product, ensuring the same theoretical cell capacity, but elimination of the upper voltage reaction

lowers the cell energy about 10%. This system delivers exceptional cyclability, but fabrication of the composite is difficult, typically requiring high temperature (>400°C) vacuum processing with sulfur vapor over long durations (>1hr). Additionally, this strategy suffers from low mass loadings of sulfur (<50 wt.% sulfur) limiting the mass specific performance of the devices.

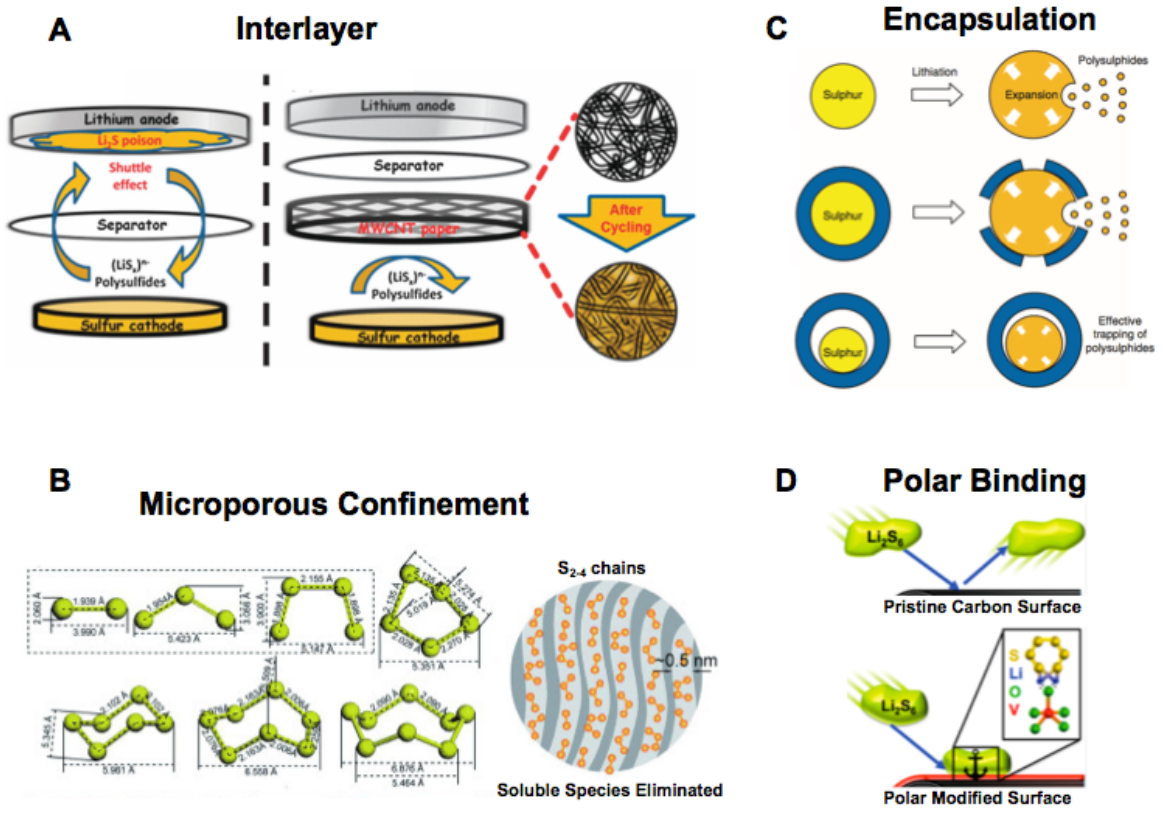

Figure 1.5- Schematic depiction of the four most common polysulfide containing strategies for Li-S cathodes. **A.** Image reproduced from Su *et al*.[47] with permission from Royal Chemistry Society. **B.** Image reproduced from Xin *et al*.[23] with permission from Nature Publication Group. **C.** Image reproduced from Seh *et al*.[48] with permission from Nature Publication Group. **D.** Image reproduced from Carter *et al*.[49] with permission from Nature Publication Group.

The next major approach focuses on encapsulating sulfur in various conductive materials in unique ways, including graphenic wrapping[25, 39, 41] or synthesis of complex nanostructures like the yolk-shell (Figure 1.5C).[38, 48] However processing for these approaches can prove expensive and not practical for commercial viability. This work builds on some of the most effective encapsulation strategies and enables lower cost processing.

Finally, polysulfide binding illustrated in Figure 1.5D has emerged as one of the most promising Li-S cathode design strategies. The intermediate polysulfide products, produced during device operation, are highly polar in nature and by incorporating proper polarity at the surface of the host, electrostatic binding between the polysulfide and the polar surface can anchor the active material and prevent migration.[38, 43-46] This strategy has proved highly effective and researchers have asserted claim that the stronger the electrostatic binding in the system, the better the battery will perform.[45] The materials exhibiting the best electrostatic binding are transition metal oxides, requiring careful consideration for their less conductive and dense material nature. The community, as well as portions of this thesis, continues to focus on developing lightweight sulfur host materials capable of high performance and long cycle stability using feasible processing techniques that build on the successes of these four major cathode design strategies.

Additionally with the demonstration of impressive device performance with various designs, the field began attempting the demonstration of packaging scale loadings, to further the commercial viability of the Li-S battery. Although mass specific performance 5X that of Li-ion has be demonstrated by many types of Li-S cathodes, these batteries are challenged by low areal loadings.[12] Commercial Li-ion batteries deliver 3-5

mAh/cm^2 in areal capacity but labscale Li-S batteries typically deliver less than 2 mAh/cm^2, since thicker assemblies (μm-mm) of the sulfur electrodes are severely challenged by conductivity, as critical thicknesses of the insulating active sulfur are surpassed or conductive host electrical interconnection is compromised.[12] Without the ability to increase areal loadings in the Li-S battery, a higher ratio of packaging materials will be required, increasing price, weight and volume of the fully fabricated cell, undermining the advances in mass specific performance.[18] Recent literature has explored alternative current collector materials, replacing heavy, expensive metals with carbonaceous mats, and enhanced electrical interconnection with sponge-like hosts or calendaring techniques, that compress the fabricated films in hopes of improving contact.[12]

1.2.5 Experimental Approach

This thesis looks to develop scalable material designs[50] and processing techniques to produce Li-S battery cathodes capable of close to theoretical behavior with minimal host materials and cyclability competitive for commercialization. The general design strategy utilizes lightweight, high surface area carbon host materials arranged in high aspect ratio configurations capable of providing full lithium ion access but slowed migration of soluble polysulfides.

I first approached this challenge by developing a high aspect ratio mesoprorous carbon from inverted, tree-like porous silicon template, as described in Chapter 2.[51] Our research group diligently developed a passivation technique, where the nanoscale features of electrochemically etched porous silicon catalyze a thin conformal layer for graphenic carbon from hot acetylene gas.[52-53] This passivation enables stability of porous silicon in electrochemical environments (aqueous, organic, corrosive, etc.)[54], where it was natively

highly reactive,[55] and allowed demonstration of a range of applications (supercapacitor,[56] battery,[57] photoanode,[58] die-sensitized solar cell counter electrode,[59] etc.[60]). Building on this passivation process, I remove the conformal carbon layer to obtain a lightweight, electrically interconnected mesoporous carbon material possessing the morphological integrity of the porous silicon template. This material is examined as a sulfur cathode according to conventional methods. The cathode demonstrated strong polysulfide confinement but was inadequate in providing optimal electrical conductivity, attributed to poor sulfur uniformity in the structure, by fault of the widely accepted melt infiltration composite processing technique.

Melt infiltration, conventionally used to fabricate sulfur composites,[12] attempts to fill nanoscale features of host materials with bulk liquid, but without control over the diffusion of the liquid, poor uniformity and destruction to electrical interconnections ensues. This destructive nature is evident by the necessity to process melt infiltrated composites with conductive additives and binders, as a result of poor composite conductivity following melt infiltrating. With discovery of this significant limitation in the field, this work aimed to provide a better composite processing technique to enable proper function of fabricated host materials.

Although the carbon nanotube (CNT) was proposed as the best candidate for a sulfur host material to demonstrate high sulfur conversion and strong cyclability,[18] successful demonstration of carbon nanotube-based cathodes has been prevented by challenges with the melt infiltration technique.[61] The carbon nanotube, a single or few layer cylinder of graphenic carbon, demonstrates ultra-high conductivity and surface area with very low density. Further, the high aspect ratio tubular structure can provide

geometric confinement of sulfur in its interior. However, as highly interconnected carbon nanotube electrodes are melt infiltrated with sulfur, the liquid diffuses between crucial tube-tube contacts. Further, infiltration of vertically aligned arrays with bulk liquid causes the array to collapse, destroying the desired mechanical rigidity.[62] Compromise of the highly desired CNT host's properties in the presence of molten sulfur motivates the ability to sulfur infiltrate pre-formed host materials in a nondestructive manner, enabling the full potential of the design and preventing the need for further processing with conductive additives and binders.

Chapter 3 presents the use of electrophoretic deposition (EPD) to rapidly and cleanly assemble optimized carbon nanotube electrodes on various current collector morphologies.[63-68] These electrodes, ideal for use as a sulfur host material, demonstrate high electrical interconnection and high surface area and further deliver impressive performance as pure CNT electrodes in several other device configurations (supercapacitor, Li-ion anode and Li-air cathode). Chapter 4 subsequently reveals the simple isothermal vapor infiltration technique we developed to process these CNT films with sulfur in a nondestructive way.[62, 69]

With realization of a process capable of effectively loading CNTs with sulfur, Chapter 5 explores optimization of the ideal carbon nanotube host to demonstrate remarkable cycle stability.[49] Here, we combine CNT interior confinement of sulfur with an exterior anchoring strategy. An ultra-thin layer of V_2O_5, known to strongly electrostatically bind soluble polysulfides, is applied to the exterior of the CNTs, to enable reactivation of species escaping the CNT ends at the coated CNT exteriors.

Finally, in Chapter 6 the ideal CNT host material is assembled into hierarchical arrays with large vertically aligned CNTs supporting small (single to few layer) CNTs at their sidewalls in a tree-like structure,[70] which is easily and rapidly isothermal vapor infiltrated with sulfur using the process established in chapter 4. The use of the nondestructive vapor processing allows the structure to maintained structural rigidity and electrical accessibility throughout for the demonstration of cathode viable for commercial packaging with high mass and areal specific performance.

The knowledge gained and lessons learned in fabricating Li-S cells, as well as ability to realize high performance hosts with development of improved composite processing methode, motivates exploration of the less successful and less understood sodium sulfur system for promise of grid scale viable energy storage.

1.2 Sodium Sulfur Batteries

1.3.1 The High Temperature Cell

In the 1960s Ford Motor Company proposed an entirely new battery configuration, the high temperature sodium-sulfur battery. Here the active materials are liquid and the ion-transporting separator is solid, where in the conventional sense solid electrodes are separated by liquid electrolyte. The high temperature sodium sulfur (Na-S) cell boasted low cost of active materials and promise of high energy density (760 Wh/kg compared to 387 Wh/kg for Li-ion).[14] The system utilizes the same conversion mechanism observed in the Li-S system but operates with active materials (sodium and sulfur) and all intermediate products in the molten state, requiring cell temperatures above 300°C. Due to the high

operating temperature, a unique cell configuration is used to accommodate cell heating[2] and, as a result of the corrosive nature of the molten materials, expensive and dense ceramic beta-alumina is deployed as a separator (Figure 1.6).

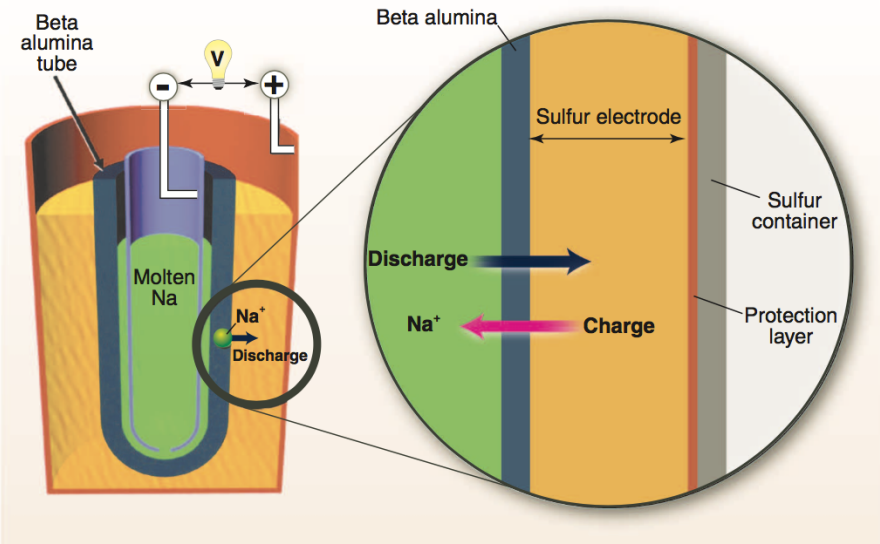

Figure 1.6- Schematic depiction of the high temperature sodium sulfur cell configuration. Image reproduced from Dunn *et al*.[2] with permission from the American Association for the Advancement of Science.

This system does not realize the full potential of sodium sulfur conversion (1400 Wh/kg), since the final discharge product Na_2S (analogous to Li_2S in the Li-S system) exhibits heightened melting point (>1100°C).[10] Therefore the system discharges to the Na_2S_4 sodium polysulfide (balanced discharge reaction- equation 3) and is then subsequently charged back to the sodium and sulfur state.

$$2Na + 4S \rightarrow Na_2S_4 \qquad 3$$

Although the cell energy density is limited to 760 Wh/kg, because of the shortened discharge, and further handicapped by the heavy ceramic separator and energy requirement for cell heating, the system delivers remarkable stability with virtually undetectable performance fade over cycling. With the promise of reliability and in an attempt to enable a lower cost Na-S system, the first room temperature sodium-sulfur battery was demonstrated in 2006, giving promise for the realization of a system viable for grid-scale stationary storage.[14]

1.3.2 Limitations in the Room Temperature Cell

Demonstration of a room temperature sodium sulfur (Na-S) battery has been extremely limited to date with less than 50 publications total, as a result of significant challenges over the Li-S system. Although it's assumed that the system behaves mechanistically the same as the Li-S system and even stores identical charge capacity (1675 mAh/g_S), the larger ion size and differing reactivity present new challenges. The enhanced size of the alkali ion increases the cell volume expansion on complete discharge from 80% to 260%, presenting exceptional challenges in enabling electrical conductivity to the final discharge product.[14] Further the sodium ion suffers from lower reactivity with sulfur and subsequent higher reactivity with electrolyte, causing significant challenges in establishing metallic anode stability.[71]

In the presence of most organic electrolytes the sodium metal surface proves unstable and reacts to form various sodium compounds, which are typically poor ion conductors. As sodium cells are cycled, the metal surface continues to react with the electrolyte until ion transport is completely prohibited. This layer formed at the anode surface is typically referred to as the solid electrolyte interface (SEI). Extensive research

has focused on providing a stable SEI for the lithium system with artificial interfaces and electrolyte modulation. However, analogous successful efforts with sodium are limited.[6, 72] Further, the presence and role of solubilized sodium polysulfides is not well understood. The combined instability of the sodium metal anode and poor understanding of the conversion mechanism has prevented the discovery of a suitable electrolyte for Na-S system.

Additionally, without understanding of solubility challenges and rate limiting behaviors, educated host design is prohibited. Therefore, the majority of room temperature sodium sulfur battery work has focused on exploiting the solubility of high order polysulfides, modulating through selective products much like the high temperature system (equation 3),[73-74] or utilized the microporous confinement strategy demonstrated first in the Li-S system (Figure 1.5C), to isolate the active sulfur from the electrolyte.[71, 75-77] The confinement strategy, where sulfur is stored within ultra-small (<1nm) pores, causing sulfur chains to be limited in length (S_{2-4}), eliminates production of soluble polysulfides during operation, providing impressive cyclability. The strategy was abandoned for the Li-S system, due to difficult and expensive processing and the ability of other techniques to enable higher mass loadings. However for the sodium sulfur system, lower mass loading is less concerning when long-term stability gained. Further, the confinement host requires sodium ions to transport through the host to convert sulfur, allowing complete isolation of active material from the cell electrolyte, which is highly desired behavior in a system lacking optimized electrolyte.

1.3.3 Experimental Approach

Considering the success of the microporous confinement strategy in demonstrating long term stability in the lithium and sodium sulfur systems, Chapter 7[78] looks to develop a low cost microporous host to complement the exceptionally low cost of the active materials and push the limits of the low temperature vapor infiltration technique for loading of ultra-small pores. Here, table sugar is simply dehydrated and then pyrolized to form highly ordered microporous carbon spheres. The isothermal vapor process is then able to rapidly and fully infiltrate the spheres consisting of micropores 0.5 nm in size throughout. This low cost composite demonstrates exceptional reliability on cycling providing promise for the chemistry in enabling viable stationary storage.

Chapter 2

Surface Oxidized Mesoporous Carbons Derived from Porous Silicon as Dual Polysulfide Confinement and Anchoring Cathodes in Lithium Sulfur Batteries

Adapted from: R. Carter, D. Ejorh, K. Share, A.P. Cohn, A. Douglas, N. Muralidharan, T. Tovar, and C.L. Pint, "Surface oxidized mesoporous carbons derived from porous silicon as dual polysulfide confinement and anchoring cathodes in lithium sulfur batteries," J. Power Sources 330, 70-77, (2016) *with permission from Elsevier*.

2.1 Introduction

Lithium sulfur batteries are poised as a technology to provide a midpoint between the energy storage capability of lithium-ion batteries, and emerging batteries that have promise to compete with the energy density of fossil fuels. This advance is critical due to the increasing reliance of modern technology on portable power storage.[3] The most primitive design of a lithium-sulfur battery incorporates an elemental sulfur cathode and lithium metal anode which exhibits a high theoretical energy density (2600 Wh/kg[79]) with the inherent benefit of the low cost and earth abundance of sulfur. However, practical routes to achieve lithium-sulfur batteries based on complete conversion of elemental sulfur to lithium sulfide have proven to be quite challenging due to three major issues 1) large volumetric expansion 2) poor electrical conductivity and 3) polysulfide stability in electrolyte.[48] This has led to an immense interest in using carbon as a backbone material for cathodic sulfur loading since lightweight carbons can be produced with high porosity,

carbons are natively conductive, and high sulfur loading of carbons can enable total electrode capacities that significantly overcome traditional lithium-ion cathodes.

Among the most studied materials are mesoporous carbons. Early studies by Ji *et al*. demonstrated a mesoporous carbon composite cathode by melt diffusing CMK-3 with 70 wt.% S. The cathode was capable of delivering high capacity of 1320 mAh/g, but with durability only analyzed over 20 cycles.[80] Subsequent efforts with mesoporous carbons exhibit high capacity with rapid linear decay of storage capacity that has provided a bottleneck for these materials.[33-35, 81] This capacity fade is attributed to polysulfide shuttling, where elemental sulfur (stored as S_8 crystals) is reduced to the soluble S_6^{2-} (bound to $2Li^+$) state during the multistep transition to lithium sulfide. If out-diffusion of the soluble compound (Li_2S_6) is permitted from the cathode side, fouling of the lithium metal anode can occur leading to rapid loss of storage capability.[79] Whereas some attempts have been made to address this through electrolyte additives,[82] recent efforts have mostly been aimed toward materials-level approaches to mitigate these challenges.

The first of these approaches employs an interlayer between the cathode and separator to trap dissolved polysulfides near the cathode and instigate precipitation on the cathode before formation of the final discharge product Li_2S.[19-20] Another strategy for preventing polysulfide dissolution is sulfur encapsulation using synthesized constructs such as yolk-shell structures,[38, 48] graphene wrapping,[39, 41] and microporous carbons.[25-37] Encapsulation in microporous carbon is most commonly carried out in carbide derived carbon materials due to the uniform micropore sizes (< 2 nm) that arise based on removal of metal clusters from the carbide which can be interconnected through mesoporous networks.[27] Building on this approach, recent efforts have proposed that confinement in

ultra-small pores (< 0.5 nm) can prevent the formation of soluble Li_2S_6[21-24] which can improve performance. Most recently, anchoring materials with polar surface characteristics such as metal oxides[44-46, 83] and functionalized carbon materials[83-84] have been demonstrated to pin soluble polysulfide species to the cathode and reduce capacity fade.[43] Overall, current efforts therefore build upon either structural or chemical roles of confinement in sulfur cathode materials, leading to an emerging research area that can simultaneously combine these confinement strategies into the framework of a single electrode material.

In this spirit, our work demonstrates a new family of mesoporous carbon materials that are derived from porous silicon and unlike other reports on mesoporous carbons, *simultaneously* exhibit both structural confinement and chemical anchoring of soluble polysulfides for lithium sulfur batteries. Defective carbons are directly grown in a self-limiting manner onto porous silicon templates, and the porous silicon is dissolved in aqueous basic (salt-water) conditions to yield mesoporous carbons with structural features correlated to the porous silicon template, and surface chemical features dictated by the material synthesis. Unlike other routes to produce mesoporous carbons such as carbide-derived carbons, our work enables a route to decouple the carbon chemical properties and the structural properties in the framework of scalable or low-cost processing based on conventional semiconductor manufacturing techniques. We demonstrate high initial capacity and excellent capacity retention of these cathode materials approaching key cathodic performance targets that arises from a two-fold strategy to inhibit polysulfide shuttling.

2.2 Experimental Details

2.2.1 Porous Carbon Preparation

Porous silicon was formed through electrochemical etch of highly boron doped (p++) silicon wafers using an AMMT porous silicon etching system. The etch applied was 60 mA/cm^2 current density to the wafer for 100 seconds in 8:3 (v:v) ethanol, hydrofluoric acid (50% water by volume Sigma Aldrich) electrolyte. The wafer was then fully rinsed in ethanol and then loaded into a Lindberg Blue 1" tube furnace for carbon growth by chemical vapor deposition (CVD). The furnace was ramped to 650°C under 1 SLM of Ar and 200 SCCM of H_2. Then 10 SCCM of C_2H_4 is allowed to flow as the furnace ramps to 750°C. Upon reaching 750°C the temperature is maintained for 10 minutes and then ramped to 850°C and held for 10 minutes. The acetylene was then turned off and the system is allowed to cool to room temperature under hydrogen and argon. After removing the sample from the tube furnace it is heated to 60°C in a 2M solution of NaOH for 48 hours. The freestanding carbon flakes are washed in nanopure water while monitoring pH until the solution is neutral. The material are allowed to rest in a water bath for 1 hour and exchanged once. The water is then removed and material suspended in ethanol. The carbon and ethanol solution is probe sonicated for 2 minutes to form uniformly sized particulates. The solution is centrifuged for 15 minutes at 9000 rpm and the ethanol is removed leaving micron scale mesoporous carbon flakes in powder form.

2.2.2 Porous Carbon/Sulfur Composite Preparation

This powder is then mixed with elemental sulfur in a 1:3 ratio and heated just above the melting point of sulfur 120°C for 6 hours. The carbon is fully infiltrated through capillary action and low surface energy of sulfur. The mixture is then flash heated to 200°C for 5 minutes to burn off the excess sulfur not infiltrated into the carbon.

2.2.3 Cell Fabrication and Electrochemical Measurement

The material was then prepared into electrodes by mixing the prepared material with PVDF and carbon black in a 7:1.5:1.5 ratio by mass with a small amount of NMP (Sigma Aldrich). The mixture was bath sonicated for 1 hour and then applied to steel discs (MTI) and vacuum dried. This process resulted in an areal sulfur loading of 0.3-0.6 mg/cm^2. Electrochemical half-cells were assembled in an argon glovebox using CR 2032 stainless steel coin cells (MTI) with prepared electrode as cathode, elemental lithium as counter and reference electrode and 2500 Celgard as separator wetted with electrolyte. The electrolyte used was 1M LiTFSi, 0.25M $LiNO_3$ in DME:DOL 1:1 by volume (all from Sigma Aldrich). Electrochemical testing was carried out using Metrohm Autolab and MTI potentiostats.

2.2.4 Materials Characterization

Materials Characterization was carried out using SEM (Zeiss), TEM (FEI) to investigate surface morphology and composite features. Raman (Raith) spectroscopy was used with 532 nm laser excitation to assess carbon quality and surface features and XRD was used to assess crystallinity. BET (ASAP 2020 V3.01 H) was employed to analyze the pore characteristics, and UV/Vis (Cary) was employed to verify polysulfide immobilization through polar binding.

2.3 Results and Discussion

The process used to develop porous silicon derived mesoporous carbon is shown schematically in Figure 2.1a. This process builds on our previous works in which carbon passivated porous silicon was studied[54, 58] and employed as supercapacitor electrodes,[52] Li-ion battery anodes[57] and photocapacitor electrodes.[59] The first step of the process is an electrochemical etch of silicon to generate a controlled highly porous template. Next a thin conformal layer of defective carbon is grown on the porous silicon template. Since porous silicon is rapidly dissolved in aqueous basic solution,[54] the mesoporous carbon is released from the porous silicon in a manner that allows the carbon to retain the pore network and structure of the porous silicon sacrificial template. These carbon pieces are then sonicated and dried to yield a powder of micron-scale particulates that can be efficiently loaded with sulfur.

This process produces a high porosity, low-density porous carbon material. To assess these properties in the framework of sulfur cathodes, nitrogen adsorption-desorption isotherms were used to determine surface area and pore volume. The isotherm shape (Figure 2.1b) reveals type IV hysteresis according to the IUPAC classification[41] indicating mesoporous character.[29] The Brunauer-Emmett-Teller (BET) surface area measured from the isotherm was 420 m^2/g and pore volume determined using the Horvath-Kawazoe model was 0.72 cm^3/g, with a majority of mesopore volume (0.60 cm^3/g in mesoporous range and 0.11cm^3/g in microporous range). This high pore volume concentrated in the mesoporous range will enable ideal behavior in a sulfur

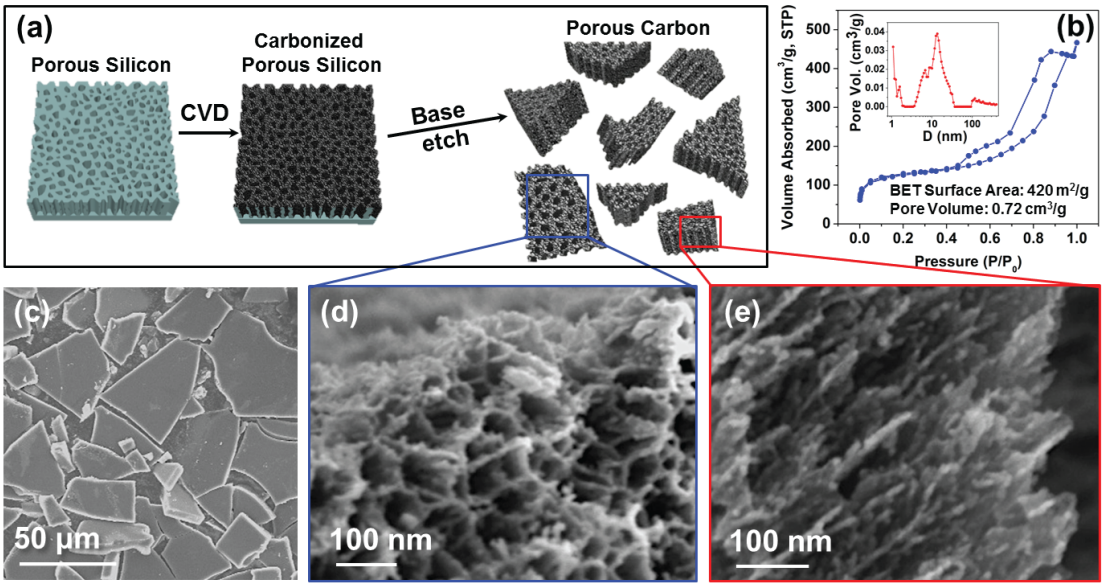

Figure 2.1- **A** Schematic representation of mesoporous carbon material processing, **B**, Nitrogen adsorption/desorption isotherms with inset showing pore size distribution, **C** scanning electron micrograph of sonicated porous carbon, leaving micron scale flakes of interconnected material, **D** SEM top down view of mesoporous carbon material, **E** SEM cross sectional view of mesporous carbon.

anchoring material.[29, 32] Similarly, the pore size distribution (Figure 2.1b, inset) reveals a broad peak ranging from 3.7-37 nm, centered at 13.7 nm, and a peak near ~ 1 nm. This correlates with to the structure of porous silicon that contains pore channels linked to pockets of micropores in the materials (apparent in SEM images Figure 2.1e-f).

Scanning electron microscope (SEM) analysis of these microscale mesoporous carbon particulates is shown in Figure 2.1c, with higher magnification images showing the nanoscale pore features in Figure 2.1d and e. From SEM the high porosity of the material is apparent with a pore diameter of about 15 nm (Figure 2.1d) which agrees well with the pore size distribution. The images also reveal the thin, semi-transparent flake-like edges (Figure 2.1e) which are unique attributes of this. Figure 2.1e also reveals the tree-like

porous structure, characteristic of the porous silicon template, further emphasizing the material maintains the structural integrity of the template following removal.

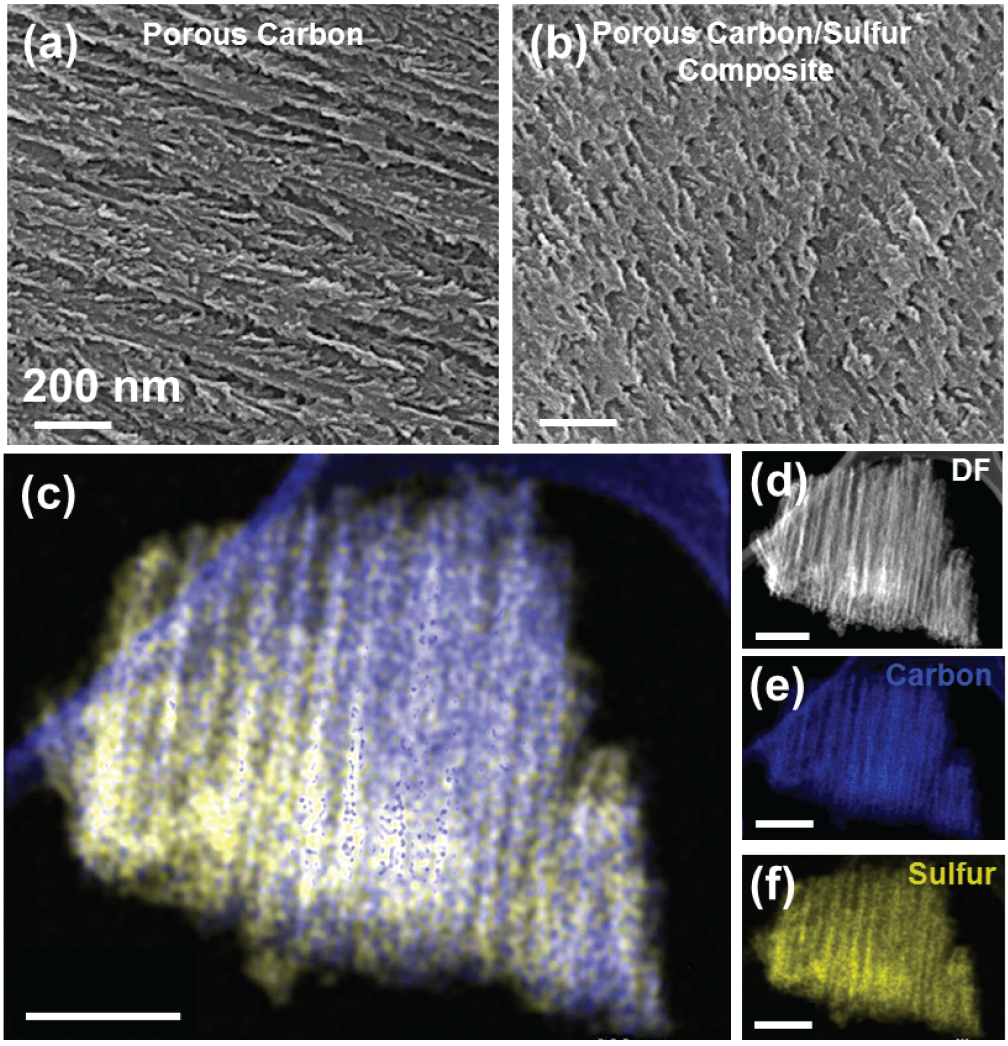

Figure 2.2- **A** SEM cross sectional view of mesoporous carbon material, **B** SEM cross sectional view of mesoporous carbon/sulfur composite material **C** STEM EDS composite map **D** STEM image of a mesoporous carbon flake, **E-F** STEM elemental map **E** of carbon and **E** of sulfur. All scale bars are 200 nm.

To prepare a lithium-sulfur battery cathode, the carbon powders are melt infiltrated with sulfur *via* a simple method commonly used to produce carbon-sulfur composites.[21, 24, 85] Figure 2.2 shows SEM images both before (Figure 2.2a) and after (Figure 2.2b) sulfur infiltration at 60wt.% sulfur. Sulfur loading is measured to be ~ 0.5 mg/cm^2 and ~ 0.3 μg/cm^2 relative to total footprint and specific surface area, respectively. In this architecture, the tree-like morphology of the porous silicon-derived carbons leads to small pores that actively confine sulfur near electrically accessible sites, and larger channels (~15 nm) that allow access of electrolyte ions to the sulfur for the formation of Li_2S. The material also maintains a high level of porosity even with the relatively high loading of sulfur that gives promise for excellent electrolyte penetration and good performance. To verify the distribution of sulfur in the porous carbon, a flake of porous carbon/sulfur composite was imaged using scanning transmission electron microscopy (STEM) for elemental mapping (Figure 2.2c). Elemental maps of carbon and sulfur (Figures 4.2e, 4.2e) indicate uniform distribution of sulfur in the porous network of the carbon. Thermogravimetric Analysis (TGA) was further used to verify the sulfur loading of the material and is shown in Figure 2.3. This analysis was used to normalize device data to the mass of sulfur present in order to compare to the theoretical device performance.

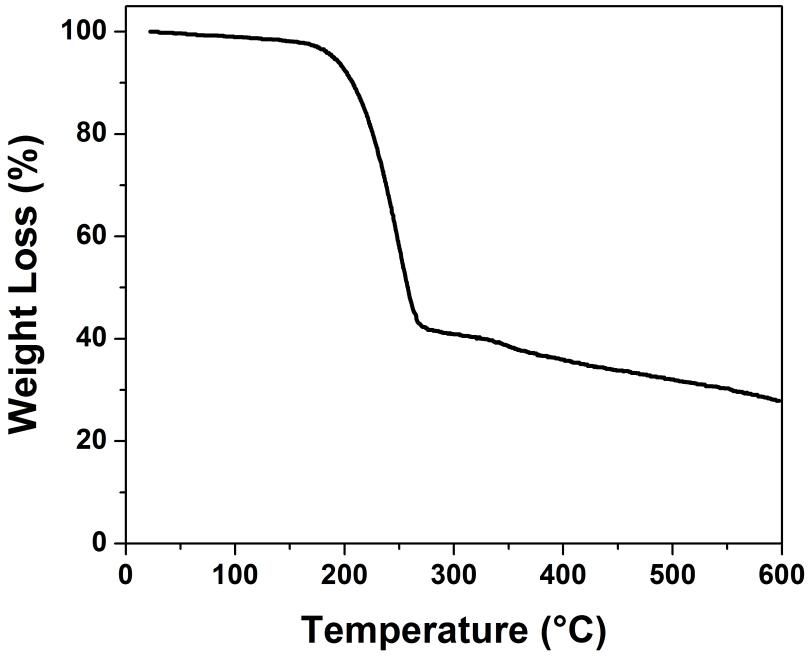

Figure 2.3- Thermogravimetric analysis of porous carbon verifying 60 wt.% sulfur loading.

In order to further analyze the porous carbon/sulfur composite, Raman spectroscopy was used to compare the porous carbon and the porous carbon/sulfur composite. The porous carbon exhibited characteristic D and G carbon peaks representing defective sp^3 hybridized carbon bonds (1350 cm^{-1}) and ideal in-plane sp^2 carbon bonds (1595 cm^{-1}) respectively (Figure 2.4a). The equivalent ratio of D to G peak emphasizes the defective nature of the porous carbon as a result of the synthetic process. Upon sulfur infiltration, the elemental sulfur (S_8) Raman signature most prominently at 219 and 473 cm^{-1} overwhelms the carbon signal. This is indicative of a high loading of crystalline S_8 structures of elemental sulfur on the interior of the defective carbon material, with no change to the corresponding Raman features of the carbon material.

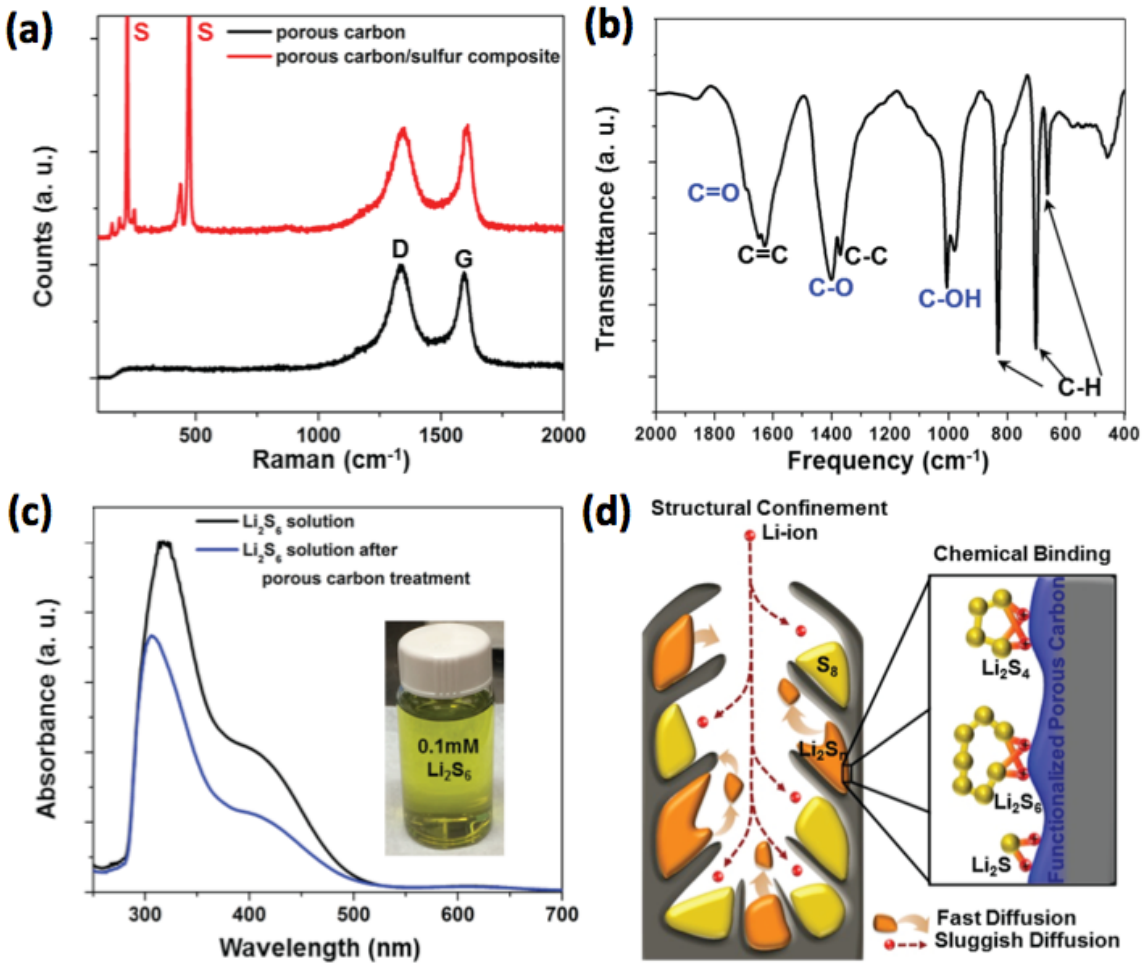

Figure 2.4- **A** Raman spectroscopy with 532 nm excitation of porous silicon derived mesoporous carbon and mesoporous carbon/sulfur composite material, **B** Fourier transform infrared spectroscopy of mesoporous carbon material with notable stretch modes labeled, **C** UV/vis absorption spectra of Li_2S_6 solution before and after exposure to porous carbon material with inset photo of polysulfide solution **D** schematic representation of two-fold polysulfide confinement by controlled pore structure (left) and by surface anchoring of polysulfides (right).

A key feature of this material is the combination of high defect concentration that leads to functionalized sp^3 carbon surface sites and the controllable and interconnected porous structure that enables electrical conduction and sulfur storage. Recent studies have indicated that surface polar sites are critical to anchor soluble polysulfide species, and we

elucidate this as a strength of this material fabrication approach. The sp^3 hybridization of carbon that arises due to defects in the carbon lattice can be controlled during synthesis of this porous carbon material and leads to out-of-plane dangling bonds on the carbon surface that are susceptible to functionalization. Following the aqueous dissolution of the porous silicon template, the high defect content of the carbon is expected to lead to an oxidized surface that will anchor soluble polysulfides in accordance with recent reports.[36]

To study this, Fourier transform infrared spectroscopy (FTIR) spectroscopy is used to analyze the infrared response of a KBr pellet with porous carbon in a 1% mass ratio. The presence of C-OH, C-O, and C=O groups are confirmed using FTIR (Figure 2.4b). The three sharp peaks at lower frequencies (663, 702, and 831 cm^{-1}) are C-H stretch modes, the peak at 977 cm^{-1} agrees well with a bound O-H group stretch, and the sharp peak at 1007 cm^{-1} reveals C-O stretch with the bound OH. The double peaks in range of 1350-1450 cm^{-1} agree well with C-C and C-O stretching respectively and the broad peak from 1550-1750 cm^{-1} comprises of C=C and C=O stretch with the C=O arising in the shoulder at the higher wavenumbers of the peak.[86] This is representative of a material with a high defect content and polar oxygen-containing functional species on the surface. These polar groups provide pinning sites for the polar $2Li^+$ species in soluble Li_2S_n compounds to mitigate soluble species dissolution into the electrolyte.

To demonstrate the polar binding and anchoring effect of these materials, UV/vis absorption spectra was used to compare the known Li_2S_6 absorption peaks[87] before and after exposure to porous silicon derived mesporous carbon. Since the polysulfide discharge product Li_2S_6 is soluble in DME:DOL, fully solubilized solutions of the species were developed by adding stoichiometric amounts of Li_2S and S_8 to the solvents and

spinning the solutions at 60°C for 12 hours. Porous carbon was then added to the solution of known concentration and allowed to spin for 24 hours. The spectrum of this solution was compared to solution not treated with carbon (Figure 2.4c). The porous carbon treated solution exhibited an absorption intensity decrease at the known S_6^{2-} absorption peaks around 300 and 350 indicating a change of concentration of these species and verifying the ability of the material to bind the polar and soluble discharge product.[84, 88] The peaks also exhibit a blue shift, which is another sign of strong interaction between the material and the solution, resulting in slight change in behavior of still solubilized species.

Figure 2.4d schematically represents the utility of this material for confining soluble polysulfides in the framework of lithium-sulfur cathodes. First, structural confinement is a result of the ideal material geometry provided by the porous silicon template. The high aspect ratio of nanopores (about 15 nm in diameter and 8 μm in depth) provides a wide pathway for the rapid transport of Li^+ species (0.18 nm), but a torturous pathway for the transport of soluble polysulfides. Along the pore channels are small micropores that provide locally electrically interconnected binding sites for ideal confinement in a sulfur cathode. Second, the confirmation of polar functional groups on the porous carbon surface enables chemical anchoring of soluble polysulfides in a manner that is synergistic with structural confining features. As discussed previously, dissolution (and capacity fade) occurs when S_6^{2-} is not anchored to electrode materials because of its solubility in DME:DOL electrolytes (most common for Li-S batteries). The binding of Li_2S_8 to electron rich oxygen groups found on the carbon surface will allow for transition to Li_2S_6 and then Li_2S_4 without the dissolution of sulfur-containing species. The structure of several polysulfides is depicted in Figure 2.4d to emphasize the strong polarity of the

compounds and their binding on the functionalized carbon surface. The combination of these two effects, structural confinement and chemical binding, allow optimal characteristics expected for a sulfur cathode material and near-theoretical capacity since the active material is highly accessible and fully intact. It also allows strong cycling performance due to the prevention of polysulfide dissolution in subsequent cycles.

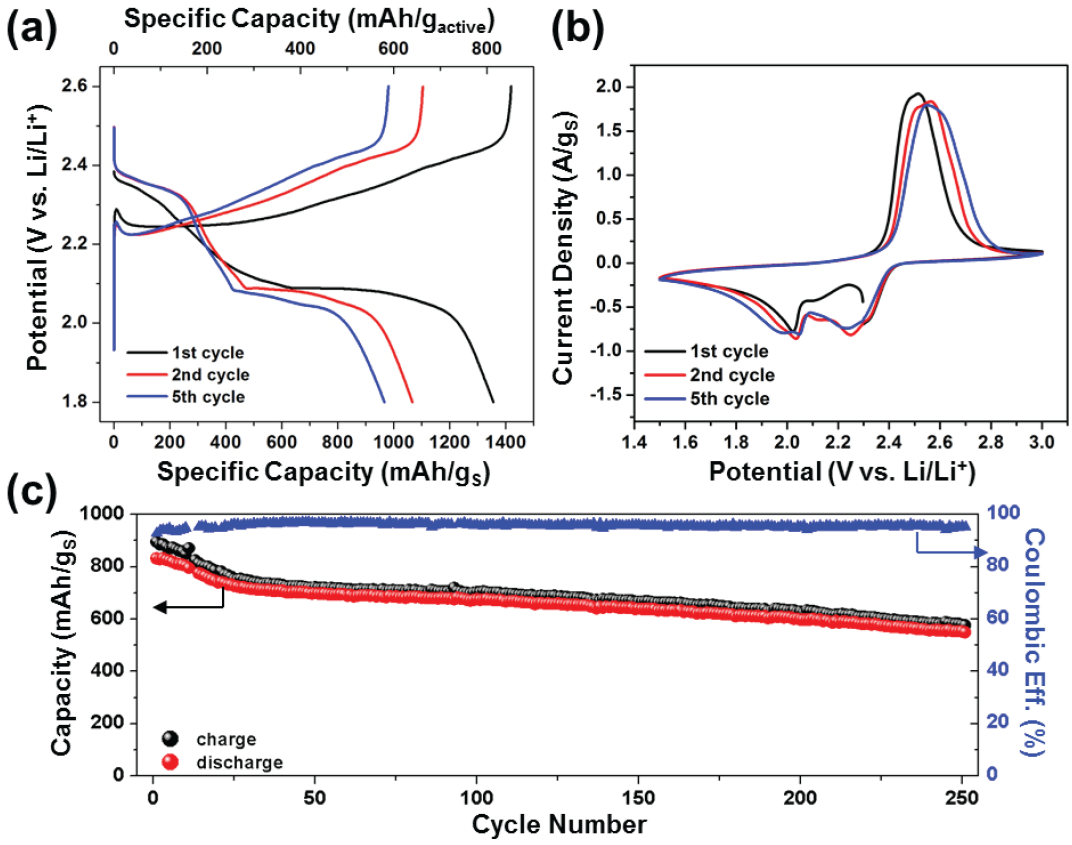

Figure 2.5- Electrochemical tests of porous silicon-derived mesoporous carbons as lithium sulfur battery cathodes. **A** galvanostatic charge discharge at 0.1C rate showing the first five cycles, **B** Cyclic voltammetry at scan rate 0.1 mV/s for the first five cycles, **C** Durability measurements based on galvanostatic charge discharge at 0.2C rates over 250 cycles. Blue points correspond to the Coulombic efficiency, labeled on right side axis.

To support the picture in Figure 2.4, full electrochemical characterization was carried out and is shown in Figure 2.5. The material was galvanostatically charged and discharged at a rate of 0.1C (1675 mA/g_{sulfur}) to assess discharge capacity and durability. The material exhibited high initial discharge capacity of 1350 mAh/g_{Sulfur} or 810 mAh/g_{active}, the latter of which includes the mass of the porous carbon (Figure 2.5a).

This high initial discharge capacity approaches the theoretical capacity of lithium storage in sulfur. The strong stability of the upper plateau in which soluble polysulfides are formed confirms successful polysulfide confinement. Cathodic performance was further probed through cyclic voltammetry at scan rate of 0.1 mV/s. The two-step polysulfide transition[89] is apparent in the CV curves (Figure 2.5b) as well as the charge discharge curves (Figure 2.5a). On the initial discharge, the first conversion near 2.3 V involves the first major transition of S_8 to Li_2S_6, while the second peak near 2.1 V is the complete conversion of the material to Li_2S. Again in this characterization, the stability of the first peak in subsequent cycles emphasizes the ability of the material to confine polysulfides before dissolution of soluble S_6^{2-} can occur. The initial capacity fade that is manifested in the total area under the anodic and cathodic CV scan is apparent in Figure 2.5b as well as a slight degradation between 2nd and 5th cycle. From durability experiments that were conducted over 250 cycles at rates of 0.2C, it is evident that a small capacity fade occurs in the first 20 cycles, and then the capacity stabilizes. This initial fade is attributed to slightly insufficient surface area to accommodate Li_2S species which could be improved through the versatile control of porous silicon etching to control both surface area and porosity. From the first to 100th cycle, we observed 81% capacity retention, which is impressive in comparison to previous efforts in carbon anchoring materials[22, 25, 27,

[33, 35, 37, 39, 41, 83, 85] and approaches the aim of lithium sulfur chemistries to obtain 90% retention over 100 cycles.[90-91] We directly attribute this improved performance to the two-fold polysulfide confinement that builds from structural confinement from the porous structure and chemical anchoring due to the oxidized, high defect content carbon surface. As a result, full conversion of S_8 to Li_2S is achieved on discharge and reversed on the charge. The ability to fully recharge is directly represented in the high Coulombic efficiencies greater than 95% between the 20th to the 250th cycle. In previous studies, maintaining high Coulombic efficiencies and achieving good durability – two closely related features, have presented a major challenge. In this work, we show that this new family of materials that are derived from electrochemically etched templates, can overcome these challenges and enable optimized performance in lithium sulfur battery cathodes.

2.4 Conclusion

In conclusion, we present a new technique to produce lithium sulfur battery electrodes based on coating high defect-containing carbon onto sacrificial porous silicon templates. This yields an oxidized carbon surface demonstrated to be effective for polysulfide anchoring in addition to the structural confinement offered by the porous nature of the carbon. Combined, this enables us to achieve initial capacity of 1350 mAh/g_{Sulfur} with 81% capacity retention over 100 cycles at slow rates of 0.2 C, which is competitive or better than the best reported state-of-the-art cathode materials. Compared to other routes, structural control enabled from the porous silicon template builds on over

six decades of research in low-cost semiconductor manufacturing and is transformed into a sacrificial template for defect-controlled porous carbons through scalable and low-cost steps such as acetylene treatment and dissolution in (basic) salt water. Unlike other routes to produce mesoporous carbons, the independent control over (1) the structure of the porous silicon and (2) the chemical properties of the carbon grown on the porous silicon enables a fine control knob on tailoring the chemical and structural properties to be optimized for sulfur cathodes. This opens an exciting area to connect fabrication processes rooted in low-cost semiconductor manufacturing with emerging battery systems that have promise to advance beyond the performance of lithium-ion batteries.

Chapter 3

Solution Assembled Single-Walled Carbon Nanotube Foams: Superior Performance for Various Energy Storage Electrodes

Adapted from: R. Carter, L. Oakes, A. Cohn, J. Holzgrafe, H.F. Zarick, S. Chatterjee, R. Bardhan, and C.L. Pint, "Solution assembled single walled carbon nanotube foams; Superior performance in supercapacitors, lithium ion, and lithium air batteries," J. Phys Chem C 118, 20137-20151 (2014) *with permission from the American Chemical Society*.

3.1 Introduction

Single-walled carbon nanotubes (SWCNTs) possess extraordinary promise as next-generation building blocks for the advanced design of materials with applications across energy, electronics, sensing, and composite materials.[92] The electrical, thermal, and mechanical properties that exist at the length scale of individual SWCNTs have driven interest for next-generation applications.[93-94] However, central to materials innovation is the construction of hierarchical three-dimensional (3-D) assemblies from these one-dimensional building blocks without compromising the inherent physical and surface characteristics that make SWCNTs appealing.[95-99] One route to achieve such materials is to synthesize SWCNTs in aligned structures that can be directly implemented in diverse applications from energy storage and conversion to optoelectronic devices.[100-106] Such approaches maintain pristine SWCNT character in usable architectures, but face challenges regarding the scalability and cost involved for practical implementation. This

makes another route involving liquid phase processing of SWCNTs attractive, as routes to solubilize SWCNTs, or more generally CNTs, into solvents is straightforwardly achieved using surfactants.[107-110] However, assembling these materials makes surfactant residue removal challenging or impossible, with the surfactant compromising desired properties of the material.[111] This has motivated surfactant-free routes utilizing superacids or organic polar solvents, which can natively disperse both graphene and SWCNTs.[112-120] Surfactant-free superacid dispersions of SWCNTs[113-114] have been demonstrated as an enabling route toward the assembly of multifunctional fibers with extraordinary mechanical and conductivity properties retained due to the pristine character of the SWCNTs.[121] On the other hand, *n*-methylpyrrolidone (NMP) is a polar solvent that can directly disperse graphene or SWCNTs,[115-116, 118-119] but routes to directly process functional materials from such polar solvent dispersions have yet to be realized. Current advances in electrophoretic deposition (EPD), a route for electric field-assisted solution assembly, require the use of surfactant in order to achieve deposition and assembly of SWCNTs and graphene.[68, 122-123] In this work, we demonstrate EPD directly from SWCNTs dispersed in polar NMP solvents, without the necessity of surfactant-based dispersions. As SWCNTs and more generally CNTs appeal to many applications, they are well-suited for electrochemical energy storage devices due to high surface area, good conductivity, and native electrochemical stability.[124]

In this spirit, our work explicitly demonstrates the importance of pristine assembly routes for freestanding SWCNT binder-free electrodes in electrochemical energy storage. Forming 3-D SWCNT foams directly from surfactant-free organic solvents leads to device performance in supercapacitors, lithium-ion batteries, and lithium-air batteries competitive

or better than performance previously reported for SWCNT materials. However, assembly of SWCNT foams mediated by TOAB surfactant suspensions leads to degradation of both the gravimetric and Faradaic chemical storage behavior in varying degrees for these devices in the order of lithium-air cathodes > lithium-ion anodes > supercapacitors. This work motivates the development of scalable solution-based routes to produce pristine, three-dimensional assembled carbon nanostructures to exploit their exceptional properties as catalytic sites or stable electrodes in a wide range of devices.

3.2 Experimental Details

3.2.1 Freestanding SWCNT Electrode Fabrication and Characterization

HiPCO SWCNTs (Unidym, purified) were deposited on a Ni foam template (positive terminal) with the use of electrophoretic deposition. Well-dispersed solutions of SWCNTs of two types were created. The first consisted of 1mg/2mL of as received SWCNTS and THF and 10:1 mass ratio of TOAB (Sigma Aldrich) to SWCNTs. The second solution contained 3mg/4mL of SWCNTs and NMP (Sigma Aldrich). Both solutions were treated with sonication for 30 min prior to deposition. The solution containing THF and TOAB was centrifuged (9000 rpm for 10min) twice to remove excess surfactant prior to deposition, and redispersed using sonication. To perform electrophoretic deposition, a Ni foam (MTI) was immersed in a beaker filled with SWCNTs and connected to the negative terminal of the DC power source. A counter electrode is connected to the positive terminal in a parallel plate set up with a 0.5 cm separation distance, and a 30 V potential was applied across the plates. The SWCNT coated Ni foam is then removed from the

negative terminal and dried vertically in the hood for 12 hours. The dried Ni foam coated in SWCNTs is etched in HCl (37% Sigma Aldrich) for 48 hours. The freestanding SWCNT foam material is then transferred to a nanopure water bath for 1 hour and then further transferred to a new water bath for another hour. This material is dried under vacuum for 30 minutes leaving the freestanding SWCNT foam. Analysis of SWCNT foam materials was carried out using Scanning Electron Microscopy (Zeiss) (SEM) and Thermogravimetric Analysis (TGA). The SWCNT foams were also analyzed with a Renishaw inVia Raman microscope using 785 laser excitations.

3.2.2 Supercapacitor Device Fabrication Electrochemical Testing

Electrodes made from foam pieces of equivalent mass are separated with a polymer separator (Celgard) and coated with ionic liquid electrolyte ($EMIBF_4$ 98% Sigma Aldrich). These supercapacitor electrodes were electrochemically tested using a Metrohm Autolab multichannel testing unit. The tests included cyclic voltammetry (CV) with various scan rates (25-100mV/s) from -3 to 3V, electrochemical impedance spectroscopy (EIS), and galvanostatic charge discharge measurements at various charging currents (0.1 to 20 A/g).

3.2.3 Lithium-ion Battery Device Fabrication and Electrochemical Testing

Half-cell devices were assembled in an Ar glove box using stainless steel coin cells (MTI). The freestanding foam is assembled as anode material with 2500 Celgard seperator saturated with 1 M $LiPF_6$ in 1g/1mL of ethylene carbonate (EC) and diethyl carbonate (DEC) (Sigma Aldrich) separating the anode material from pure lithium foil (Sigma Aldrich). The device is crimped in a 2032 coin cell and tested utilizing a Metrohm autolab multichannel testing system. Cyclic voltammetry was performed on the devices between 0-3.7 V at various scan rates (0.5-100 mV/s) and Galvanostatic charge-discharge

measurements were carried out for 7 constant currents ranging from 186 mA/g to 14.88 A/g. Cycling studies were performed at 744 mA/g, and samples were tested after 300 cycles at the 7 current densities initially utilized to assess post-cycling performance.

3.2.4 Lithium-air Battery Device Fabrication and Electrochemical Testing

Mesh coin cells containing 0.1 M $LiClO_4$ in TEGDME were assembled in an Ar glove box using free-standing SWCNT foam as the cathode material separated from Li foil with a Celgard 2500 membrane. These batteries were sealed in an MTI test cell under 1 atmosphere of a mixture of ultra-high purity 20% oxygen and 80% Argon gas at room temperature. The devices were tested under Galvanostatic charge discharge at three constant current discharge rates of 1 A/g, 0.5 A/g, and 0.1 A/g using a Metrohm Autolab multichannel testing system.

3.2 Results and Discussion

Central to the fabrication of pristine 3-D SWCNT foam materials is the ability to assemble SWCNTs directly from surfactant-free solutions. To achieve this, we utilize NMP polar solvent suspensions of SWCNTs and EPD assembly. This gives us the ability to form pristine coatings of SWCNTs on the surface of metal foams, where the metal foam is then dissolved in HCl to yield a freestanding foam material of SWCNTs (Figure 3.1a-c). After rinsing and drying this material, a structure remains composed only of SWCNTs that retains the porous microstructure of the metal foam. Unlike CVD processes, where self-assembly during growth dictates the microstructure of CNT or SWCNT materials, even in tunable post-growth processing,[125] this approach enables careful tuning of the

microstructure based on the choice of metal foam in the framework of a scalable, low-power (*e.g.* up to 120 V, low currents) solution processing route. Furthermore, as opposed to conventional solvent processing techniques utilizing surfactants, the use of NMP maintains the pristine character of the SWCNT. Characteristic SEM images of 3-D foam structures showing the bundle microstructure and the microscale foam features after removal of the sacrificial metal template are shown in Figure 3.1 e-f.

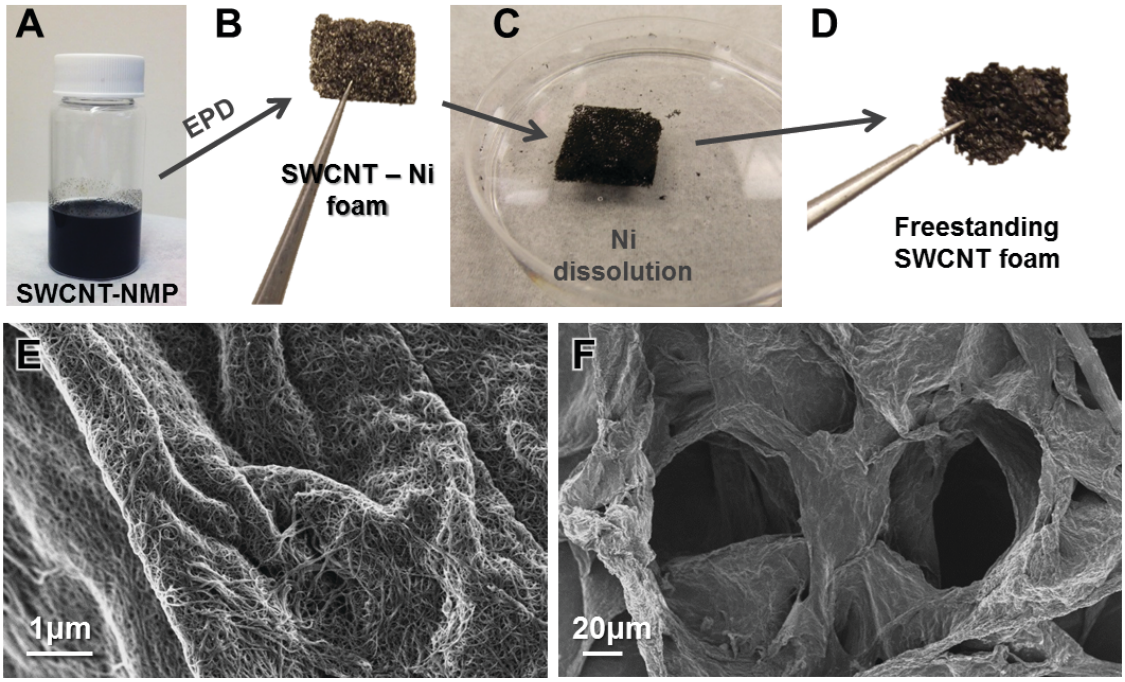

Figure 3.1- A. SWCNT-NMP surfactant-free suspensions utilized to make freestanding foams, **B.** Ni foam coated with SWCNTs from NMP solutions using EPD, **C.** picture of a freestanding SWCNT foam following dissolution of the sacrificial Ni foam substrate, and **D.** picture of a freestanding SWCNT foam following metal foam removal and drying. **E-F** SEM images at different magnifications showing the nanostructured and microstructured features of SWCNT foams that remain in-tact in the freestanding material.

In order to assess the benefit of pristine SWCNT foams for applications, we also performed EPD assembly from tetrahydrofuran (THF) solvents containing SWCNTs suspended with tetraoctylammoniumbromide (TOAB) surfactant. This was performed in an identical manner as that shown in Figure 3.1 on metal foams to produce equivalent freestanding materials, except based on solutions where the SWCNTs are surfactant suspended. SEM comparison of NMP and surfactant-suspended SWCNTs at the same magnification (Figure 3.2a, 3.2b) indicates notably different surface properties of the deposited materials. The pristine (NMP) foam (Figure 3.2a) exhibits mat-like bundles of SWCNTs that appear free of excess contamination and consistent with the nature of bundles that are dispersed in NMP polar solvents. In the case of the surfactant-suspended SWCNTs, the resulting material evidently contains a surface residue of TOAB surfactant on the exterior of SWCNT bundles (Figure 3.2b). As we emphasize in this work, for applications that require the surface of the SWCNT as an active component to enable device performance, this insulating surfactant coating will significantly inhibit the performance of these materials. In order to quantify the different material characteristics evident in Figure 3.2a-b, thermogravimetric analysis (TGA) was carried out in air on both the pristine and surfactant-coated foams (Figure 3.2c) at 20ºC/min. However, for foams prepared from surfactant-suspended SWCNTs, the derivative weight loss analysis of the TGA measurements exhibits multiple peaks associated with thermal decomposition. We associate the derivative peaks at 500ºC and below primarily to weight loss due to removal of excess surfactant impurities, emphasizing the surfactant to be a significant portion of the total foam material weight that is not removed in the washing and HCl treatment required to dissolve the sacrificial foam and isolate the freestanding material. Notably, as

virtually all of the material mass burns away below temperatures of 800ºC, this supports the notion that our SWCNT materials remain free of excess metal impurities. This emphasizes the significantly enhanced pristine character of SWCNT foams using EPD from NMP polar solvents without the use of surfactant in comparison to conventional EPD routes where surfactant is required.

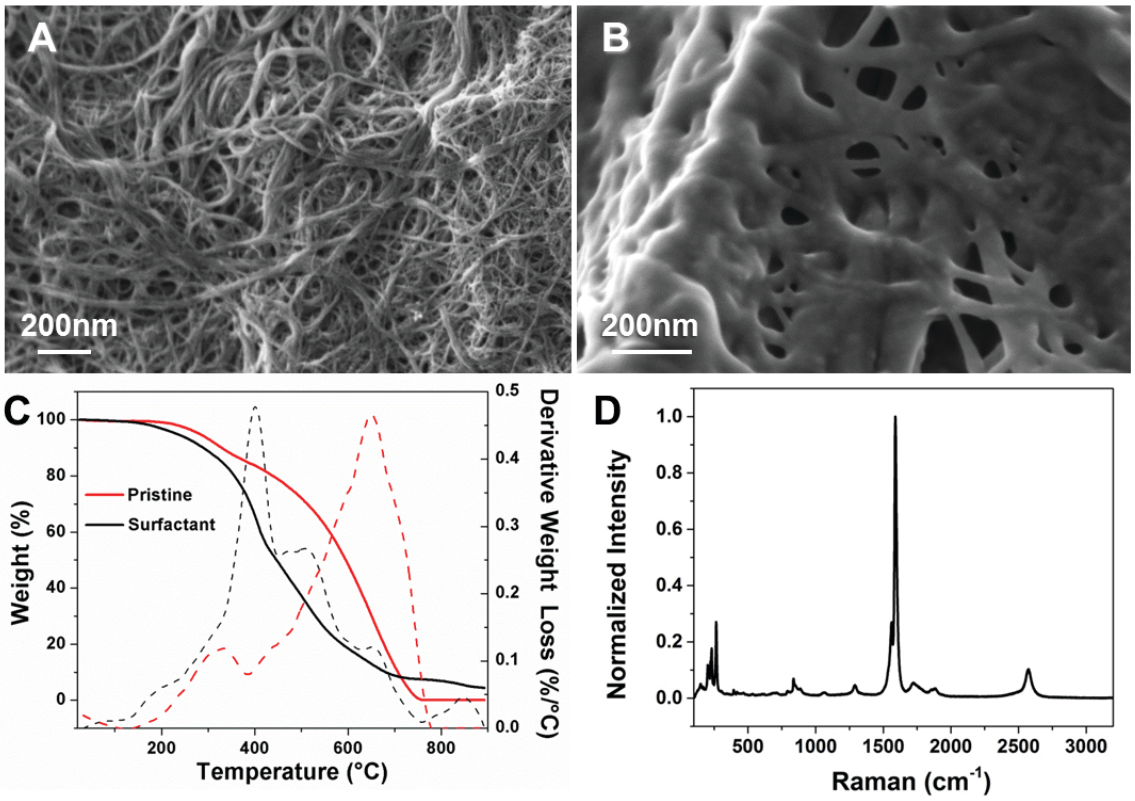

Figure 3.2- **A-B** SEM images at similar magnifications showing the different surface topology of the SWCNTs in foams prepared with NMP surfactant-free solutions **A** and TOAB-THF surfactant suspensions **B. C** Thermogravimetric analysis of SWCNT foams prepared using NMP (pristine) solutions and TOAB (surfactant) solutions. Derivative weight loss curves are shown with dotted lines. **D** Raman spectra of SWCNT foam materials showing features consistent with HiPCO SWCNTs.

In this manner, to the best of our knowledge, our work is the first to show that SWCNTs, or generally low-dimensional carbon nanostructured materials, can be EPD coated into structures without the use of surfactants to aid dispersion and enable deposition. Finally, as the SWCNTs that we utilize in this study are HiPCO produced material, we show Raman spectra of a typical foam material with 785 nm laser excitations in Figure 3.2d. Evident from this spectra is the presence of radial breathing modes (200-500 cm^{-1}), D band (~ 1293 cm^{-1}), G band (~ 1590 cm^{-1}), and 2D mode (2578 cm^{-1}) signatures – which are identical between the SWCNTs processed in NMP and THF-TOAB surfactant solutions.

Overall, SWCNTs are excellent candidates for broad applications in electrochemical devices. Their native high surface area, conductivity, electrochemical stability, and low mass density make them excellent for applications in energy storage systems. Our aim in this study is two-fold, specifically to (i) emphasize EPD from NMP-SWCNT suspensions as a viable route to assemble high performance, broadly applicable energy storage device electrodes, and (ii) demonstrate the importance of clean, surfactant-free processing routes on the performance of these electrode materials in different electrochemical platforms. To begin, we first demonstrate the utility of these SWCNT foam materials as binder-free electrodes in electrochemical supercapacitors (Figure 3.3). Supercapacitors operate on the premise of non-Faradaic charge storage through ions, in our case supplied using an ionic liquid 1-ethyl-3-methylimidazolium tetrafluoroborate ($EMIBF_4$), that assemble on the surface of a nanostructured conductive material.

We present the role of residual surfactant, supported by results from device analysis in in a scheme shown in Figure 3.3a. Overall, we generally find that residual surfactant leads to two primary effects in SWCNT foam supercapacitors, (1) poorer

gravimetric performance due to the residual mass of the surfactant in the material – a mechanism universal in all specific measurements discussed in this work, and (2) compromised non-Faradaic ion storage behavior on SWCNT surface sites where residual surfactant resides. To compare how the range of the values measured in this work relate to those reported previously in the literature for SWCNTs, we plot the specific capacitance measured at 0.1 A/g to the maximum specific capacitances measured for SWCNTs with a variety of electrolytes, processing techniques, and material morphologies (Figure 3.3b).

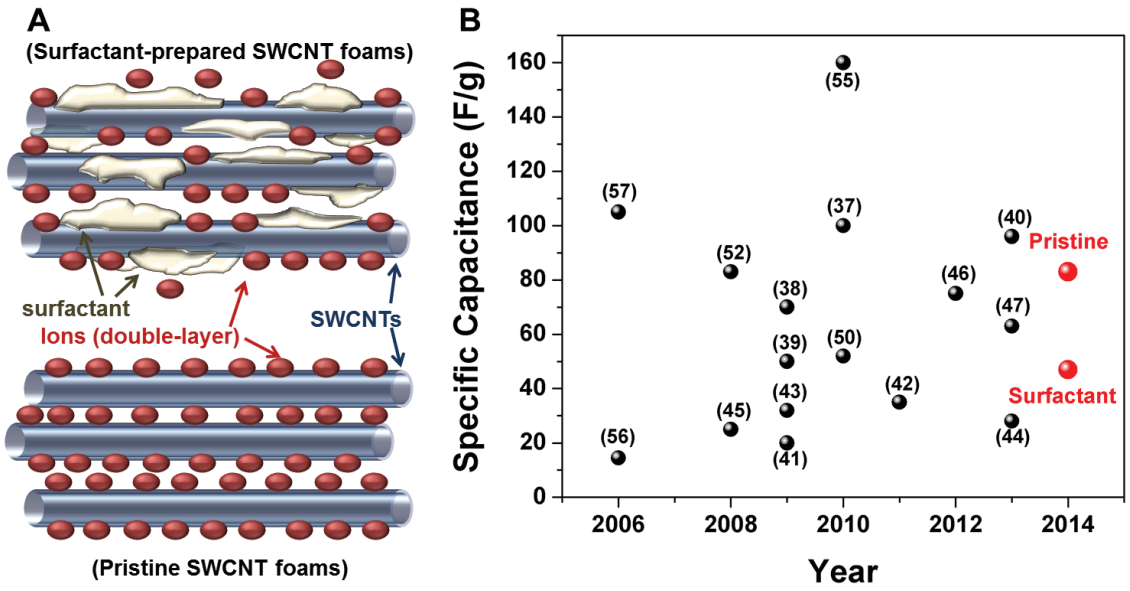

Figure 3.3- A. Schematic illustrating the effect of surfactant on the double layer storage behavior of SWCNT foams based on electrochemical measurements, **B.** Comparative analysis of supercapacitor results for pristine and surfactant-prepared SWCNT foams based on previous literature assessments of SWCNT supercapacitors.

Evident from Figure 3.3b is that most values measured for SWCNTs remain below 90 F/g and comparable to our maximum specific capacitance of 83 F/g measured for the pristine

SWCNT material. As most SWCNT materials are processed with binders or surfactant-processing, the results for our surfactant-prepared samples are consistent with the average results measured using such liquid processing techniques. The highest numbers reported thus far have been centered on materials where direct CVD growth was used to obtain the materials or care was taken in processing to limit impurities. This emphasizes the importance of clean, functional materials to exploit the non-Faradaic ion storage properties of SWCNT materials and emphasizes our SWCNT foams as being competitive with some of the best SWNCT supercapacitors developed thus far.

Whereas the high surface area of SWCNTs makes them excellent candidates for supercapacitors, SWCNTs have also demonstrated promise for improved Faradaic lithium metal storage in comparison to bulk carbon materials. In this manner, we employed these foams as Li-ion battery anodes in half-cell configurations involving Li foil cathodes, celgard 2630 separators, 1M $LiPF_6$ in EC-DMC electrolyte, and pressed into coin cells for testing. To assess their lithium storage capability, we first performed Galvanostatic charge-discharge measurements with charging currents ranging from 0.186 A/g to 14.9A/g (0.5 to 40C for conventional graphite) over a range of 0 – 3.7 V vs. Li/Li^+.

A schematic demonstrating the impact of surfactants on the lithium metal storage capability of SWCNTs is illustrated in Figure 3.4a. Here, illustrative energy diagrams are constructed to visualize the observations made in this study for Faradaic charge-storage reactions occurring between the $LiPF_6$ electrolyte and the surface of the pristine and surfactant-prepared SWCNT foams. Based on our observations in this study, we generally find that the presence of surfactant leads to higher average energies for electrolyte decomposition and metal storage, and lower average energies for the replenishing of

electrolyte with Li metal. By cycling the material, we observe this to improve for the surfactant-prepared foam, as charge-transfer reactions remove surfactant from the SWCNT surface while the pristine SWCNT material shows nearly identical or slightly degraded performance. In order to assess how these SWCNT foam materials in our work compare with other SWCNT and also multi-walled CNT electrodes, we included the capacities measured in our devices both before and after 250 cycles in Figure 3.4b in comparison to the highest capacities reported in other studies.

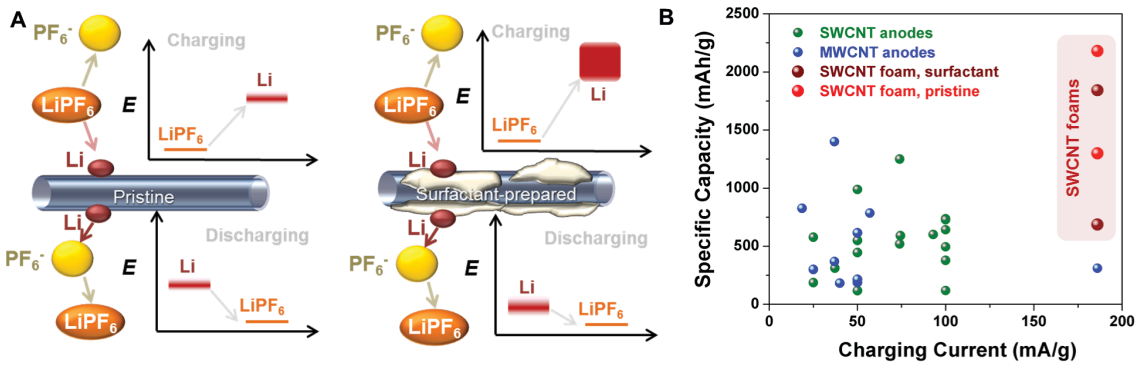

Figure 3.4- A. Schematic illustration of the effect of surfactant on the intercalation and de-intercalation behavior of SWCNT foam anode materials, with generalized energy diagrams for these processes that represent the measurements from this work. **B.** Comparative analysis of results for SWCNT foams compared to other literature-reported SWCNT and MWCNT materials used as lithium-ion battery anodes.

Prior to cycling, our work shows comparable storage capacities to the best reported CNT battery anode materials at charge-discharge currents (0.186 A/g) that are ~ 4X higher than other studies. After cycling for 250 Galvanostatic cycles at 0.74 A/g, we observe storage capacities greater than the best measured capacities on SWCNT materials thus far. Notably, as these measurements are carried out at charging/discharging currents of 0.186

A/g, compared to other studies that report values at < 100 mA/g currents, we emphasize the storage behavior at comparable rates for this material should be enhanced, even though such low rates are not practical for true operation of these devices. Additionally, where many of these reports involve capacities that exist at high voltages and poor energy efficiencies, we emphasize the important role of clean material processing on achieving materials that exhibit large capacities and the majority of that capacity usable in a full-cell device with good energy efficiency.

Whereas SWCNTs have great promise for lithium-ion batteries, significant effort has recently been focused toward the development of lithium-air batteries, which have the potential to exhibit energy densities superior to lithium-ion batteries and capable of replacing fossil fuels.[126-127] To realize such devices, cathodes that are electrically conductive, lightweight, and porous must be developed. Whereas previous reports have primarily focused on multi-walled CNTs as electrodes for lithium-air batteries, we demonstrate here that SWCNT foams can be viable high performance materials for lithium air batteries. In order to assemble lithium-air batteries, we sandwiched freestanding SWCNT foams with lithium foil in a mesh coin cell using 1 M $LiClO_4$-TEGDME electrolyte solutions. We then pressurize the coin cell holder with 20% O_2/Ar mixture, and carry out measurements on devices. Discharge voltages characteristic of lithium peroxide formation are evident in the Li-air battery prepared using pristine SWCNT foams, with a discharge plateau that extends to a total discharge capacity of 8275 mAh/g at a rate of 0.1 A/g, measured in the reversible regime above 2 V. This discharge capacity of the SWCNT foams exceeds that previously measured for SWCNT materials, and is consistent with the best results measured for MWCNT foams materials that remain

supported by Ni foam substrates (~ 8500 mAh/g). On the other hand, for the TOAB surfactant-prepared SWCNT foam materials, the discharge characteristics of the devices were poor, exhibiting a maximum of ~ 250 mAh/g at discharge rates of 0.1 A/g. At higher rates (0.5 A/g and above), the measured capacity was virtually zero, and this behavior was consistently measured across many test devices, with none of them showing any notable capacity. This significant difference in device performance emphasizes that the presence of surfactant on the SWCNT surface completely inhibits the nucleation of reversible charge storage products in the voltage range of 2-2.7 V vs. Li/Li^+ that are typically present in discharge processes with good lithium-air battery cathode materials. This leads us to conclude the difference between surfactant prepared and pristine foam materials (illustrated in Figure 3.5a), where surfactant plays an inhibitory effect on the nucleation process of reversible lithium-peroxide charge storage species on the SWCNT surface. Unlike lithium-ion batteries, where the role of the SWCNTs is to generate charge-transfer sites to form monovalent lithium, or supercapacitors where the role of the SWCNTs is to produce a conductive surface to form a double-layer, lithium-air batteries require a cathode material to support nucleation sites for chemical species that are catalytically formed on the SWCNT surface during discharge. This means that the presence of surfactant, unique from supercapacitors and lithium-ion batteries, can completely inhibit the Faradaic storage process in lithium air batteries and only enable the formation of irreversible products based on the reaction between the electrolyte and surfactant at low rates. Comparing these results to other results for SWCNTs and MWCNTs reported in the literature, our capacities at 0.1 A/g rates are comparable to the best reported values for

these materials (8275 mAh/g) and significantly improved compared to most CNT-based electrodes (Figure 3.5b).

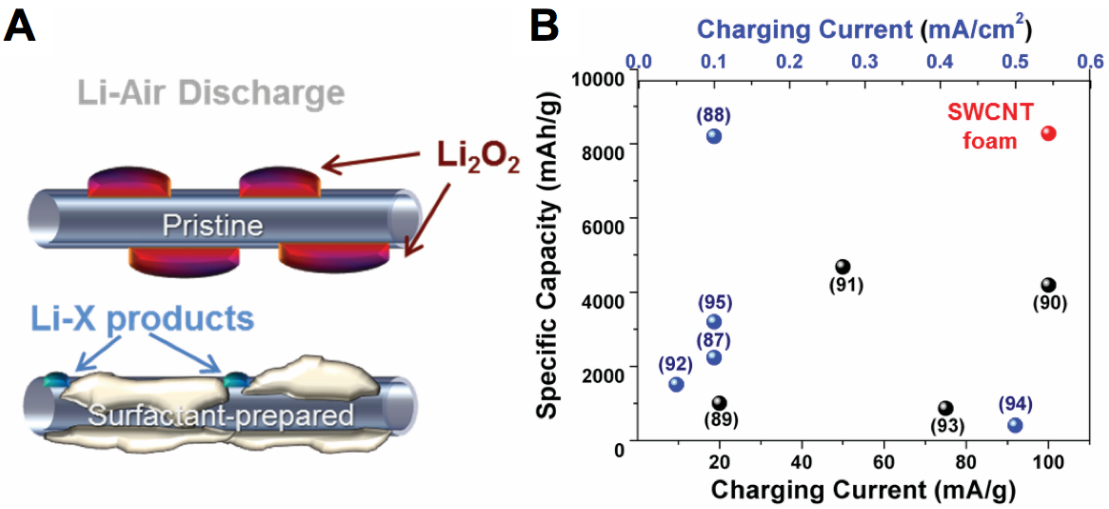

Figure 3.5- A. Schematic illustration demonstrating the formation of Li_2O_2 reversible charge storage products on pristine SWCNT foams compared to a low capacity of irreversible Li-X products on surfactant-prepared SWCNT foams. **B.** Comparative analysis between first discharge capacities measured in this work versus other SWCNT and MWCNT materials studied for Li-air battery cathodes.

Previous studies have emphasized capacities of up to ~ 8500 mAh/g for MWCNTs supported by Ni foam materials at discharge rates of 0.1 mA/cm^2,[128] with previous SWCNT materials demonstrating less than 3100 mAh/g at comparable current density. Our work here underlines the critical importance of SWCNT material processing and impurities on enabling practical, high rate and high capacity lithium-air discharge characteristics and further emphasizes the notion that SWCNT foams are a high performance and lightweight electrode material for lithium-oxygen or lithium-air batteries.

Overall, these results collectively suggest that freestanding SWCNT foams are a universal platform for high performance electrochemical energy storage, and that the route to achieve such high performance is to harness the utility of clean, liquid processing techniques that minimize impurities which can inhibit usable, efficient charge storage behavior. In the broadest sense, beyond electrochemical energy storage, our work emphasizes a message transferrable to areas of catalysis, sensing, energy conversion, or electronics, which emphasizes the foundation for innovation with such materials is the development and understanding of clean solution processing routes to manipulate and assemble SWCNTs into macroscopic, functional structures.

3.4 Conclusions

We demonstrate a route to use electrophoretic assembly to produce freestanding SWCNT foam materials, and compare the impact of processing these materials from pristine, NMP-SWCNT suspensions and TOAB-SWCNT surfactant suspensions. Our results indicate that the residual TOAB surfactant in the foam due to processing compromises the gravimetric and Faradaic storage characteristics of electrochemical energy storage devices in the order of lithium-air batteries > lithium-ion batteries > supercapacitors, where the greater value indicates more compromised storage performance. In the extreme case of lithium-air batteries, we find the presence of surfactant to completely inhibit the formation of reversible charge storage products upon discharge, with the surfactant-prepared foam to only exhibit ~ 3% of the total capacity of the pristine foam. Whereas these results emphasize the importance of clean solution

processing of SWCNT macroscopic materials, our results also give significant promise to the utilization of NMP-assembled SWCNT materials in electrochemical energy storage. We emphasize such excellent performance to be achievable through the development and utility of clean, surfactant or impurity-free assembly processes which preserve the native SWCNT surface properties, and is transferrable to diverse applications such as catalysis, sensing, electronics, and energy conversion, among others.

Chapter 4

Isothermal Sulfur Condensation into Carbon Scaffolds: Improved Loading, Performance, and Scalability for Lithium Sulfur Battery Cathodes

Adapted from: R. Carter, L. Oakes, N. Muralidharan, and C. L. Pint, "Isothermal Sulfur Condensation into Carbon Scaffolds: Improved Loading, Performance, and Scalability for Lithium Sulfur Battery Cathodes," J Phys Chem C, Just Accpeted 2017 *with permission from the American Chemical Society*.

4.1 Introduction

Lithium sulfur batteries exhibit great promise for improvement relative to state-of-the-art lithium ion batteries due to the superior energy density (2600 Wh kg-1), low cost materials, natural material abundance, and environmental sa3fety.[129-131] However, the direct use of elemental sulfur as a cathode material is limited by the insulating nature of sulfur and the 80% volume expansion experienced upon full polysulfide conversion.[132] Therefore, hybrid combinations of sulfur and electrically conductive materials that can contain and/or anchor sulfur species and maintain integrity during battery operation has been a key research focus.[13, 32] In recent years, many advances have emerged to mitigate polysulfide shuttling effects, such as externally situated membranes,[22, 133] encapsulating cathode materials,[21-23] and electrode materials with improved anchoring layers.[45, 48, 64, 134] However, approaches demonstrating high performance have commonly made use the melt-infiltration technique to form sulfur-carbon composite materials, requiring a large mass of material in powder form, additional binders, additives, or extra materials outside

of the sulfur and host material, as well as additional processing steps following infiltration, in order to produce a suitable film for electrode fabrication.[135] Commonly, specific cathodic performance is characterized independently from the mass introduced due to extra cathodic components (*e.g.* binders, membranes, *etc.*), even though these components are equally passive to the conversion chemistry of the sulfur active material.[17, 136-137] However, for lithium-sulfur battery performance to practically exceed conventional lithium-ion batteries, industry-scalable techniques must achieve high sulfur loading (> 70%) relative to *all* additives and components of the cathode template,[17-18] while simultaneously preserving the native specific capacity of the (insulating) sulfur active material. Until now, the few reports of high specific sulfur loading that matches this criteria indicate downfalls in storage capacity, cycling performance, and scalability considerations.[138-139]

On this front, research efforts focused on carbon-based cathodes have been centered on improved performance based on either pore confinement[140-143] and/or surface functionalization[83-84, 144] where sulfur infiltration yields low loadings < 50 wt.% or multiple long-duration steps until a usable battery material can be realized.[145] Whereas alternative approaches to melt infiltration have been proposed including electrolysis,[146] wet chemical methods,[147-148] simple mixing,[149-150] ball milling,[151] spray coating,[152-154] and catholytes[155-156] the incorporation of sulfur into porous structures is best achieved through melt-infiltration, leaving this as a benchmark technique in the research community.[157] High performance in lithium-sulfur cathodes requires a quartet between high loading of sulfur relative to the entire composite (> 70 wt.%), high capacity (> 1000 mAh/g_{sulfur}), excellent cycling performance (above 80% retention after 100 cycles), and high Coulombic efficiency (>

98%). Despite intense widespread research on lithium-sulfur batteries, only a few reports have emerged that indicate such combined levels of performance, and failure in even one of these categories undermines the practical nature of the battery. In fact, recent examination of 274 Li-S papers revealed that fabricated electrodes contain only 30-70%, which prohibit competitive performance with commercialized Li-ion cells. Additionally, less than half of these papers reported any information at all regarding the sulfur loading, prohibiting a direct comparison with other electrode architectures.[24] Notably, equipped with the thermodynamically-guided sulfur infiltration technique described herein, we report combined performance across these metrics, that is distinguished against a rigorous comparison of our electrode performance with the state-of-the-art carbon-based sulfur electrodes published in the last two years (Table 5.1).

In this report we demonstrate a simple isothermal technique where the high surface free energy of nanoscale pores or surfaces drives the spontaneous nucleation of sulfur liquids until conformal coating of condensate is reached. Unlike melt infiltration where such small pores are thermodynamically inaccessible, our approach achieves more complete and uniform coating, in addition to highly repeatable sulfur loadings exceeding 80 wt.%. The isothermal vapor process allows for rapid coatings of carbon nanomaterial scaffolds situated adjacent to saturated mixtures of sulfur. In order to directly compare this process to the widely accepted melt infiltration, melts of 155°C was utilized to make both composites for direct comparison of manufacturing cost and device performance. Both the vapor infiltrated and melt infiltrated consisted of carbon black – single-walled carbon nanotube templates and resulted in high mass loadings (~74 wt.%).

ref.	material discription	Sulfur Utilization (mAh/g)	rate (C)	decay rate (%/cycle)	rate (C)	loading (%)	additives (S:CB:binder)	Electrode Capacity (mAh/g)
-	SW/CB	1343	0.5	0.04	0.5	81	binder-free	1088
1	P. Carbon	1361	0.2	0.03	0.2	80	80:10:10	871
2	VS2	900	0.5	0.05	0.5	56	80:10:10	403
3	N-graphene	1486	0.05	0.08	1	90	80:10:10	1070
4	MnO2	1196	0.5	0.03	0,5	75.5	75:15:10	677
5	CNFs	1400	0.2	0.31	0.5	37	binder-free	518
6	P. Carbon	1382	0.5	0.29	0.5	72	80:10:10	796
7	MgO	1368	0.1	0.034	0.1	52.5	70:10:20	503
8	Gr	1374	0.1	0.1	1	59	80:10:10	649
9	rGO	1219	0.2	0.18	0.2	53	binder-free	646
10	CNTs	1633	0.1	0.27	0.1	68	80:10:10	888
11	MnO2	1120	0.2	0.09	0.2	56	75:10:15	470
12	CNTs	1264	0.1	0.315	0.1	60	binder-free	758
13	CNT/CB/Gr	1239	0.02	0.6	0.1	72	80:10:10	714
14	Gr/CNT	1070	0.2	0.475	0.2	56	binder-free	599
15	rGO	1400	1	0.5	1	35	70:20:10	343
16	CNT/Gr	1048	1	0.11	1	50	binder-free	524
17	P. Carbon	1246	0.1	0.475	0.1	63.7	85:12:03	675
18	P. Carbon	1346	0.2	0.17	0.2	62	binder-free	835
19	CNTs	1340	0.2	0.44	0.2	62	binder-free	831
20	P. Carbon	1021	0.5	0.5	0.5	57.12	80:10:10	467
21	graphene	1260	0.1	0.45	0.1	58.4	80:15:10	589
22	CNT/Gr	911	0.2	0.154	0.2	53	binder-free	483
23	P. Carbon	1317	0.1	1.2	0.1	48.3	70:20:10	445
24	P. Carbon	1070	0.1	0.052	0.5	53.6	80:12:08	459
25	rGO	1310	0.07	0.085	0.07	63	binder-free	825
26	CNF	1620	0.06	0.5	0.06	65	binder-free	1053
27	Gr	800	0.5	0.5	0.5	52	binder-free	416
28	CNT	750	0.1	0.44	0.1	76.5	85:15:00	488
29	P. Carbon	1010	0.2	0.3	0.5	62	90:10:00	564
30	P. Carbon	1278	1	0.3	1	47.25	75:15:10	453
31	P. Carbon	998	0.3	0.1	0.3	33.6	70:15:15	235

Table 4.1- Lithium sulfur works employing carbon scaffolds from 2014-2017. The very first entry to the table describes the work presented in this manuscript. . From this summary it is evident that very few works simultaneously achieve high sulfur conversion capacity and electrode capacity at loadings beyond 70 wt.%, and low decay rate. Corresponding reference list in Appendix B.

Additionally, we further assessed the performance of devices in excess of 80 wt.% loading achieved through slightly elevated melt temperatures of 175°C. Compared to the state-of-the-art, this is the first vapor infiltration method that preferentially coats nanoporous regions and exhibits competitive performance with coating uniformity that activates the cathode performance across all metrics – indicating well-rounded behavior critical for practical devices. We also demonstrate the capability to scale-up this process to a benchtop roll-to-roll coating platform that leverages the > 60x throughput and > 5x lower energy requirement to liberate commercialization barriers for lithium-sulfur batteries.

4.2 Experimental Details

4.2.1 Film Fabrication

To fabricate carbon films, 50/50 mixtures of single-walled carbon nanotubes (NanoIntegris) and carbon black particles (Super C45, MTI) (SWCNT/CB) were bath sonicated in N-Methyl-2-pyrrolidone (Aldrich, 99.8% anyhdrous)) for 1 hour at a concentration of 2mg/mL. The solution was then cast onto stainless steel mesh discs and dried for 12 hours under vacuum.

4.2.2 Sulfur Infiltration

To achieve sulfur deposition, the carbon-loaded mesh discs were placed on a slightly raised surface inside a small sealed stainless steel vessel with a reservoir of 10 mg of sulfur powder (Sigma Aldrich, 99.98%).) beneath the electrode. The entire vessel was heated to 155°C for 45 minutes and the electrodes obtained an average sulfur loading of 74 wt %. For kinetic study of the infiltration other temperatures were used (135 and

175°C) for various set times. Sulfur loadings were assessed using a microbalance before and after infiltration. To verify the accuracy of this measurement, TGA analysis was used assure the same loading was observed (Figure 4.1).

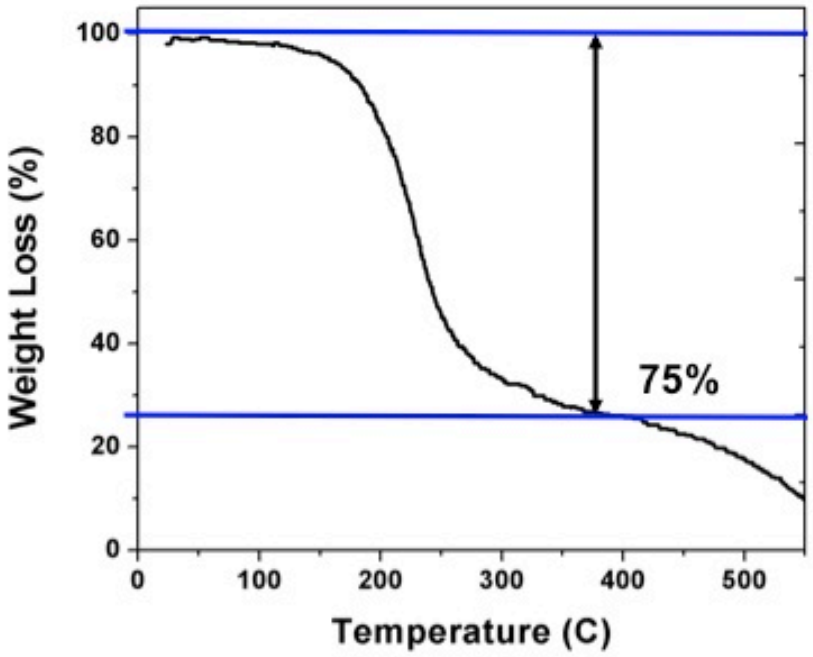

Figure 4.1- Thermogravametric analysis of electrode material showing 75% mass loading of sulfur agreeing with the microbalance analysis (75 wt.% S) carried out before and after vapor phase sulfur infiltration. This study validates use of the microbalance to assess sulfur loading on various samples throughout the work.

4.2.3 Electrochemical Testing

The electrode was directly employed as cathode in a CR 2032 stainless steel coin cell (MTI) with a lithium foil anode, 2500 Celgard separator wetted with 1M LiTFSi (Aldrich, 99.95 %), 0.25M $LiNO_3$ (Aldrich, 99.99 %) in a 1:1 mixture of DME (Aldrich, anhydrous 99.5 %) and DOL (Aldrich, anhydrous 99.8 %). The coin cell and electrolyte were prepared in an argon glove box with <0.5 ppm O_2.

4.2.4 Melt Infiltration Control Sample

In order to directly compare our lithium sulfur battery cathode with the typical melt infiltration method, a 50/50 SWCNT/CB powder was combined with powder sulfur in a 1:9 ratio by mass. Melt infiltration was performed by heating the carbon/sulfur composite to 155ºC for 12 hours. The resulting melt infiltration loading was 86 wt% sulfur. This composite was then mixed with CB and PVDF in 85:7:7 by weight and a few drops of NMP and bath sonicated for 1 hour. This solution was then cast onto stainless steel mesh electrodes for a resulting sulfur loading of 74 wt% which is equivalent to the loading obtained through vapor-phase condensation. The cathode was fabricated into coin cells in the same manner as the previous samples. Electrical testing was carried out using an MTI 8 channel battery analyzer and Electrochemical Impedance Spectroscopy was performed using a NOVA Autolab system.

4.2.5 Material Characterization

Scanning Electron Microscopy (SEM) (Zeiss, Merlin) and Scanning Electron Microscopy Energy Dispersive X- ray Spectroscopy (STEM EDS) (Osiris) were performed.

4.3 Results and Discussion

The general thermodynamic concept of rapid isothermal vapor infiltration of sulfur into carbon scaffolds is presented in Figure 4.1. In this process, liquid sulfur maintained in a sealed chamber at low temperature (< 175ºC) reaches thermodynamic equilibrium through the generation of a fixed vapor pressure of sulfur in the chamber. A carbon-based template for supporting the sulfur cathode, which is composed, in our case of pre-formed combined single-walled carbon nanotubes and carbon black material, is placed at a height

of ~ 1 mm above a reservoir of molten sulfur at the base of the sealed container. Conventionally, one would expect a fully isothermal system to exhibit balanced mass transport of sulfur vapor to and from the carbon composite and therefore negligible sulfur coating. To achieve condensation onto the composite a thermal gradient can be introduced, such as in the sulfur frost (low-pressure vapor deposition) method,[158] but this leads to thick surface coatings of sulfur as opposed to conformally coated carbon cathodes.[159] To overcome this challenge, we devised a fully *isothermal* system for sulfur infiltration where no thermal gradient is introduced. This is enabled by capillary condensation of the sulfur vapor, driven by the high surface free energy of the nanoscale pores and curved surfaces in the carbon materials.[160] At the point of nucleation, the high radius of curvature at these sites leads to the preferential spontaneous nucleation of sulfur liquid on the cathode material in the smallest pore features due to the free-energy driven difference in chemical potential (μ) between the sulfur nuclei and the sulfur vapor (Figure 4.2).[160] After nucleation occurs, $\mu_{coating}$ remains greater than than μ_{bulk} leading to a process where further mass accumulation occurs until reaching an equilibrium state where $\mu_{coating} = \mu_{bulk}$, and the process is complete. The final equilibrium state involves a carbon material where all surfaces are conformally coated with a layer of sulfur such that the surface free energy of the coated cathode and the surface free energy of the bulk liquid are similar. This method of sulfur infiltration provides a self-limiting process whereby the amount of sulfur loaded into the material is determined by the material system and a repeatable, optimal loading of sulfur in the carbon matrix for desired cathode performance is consistently achieved.

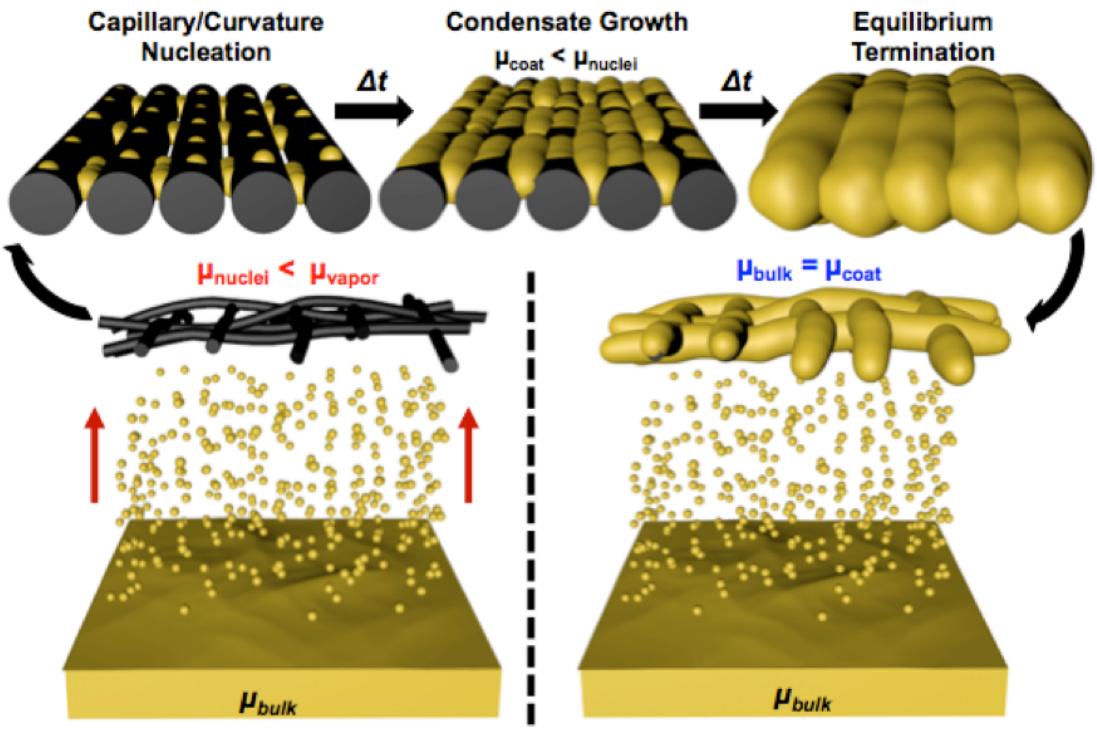

Figure 4.2- Schematic representation of the vapor- condensation infiltration process used to load pre-formed carbon anchoring materials with elemental sulfur. By maintaining a uniform temperature of the entire system to produce a sufficient vapor pressure of sulfur, capillary condensation in the porous regions of the electrode and on curved surfaces within the electrode facilitate liquid sulfur nucleation from the vapor phase. The driving force to coating the entire electrode relies on a minimization of the chemical potential of the liquid nuclei until the electrochemical potentials of both the bath and the coating are equivalent.

To investigate and verify the origin of this process, we carried out kinetic studies where the SWCNT-CB cathode material was exposed to different durations of isothermal treatment at three different temperatures (135 °C, 155 °C, and 175 °C) and the total specific sulfur loading was measured (Figure 4.3A). In all cases, decaying exponential loading curves were obtained indicating temperature-activated kinetics in accordance with Figure 4.3. By fitting these kinetic profiles (Figure 4.3B), we extracted values for the sulfur

growth rate (ν), the characteristic time for equilibrium sulfur coating (τ), and the activation energy (E_A) for the continuous isothermal growth of sulfur onto the cathode template. After less than 60 minutes of total isothermal processing, sulfur loading > 70 wt.% relative to all components of the carbon cathode is achieved.

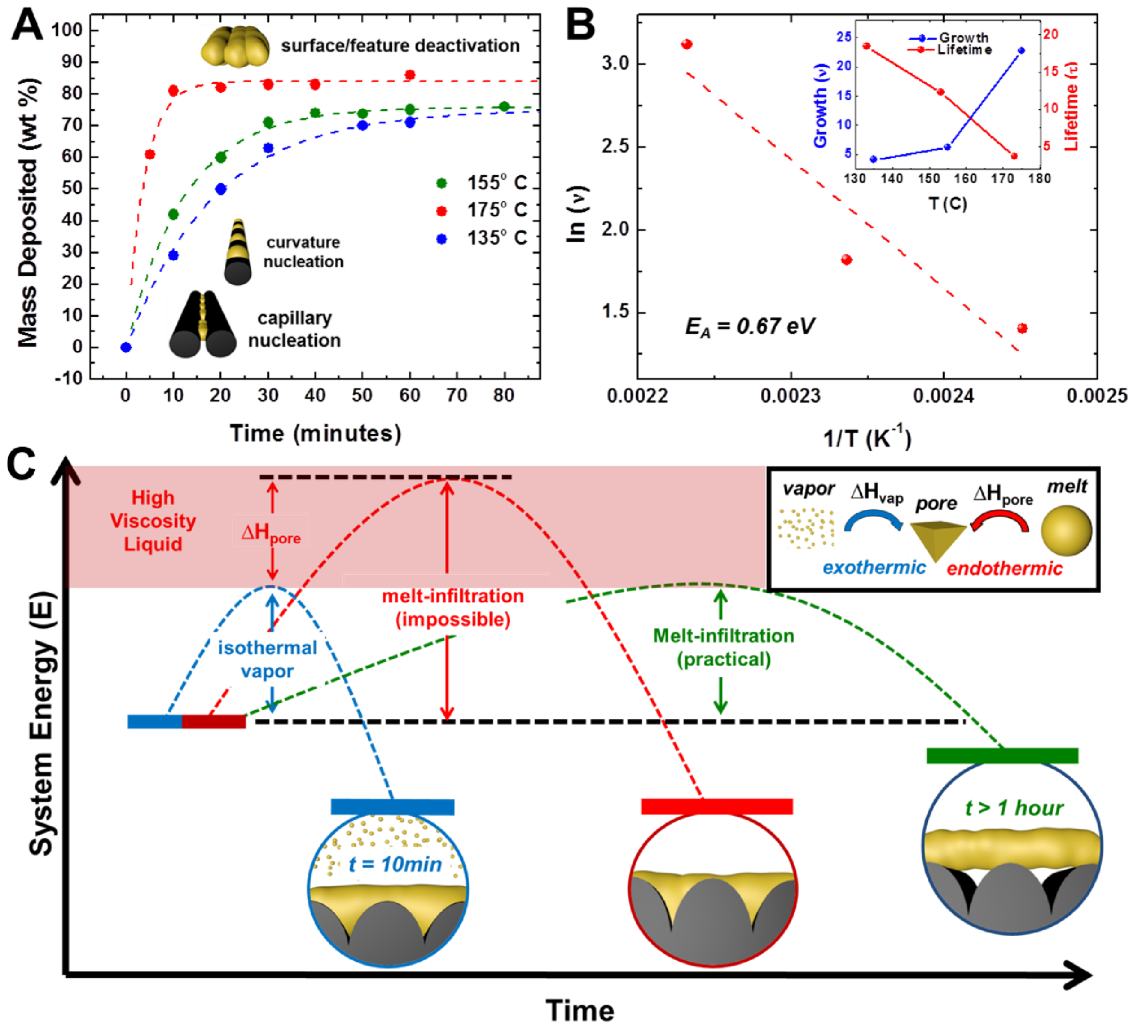

Figure 4.3- A. Sulfur loading with respect to time for three different temperatures using the vapor-condensation process with inset schematics depicting condensation nucleation and saturation points. **B.** Arrhenius plot for the growth rate of the sulfur film vs. 1/T. A linear fit to the data is shown by a dotted line with an inset depicting the specific values for growth rate and lifetime obtained at each temperature. **C.** Energy diagram depicting the evolution of the system energy during the coating process.

At the highest temperature of 175ºC, we consistently observed both the fastest (~ 10 minutes), and the highest loading (~ 82 wt.% sulfur). By slightly decreasing the isothermal temperature to the same temperature used for melt infiltration (155 °C due to the low viscosity of liquid sulfur at this temperature),[91] an equilibrium loading of ~ 75% was achieved after 40 minutes. Compared to melt infiltration processes, our isothermal vapor process significantly decreases the time associated with sulfur cathode fabrication (melt infiltration requires 6-18 hours, yielding maximum >100X throughput improvement) and yields self-limited (conformal) coating that cannot be reliably prescribed using melt techniques. In comparison to cost of the NMP-based slurry fabrication, the requirement of a 6 hour melt-infiltration step yields over a 4X increase in the fabrication cost. We note that the vapor infiltrated cathodes were infiltrated from NMP prepared slurries produced using standard processing routes used in battery manufacturing. In comparison for the melt infiltrated sample, sulfur infiltration occurs in the cathode material via melt infiltration, and this bulk material is then further processed using NMP into a slurry cathode. Therefore, a direct comparison of the power consumption between these processes is valid since both routes have similar processing methodology. However, we make note that processing of the pre-formed carbon film using NMP processing (for vapor infiltration processing) is consistent with current practices utilized in the battery industry and provides a marked advantage for process integration onto a manufacturing line.

In this spirit, Figure 4.3 presents process pathways that illustrate the mechanistic difference in melt and vapor infiltration to explain the improved loading characteristics. During melt infiltration, the use of temperature (and time) enables the liquid sulfur to overcome the activation barrier to separate from bulk and fill the nanoscale voids in the

porous material. However, filling the smallest nanoscale pores with liquid – which implies increasing the free energy of the sulfur relative to that of bulk sulfur, only occurs when the temperature used in melt infiltration can overcome an energy barrier that increases as pore size decreases. In turn, prior studies using melt infiltration to produce highly nanoconfined Li-S cathode architectures yielded a trade-off of low specific loading less than ~ 50% for many studies and demonstrated the inability of sulfur to completely utilize the entire pore volume.[140-143] As emphasized in Figure 4.3, the ceiling of thermal energy that can be supplied to melt infiltration is limited by sulfur polymerization that occurs at temperature >160°C and causes increased viscosity in the liquid and slows the infiltration, limiting feasible melt infiltration temperatures to 155°C and below. On the other hand, for our vapor-condensation process the liquid melt properties have no impact on the coating process. In this process, the coating *initiates* as a nuclei that forms in the highest energy (smallest size) pores and crevices of the cathode material that are not accessible by melt infiltration. This leads to an ideally uniform and conformal coating where sulfur is able to access the smallest pores, yielding improved loading (up to 82 wt.%) in the smallest and most active pores in the cathode. Conformality of the coating is demonstrated by scanning electron microscope (SEM), Transmission electron microscope (TEM) images, and energy dispersive x-ray maps (Figure 4.4) that show uniform penetration of the sulfur into the SWCNT/CB composite material.

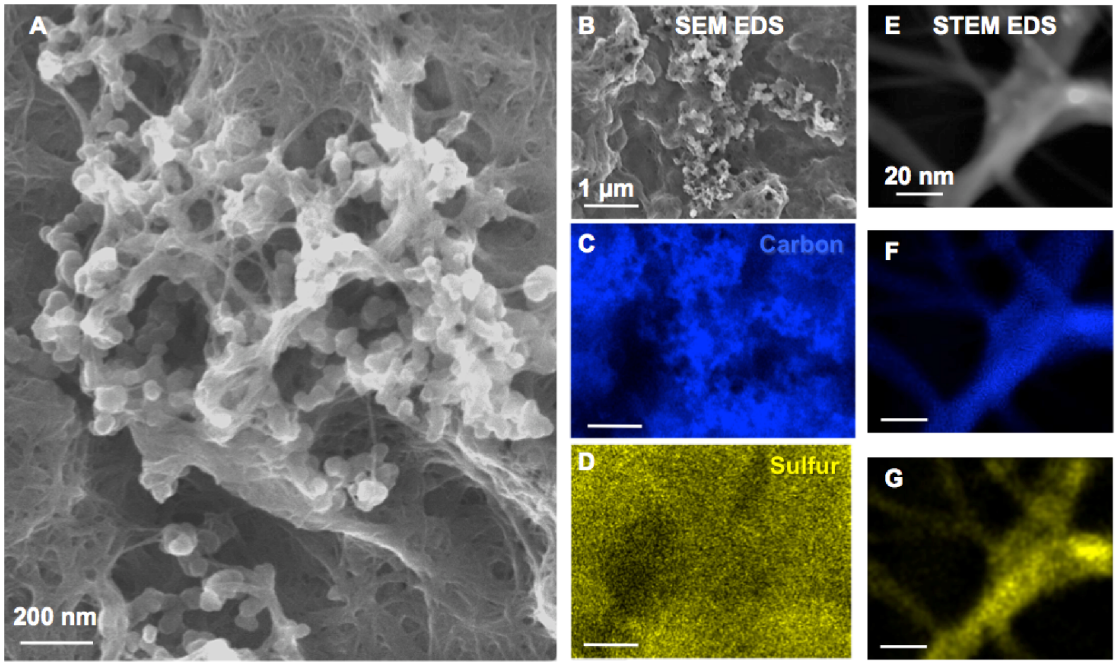

Figure 4.4- A. Scanning electron micrograph (SEM) showing surface morphology of 50/50 SWCNT/CB pre-formed carbon film a 74 wt.% sulfur loading. **B.** SEM image of the area over which energy dispersive x-ray spectroscopy (EDS) analysis was performed, **C.** SEM EDS map of elemental carbon and **D.** sulfur. **E.** scanning transmission spectroscopy image of a SWCNT bundle condensed with sulfur and corresponding **F**. STEM EDS elemental carbon map and **G.** STEM EDS sulfur map.

For isothermal sulfur vapor the total energy of the vapor is equivalent to $C_PT + H_{vap}$ and higher than that of the liquid used for melt infiltration (simply C_PT) at the same temperature, as a result of the phase change. This distinct difference provides sufficient energy to overcome the barrier to pore filling and achieve more uniform pore penetration. Based on principles of energy conservation, to achieve loading equivalent to the isothermal vapor with melt infiltration without a phase change, the temperature of molten sulfur must increase in accordance with the relationship $C_P\Delta T = H_{vap}$ where C_P is the heat capacity of molten sulfur (49.9 J mol^{-1} K^{-1}), and H_{vap} is the enthalpy of vaporization of

sulfur (9.8 kJ mol^{-1}) and ΔT is the difference in temperature for a sulfur liquid and sulfur vapor with the same energy. The melt infiltration technique theoretically could reach the same thermodynamic state as vapor infiltration at a temperature increased by 196ºC (351°C), which would require much greater input of energy to for system heating, even if time of infiltration was lowered, and remains impractical due to sulfur polymerization above 160ºC. Additionally, since our calculations indicate power consumption in cathode fabrication is largely dictated by the duration of infiltration, the fast kinetics and high loading achievable in this process can drastically improve the commercialization of sulfur batteries as nearly half of the total cost from traditional battery manufacturing originates from the fabrication process and cathode raw materials cost.[161-162]

Whereas the results so far give promise to improving lithium-sulfur battery cathodes, we further carried out experiments to test the effectiveness of sulfur cathodes produced using this technique compared to melt-infiltration. To present a robust comparison to melt infiltration techniques, we aimed for a side-by-side comparison of the same material template (SWCNT/CB) infiltrated at the same temperature (155°C) with the same sulfur loadings using both vapor infiltration and melt infiltration. Since the melt infiltrated sample required post treatment with carbon black and binder additives, total electrode loading was limited to 74 wt.%. This loading was chosen for the melt infiltration sample since higher loadings resulted in diminished conductivity of the composite cathode emphasizing poor uniformity of the contents. As this loading of 74% is easily prescribed in the vapor infiltration process at the melt infiltration temperature of 155ºC and reaches the >70% loading benchmark required for competing with state of the art Li-ion, we used this as a fair comparison of vapor infiltration to melt infiltration cathodes. Galvanostatic

testing of both cathodes at rate of 0.1 C (C = 1,675mA/g_{Sulfur}) are shown for the first cycle of both cathode materials in Figure 4.5A.

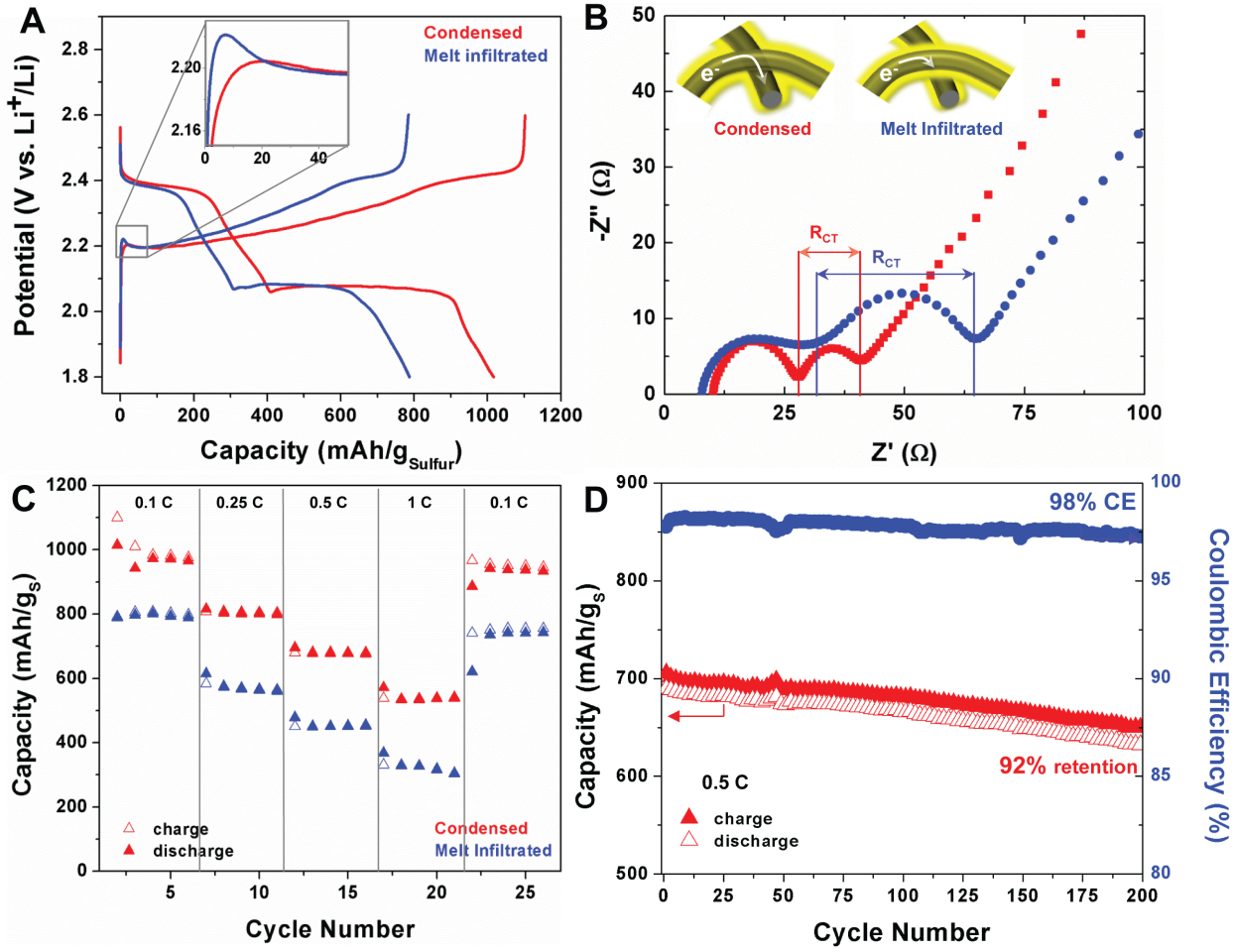

Figure 4.5- A. galvanostatic charge-discharge of a melt infiltrated and condensed cathode at 0.1 C with an inset depicting the potential barrier on charge. **B**. Corresponding Nyquist plots obtained using electrochemical impedance spectroscopy with a graphical inset of SWCNT junctions for each sulfur infiltration method explaining the variations in $R_{CT.}$ **C.** Galvanostatic rate study at 0.1, 0.25, 0.5, 1, and 0.1 C rates for each cathode and **D.** galvanostatic cycling behavior of vapor condensed cathode at 0.5 C over 200 cycles.

The vapor infiltrated cathode delivers an initial discharge capacity of 1015 mAh/g_S (~759 mAh/$g_{electrode}$) while the melt-infiltrated sample delivers 768 mAh/g_S (~568 mAh/$g_{electrode}$). The increase in initial discharge capacity and subsequently enhanced cyclability for the vapor-infiltrated cathode is attributed to both (i) an improved uniformity of the vapor coated sulfur film that extends into the narrowest pores in the material, and (ii) enhanced charge-transfer to the site of lithiation facilitated by the absence of additives and binders in the cathode material. Notably, by increasing the infiltration temperature slightly to 175°C, where melt infiltration is impractical, both mass loading and device performance are enhanced to ~ 80 wt.% at 175°C, (Figure 4.6) with initial discharge capacity of 1343 mAh/g_{sulfur} which corresponds to a capacity of 1087 mAh/$g_{electrode}$ – the second highest reported capacity to date (Table 5.1).

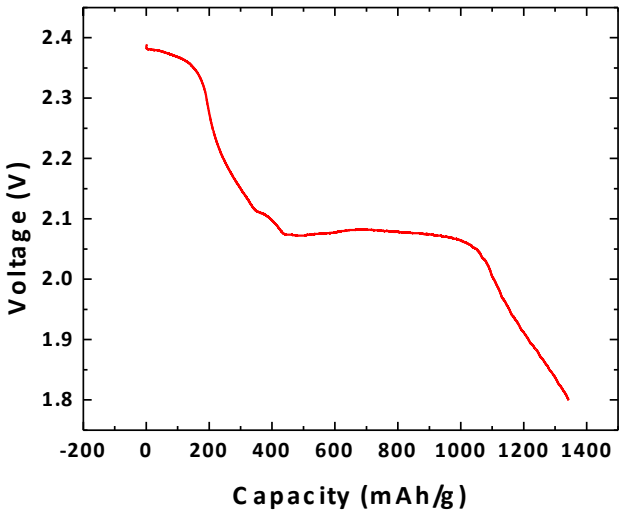

Figure 4.6- Initial galvanostatic discharge capacity for an electrode loaded with 80 wt.% sulfur at a rate of 0.05C. Notably, this corresponds to a total capacity normalized to the entire weight of the electrode of 1087 mAh/g, the second-highest capacity reported to-date.

The two cathode materials prepared by vapor and melt infiltration (74 wt.%) were further examined using Electrochemical Impedance Spectroscopy (EIS) measurements (Figure 4.5B). EIS indicates that the charge transfer resistance (R_{CT}) for the vapor infiltrated sulfur cathode is approximately 2X lower in comparison to the melt infiltrated cathode (full equivalent circuit fit in Figure 4.7 and Table 5.2). Here, R_{CT} represents the effective barrier for electron flow between the active site where lithiation occurs and the current collector. The results in Figure 4.5B suggest that (i) the vapor infiltrated cathode exhibits a less torturous pathway across SWCNT junctions that are required for electrical addressability, whereas melt infiltration processes clog the critical electrical transport pathways by insulating coatings of sulfur material (Figure 4.5B, inset), and (ii) the sulfur-carbon interface is more accessible due to more uniform infiltration using the vapor phase process. Additionally, when examining the cathode charge profile (Figure 4.5A, inset), the potential barrier prior to the first charge plateau that is characteristic to sulfur batteries is diminished for the vapor infiltrated sulfur cathode. This potential barrier is attributed to a barrier of charge transfer between electrolyte and insulating lithium sulfide during charging,[163] and this observation of a decreased barrier in the vapor infiltrated charge curve is consistent with the measurements obtained through EIS.

To further analyze the device performance, each cathode was tested with rates of 0.1 C, 0.25 C, 0.5 C and 1 C for 5 cycles each, followed by 5 cycles at the slowest rate of 0.1 C. The charge and discharge capacity of each cycle for the melt infiltrated and condensed samples are shown in Figure 4.5C. The vapor infiltrated sulfur cathode delivers excellent rate capability with ~575 mAh/g_S at 1 C, indicating over 50% retention at 10X the initial charging rate. We also note that the uniformity of the coating is observed to

mitigate the effects of polysulfide shuttling and improve the cycling performance as rate is altered.

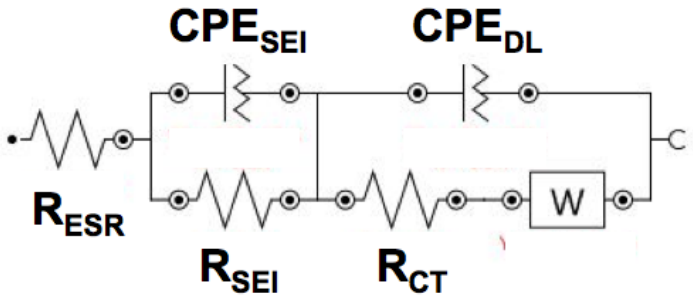

Figure 4.7- Electrochemical Impedance Circuit used for fitting EIS data shown in Figure 4.4B.

Fitting Parameter	Melt Infiltrated	Vapor Infiltrated
R_{ESR} (Ω)	7.33	9.98
R_{SEI} (Ω)	22.8	17.9
CPE_{SEI} (μMho)	14, N=0.747	7.86, N=0.837
R_{CT} (Ω)	33.6	12.9
CPE_{DL} (μMho)	569, N=0.734	1810, N=0.847
W (mMho)	40.4	90.6
X^2	0.06	0.02

Table 4.2- EIS Circuit Fitting Values for the melt infiltrated cathode and isothermal vapor infiltrated cathode in device architectures

Over the course of 100 cycles at a rate of 0.5 C, the vapor infiltrated cathode exhibits >96% capacity retention and after 200 cycles ~92% retention (Figure 4.5D). This relative capacity retention is improved compared to state-of-the-art reports[17, 164] while comparable melt-infiltrated devices with the same cathode materials and sulfur loading

exhibit only ~ 70% capacity retention (Table 5.1). This emphasizes, through a side-by-side comparison, that vapor phase infiltration leads to a cathode sulfur-carbon composite morphology that sustains better stability than melt infiltrated electrodes, without any modification to carbon host material. Additionally, the Coulombic efficiency at the 200th cycle is > 97%, which is an indicator of a stable and highly reversible conversion process. Whereas many reports indicate excellent cathode performance metrics in one area with trade-offs in other metrics, cathodes developed using this technique combine a quartet of key performance metrics that are collectively surpassing current state-of-the-art reports. This includes (1) a total cathode composite capacity of > 1,000 mAh/$g_{electrode}$ normalized to *all* cathode components, (2) >96% cycling retention at 0.5 C after 100 cycles, (3) specific sulfur loading above 70% with all cathodic components included, and (4) high Coulombic efficiency including ~98% efficiency after 200 cycles at 0.5 C. Combined with the lower energy footprint of vapor infiltration processing, this provides a straightforward process that can be widely adapted to improve lithium-sulfur battery performance to practical levels required for commercial impact.[165]

Beyond the lab-scale device performance and thermodynamic description of this process, the simplicity and reproducibility of this process can overcome key limitations that have hindered moving beyond current lithium-ion battery technology. For industrial-scale processing, the total number of steps, the duration of those steps, and the reliability of the process dictate the overall manufacturing cost in conjunction with the total energy input to the process, where vapor phase infiltration is superior. Unlike melt infiltration, vapor infiltration decouples the carbon electrode design and the sulfur infiltration steps, making these amenable to two consecutive (rapid) steps in a high throughput scale-up

battery manufacturing process. Here, a pre-formed carbon material can be coated from conventional water-based battery manufacturing routes and simply subjected to sulfur vapor infiltration to achieve a full battery cathode design in as little as 10 minutes (Figure 4.8A).

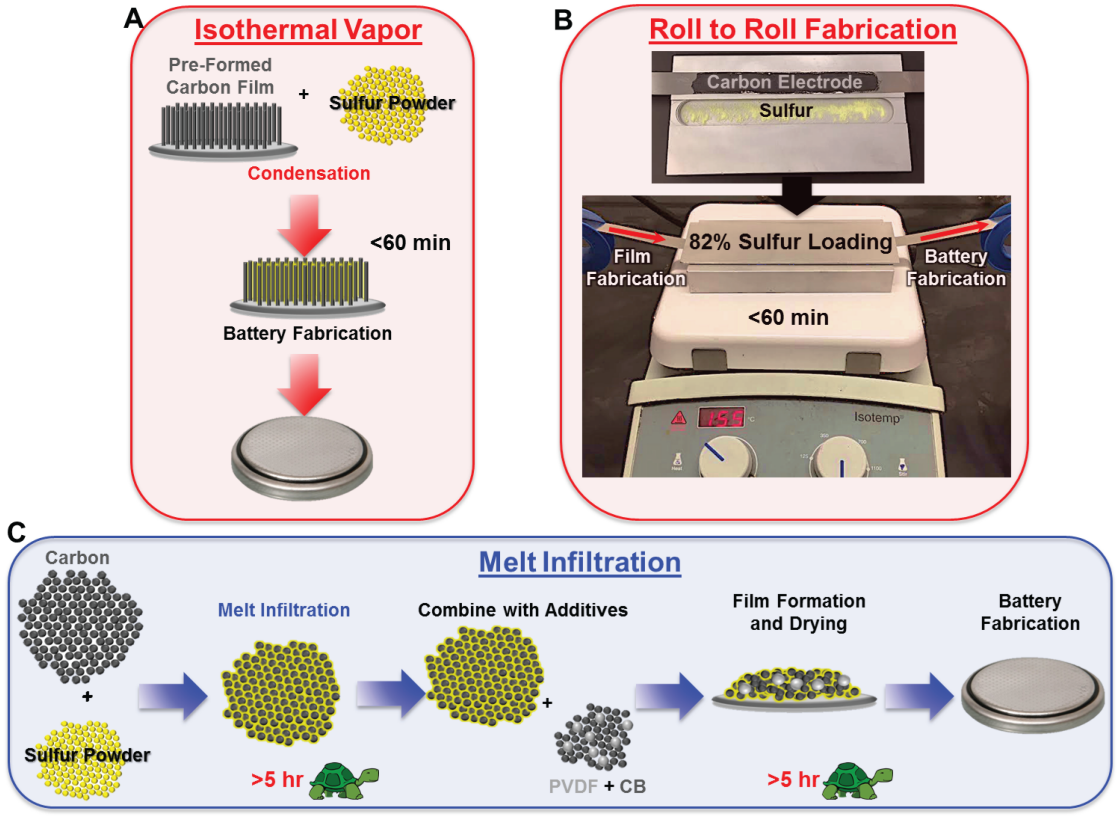

Figure 4.8- A. Schematic representation of the process for creating usable cathode materials from the vapor-infiltration process and corresponding **B.** optical photographs of a large-scale, roll-to-roll system using the vapor condensation sulfur loading process. **C.** Schematic illustration of the processing steps required for creating usable cathode materials from conventional melt infiltration processes.

Additionally, this vapor phase technique can be seamlessly "scaled down" where very small, engineered lab-scale samples can be reliably vapor infiltrated with sulfur on a "sample-by-sample" basis – a feature not achievable with melt infiltration. This can therefore provide a connection for the first time between researchers producing carbon nanostructured materials with highly controlled structure-property relationships and efforts aimed to engineer the next generation battery platform.

To further demonstrate the scaling-up of this approach, we developed a simple benchtop roll-to-roll platform (Figure 4.8B) where a coated film of SWCNT-CB on a 11 cm x 1.3 cm roll) was infiltrated with 82.5 wt.% sulfur by rolling the material through a system designed to operate on a simple bench-top hotplate. Since negligible sulfur coating occurs on bulk surfaces using this technique, full utilization of the sulfur can be achieved in this approach, and no additives or other components are necessary in the cathode manufacturing process. In contrast Figure 4.8C presents a representation of the total number of steps required in the processing of lithium-sulfur cathode material using conventional melt-infiltration, which is currently the primary route utilized to simultaneously achieve high loading and good device performance. In this approach, the melt-infiltration process typically requires between 6-18 hours duration for uniform infiltration of nanomaterials and only produces a material (not an electrode) which must be further processed into a cathode. This typically involves sonication of the material with a PVDF binder and carbon black after infiltration, which can then be cast and dried as a slurry into a cathode. The drying step is also slow (approx. 6 hours) leading to an overall sluggish process from composite elements to complete electrode. Overall, we believe that the improvement on all fronts enabled by this vapor phase infiltration

technique will liberate many of the current barriers that are limiting current advances in lithium-sulfur battery materials from penetrating the energy storage marketplace.

4.4 Conclusions

In summary, we demonstrate the first vapor phase coating process building on the thermodynamics of capillary condensation on nanoscale surfaces that is able to decouple the separate steps of carbon template fabrication and high loading sulfur infiltration. A side-by-side comparison between vapor phase infiltrated and melt infiltrated cathodes indicates improved device performance in all metrics of capacity, cycling performance, and Coulombic efficiency, as a result of improved uniformity and electrode conductivity and our vapor infiltration process enables uniform loading at > 80 wt.% sulfur. However, compared to melt infiltration where lab-scale composite preparation occurs over a matter of days, this approach is amenable to combination as a separate process in a battery manufacturing facility to produce a full cathode in a matter of minutes. On (smaller) laboratory scales, the versatility of this approach to be compatible with pre-formed carbon cathodes can enable meaningful routes to electrode design to engage a broader community centered on material synthesis efforts to overcome performance bottlenecks in next-generation battery systems. Overall, our work provides no reasoning for continued use of melt infiltration as a technique for nanostructured Li-S battery cathode preparation given points of simplicity, power consumption, throughput, combined metrics of device performance, reliability/controllability of high sulfur loading, and adoption with pre-

formed carbon templates that isothermal vapor phase infiltration exhibits, as we demonstrate in this work.

Chapter 5

Polysulfide Anchoring Mechanism Revealed by Atomic Layer Deposition of V_2O_5 and Sulfur-Filled Carbon Nanotubes for Lithium-Sulfur Batteries

Adapted from: R. Carter, L. Oakes, N. Muralidharan, A.P. Cohn, A. Douglas, and C.L. Pint, "Polysulfide anchoring mechanism revealed by atomic layer deposition of V2O5 and sulfur filled carbon nanotubes for lithium-sulfur batteries," ACS Appl. Mater. and Interfaces, 9, 7185-7192 (2017) *with permission from the American Chemical Society*.

5.1 Introduction

Compared to lithium ion batteries, lithium sulfur batteries boast up to a six-fold increase in energy density (up to 2500 Wh/kg) and leverage the low cost and earth abundance of sulfur.[13] Cathodes in lithium-sulfur batteries exhibit a conversion reaction where elemental sulfur (S_8) is first converted to high order polysulfides (Li_2S_x, $8 \geq x \geq 4$) near 2.3 V vs. Li^+/Li followed by complete reduction to Li_2S through formation of lower order polysulfides (Li_2S_y, $y \leq 2$) at 2.0 V.[164] The combined large volume expansion (>80%) required in this process and insulating nature of both elemental sulfur and the Li_2S_y (lower order polysulfide) discharge products inherently require implementation of a passive, mechanically robust, and conductive host for active sulfur that is capable of maintaining integrity during operation. Despite aggressive efforts by the research community to design scaffolds that can overcome electrode-scale limitations of polysulfide shuttling, or the capacity fade associated with dissolution of high order polysulfides,[166] this remains a

critical challenge for practical lithium-sulfur battery cathodes that results in different degrees of active sulfur mass loss, anode fouling, and self-discharge.[134]

Advances in anodes for sulfur battery configurations have included metal free anodes,[167] protected anodes,[168] and electrolyte additives.[82] However, cathode performance currently remains a limiting factor for lithium-sulfur batteries with strategies to sustain high performance segregated into two main categories: confinement and binding electrodes. Confinement electrodes employ micro-[141-142] and mesoporous carbons,[51, 80] carbon nanotubes,[81, 169-170] yolk-shell structures,[38, 48] and polysulfide trapping layers.[163]. Although unachievable to date, previous works have emphasized the idyllic desire to fill CNTs with sulfur for a highly effective confinement strategy.[12] Alternatively, binding electrodes utilize polar groups on the surface of composites including functional groups,[83, 171] metal oxides[45-46, 134, 164] or MXenes[172] to sustain a "stronger the binding, better the battery" principle[134] by providing controllable transition through intermediate polysulfides in localized regions minimizing polysulfide dissolution and enhancing conversion.[13, 46, 79, 134, 164, 172] However, early efforts with binding electrodes are limited by poorly conductive anchoring sites preventing efficient charge transfer, non-optimal particle size, and uncontrolled morphology due to reliance on wet chemical synthesis.[134] Atomic Layer Deposition (ALD) is a technique equipped to overcome these issues[50] and has been studied for metal oxide coatings applied to sulfur battery cathodes.[173-178] However, the necessity of coupling ALD processing with widely-used conventional melt-infiltration routes at electrode-scales requires coatings to be applied *over* the sulfur-carbon composites in all previously reported cases, causing resistive effects and hindering initial cathodic discharge behavior.

In this study we demonstrate the first report which overcomes the material processing bottlenecks of conventional melt infiltration to demonstrate the rational design of a nanostructured electrode material with simultaneously optimized binding and confinement properties. To accomplish this, carbon nanotubes were selected since sulfur can be loaded on the tube interior providing a robust charge-transfer pathway between the sulfur and carbon nanotube, while an anchoring layer can be produced on the tube exterior to allow the capture of soluble polysulfides. The cathode was fabricated by utilizing preformed carbon nanotubes assembled with electrophoretic deposition into binder-free electrodes,[66, 179] processed with highly polar V_2O_5 exterior surface coatings via ALD, and lastly interior infiltrated with sulfur (S_8) using a gas phase processing route leveraging the thermodynamics of capillary filling. We show that by tuning the ALD coating thickness on the CNT exterior, a trade-off exists between the (adverse) insulating nature of the anchoring layer that limits charge-transfer and the (positive) anchoring effect of soluble polysulfides that is critical to engineer in order to achieve optimized performance. Our resulting cathode effectively utilizes two unique polysulfide-confining methods physically isolated by the walls of the CNT scaffold for enhanced device stability. This work opens the door to atomically precise engineered electrode building blocks that can sustain performance requirements of future lithium-sulfur batteries.

5.1 Experimental Details

5.2.1 CNT Films

Multi-walled CNTs (cheaptubes 8-15 nm OD) were probe sonicated in N-Methyl-2-pyrrolidone (Aldrich, anhydrous 99.5%) for 1 hour at concentration 0.5 mg/mL to form well dispersed solutions. Electrophoretic deposition was then used to deposit uniform, interconnected films of CNTs on steel discs (MTI 15.5mm diameter). Steel discs attached to both counter and working electrodes were immersed into the CNT/NMP solution with a 0.5 cm separation and 100 V of potential for 5 minutes.[180-181] The working electrode was then dried under vacuum for 12 hours.

5.2.2 Atomic Layer Deposition

Following electrophoretic deposition, CNT materials were directly placed into a Gemstar 6" ALD system. The precursor, (98+%) Vanadium(V)tri-i-propoxy oxide (VTIP) with a chemical formula, $VO(OC_3H_7)_3$ was preheated to 55 ^{o}C before the process. Nanopure water (H_2O) obtained using a Millipore water purifier was used as the oxidizer. The precursor and the oxidizer manifolds were heated to 115 ^{o}C to prevent condensation effects. Ultra-high purity Argon was used as the carrier gas and a reaction temperature of 150 ^{o}C was maintained in the reaction chamber throughout the process. To obtain crystalline V_2O_5 , VTIP and water were pulsed for 2 seconds each with residence times of 1 second VTIP and 10 seconds water. This process was repeated 50, 75 or 100 times for each cathode type. According to previous reports, for formation of V_2O_5 under thermal ALD, longer residence of water compared to VTIP is required.[182] Ellipsometry control experiments were carried out on silicon wafer samples ALD coated using various

residence times, in order to select the 1:10 ratio (Figure 5.1A). In order to determine the desired residence time for thermal water, ellipsometry measurements were taken on silicon wafer samples with 50 cycles each of 1 second VTIP and 2, 10 and 30 seconds of water. The thickness of these sample show an exponentially decaying trend (Figure S1) and estimated error for these measurements are found in Figure S1. The residence time of 10 seconds was selected for all experiments. With this data the thickness per cycle was estimated to be ~0.7 Å (Figure 5.1B), correlating to coating thicknesses of 3.7 nm (50), 5.5 nm (75) and 7.4 nm (100 cycles).

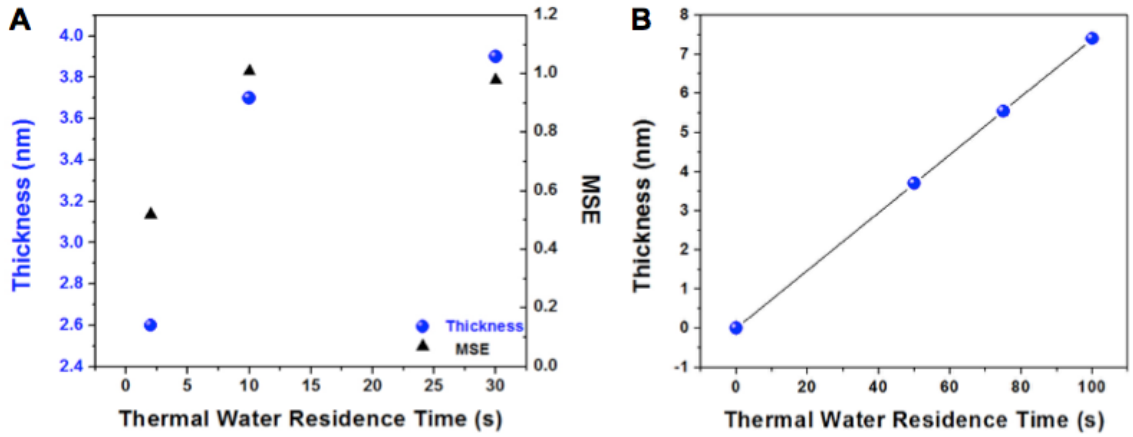

Figure 5.1- (A) Ellipsometry measurement of ALD coating thickness after 50 cycles with different residence times of thermal water on control plain silicon wafer. (B) Extrapolation of thickness for each tested cycle thickness based on Figure 5.1A.

5.2.3 Sulfur Infiltration

To achieve sulfur deposition, the carbon-loaded steel discs were placed on a slightly raised surface inside a small sealed stainless steel vessel (a modified coin cell) with a reservoir of 10 mg of sulfur powder (Sigma Aldrich 99.998%) beneath the

electrode. To experimentally achieve infiltration using this technique, the CNT substrate was placed above a sulfur reservoir (with ~ 0.2 mm separation) in a steel chamber maintained at a constant temperature of 155°C for 45 minutes, leading to an equilibrium sulfur vapor pressure of 28 Pa. The electrodes obtained sulfur loading of 65 wt % and areal mass loading of ~1.5 mg/cm^2 as characterized by mass microbalance measurements.

5.2.4 Characterization

The electrodes were directly employed as cathodes in a CR 2032 stainless steel coin cell (MTI) with a lithium foil anode, 2500 Celgard separator wetted with 1M LiTFSi (Aldirch 99.95%), 0.25M $LiNO_3$ (Aldrich 99.99%) in a 1:1 mixture of DME (Aldrich, 99.5%) and DOL (Aldrich 99.8%). The coin cell and electrolyte were prepared in an argon glove box (MBraun) with <0.5 ppm O_2. Galvanostatic charge/discharge was carried out using an MTI 8 channel battery analyzer. Electrochemical Impedance Spectroscopy (EIS) was carried out using Nova Autolab with AC potential of amplitude 0.1V over the frequency range of 0.02Hz -0.1MHz at the open circuit potential (OCV) of freshly fabricated cells. These cells were then subjected to one cyclic voltammagram at rate 0.1 mV/s, also on the Autolab, over the same voltage range tested galvanostatically. These cells were subsequently examined with EIS at the same potential as the first test.

Scanning Electron Microscopy (Zeiss) Transmission Electron Microscopy (TEM) and Scanning Transmission Electron Microscopy Energy Dispersive X-Ray Spectroscopy (STEM EDS) (Osiris) were preformed, as well as Raman Spectroscopy (Renishaw) and UV-Vis Spectroscopy (Cary). UV-Vis- The solution was prepared by overnight stirring of elemental sulfur and Li_2S in solvent with proper stoichiometric ratio resulting in a bright yellow solution with absorption features near 288 nm (S_6^{2-}, S_8) and 450 nm (S_6^{2-} and S_5^{2-}

chain-like polymeric species existing in solution).[183] Any existence of species differing from S_6^{2-} is a result of equilibrium transitions in the solution through different charge states (S_8-S_5^{2-}). This Li_2S_6 absorption signature was then compared with two solutions exhibiting identical concentration after stirring for 24 hours with CNTs with and without 75 cycles (5.5 nm) of V_2O_5 coating. CNTs were removed *via* centrifugation.

5.3 Results and Discussion

The rationale in studying V_2O_5 as an anchoring layer builds on recent modeling results from the Cui group elucidating V_2O_5 to exhibit the largest polar binding to lithium polysulfides in comparison to other metal oxides or nitrides, despite lack of experimental confirmation as an anchoring material for Li-S battery cathodes.[184] Whereas other studies have used ALD for Li-S batteries,[27-32] these techniques rely on ALD barrier coatings applied *over* the sulfur, which poses concerns about coating stability during volume expansion of the sulfur during lithiation, as well as thermal stability of the melt-infiltrated sulfur during high temperature ALD processing. The ideal ALD anchoring layer is one that (1) does not pose a charge transfer barrier for initial and subsequent sulfur conversion, (2) does not exhibit mechanical instability due to positioning above the sulfur coating, since extreme volume expansion will pulverize such materials, and (3) exhibits the strongest binding to soluble polysulfides. Notably, an electrode building block involving V_2O_5 coated onto the exterior of the CNTs and sulfur loaded on the interior of the CNT is a design that satisfies all of these points and is the basis for this study.

ALD coatings of V_2O_5 with different thicknesses were achieved on CNT films by controlling the number of sequential pulses of VTIP and water vapor coreactants.[182] STEM EDS maps (Figure 5.2A-D) of CNTs coated with V_2O_5 (vanadium and oxygen shown as red) and corresponding high resolution TEM images (Figure 5.2E-H) reveal the sequential growth of V_2O_5 with increasing ALD cycles on the surface of the CNTs.

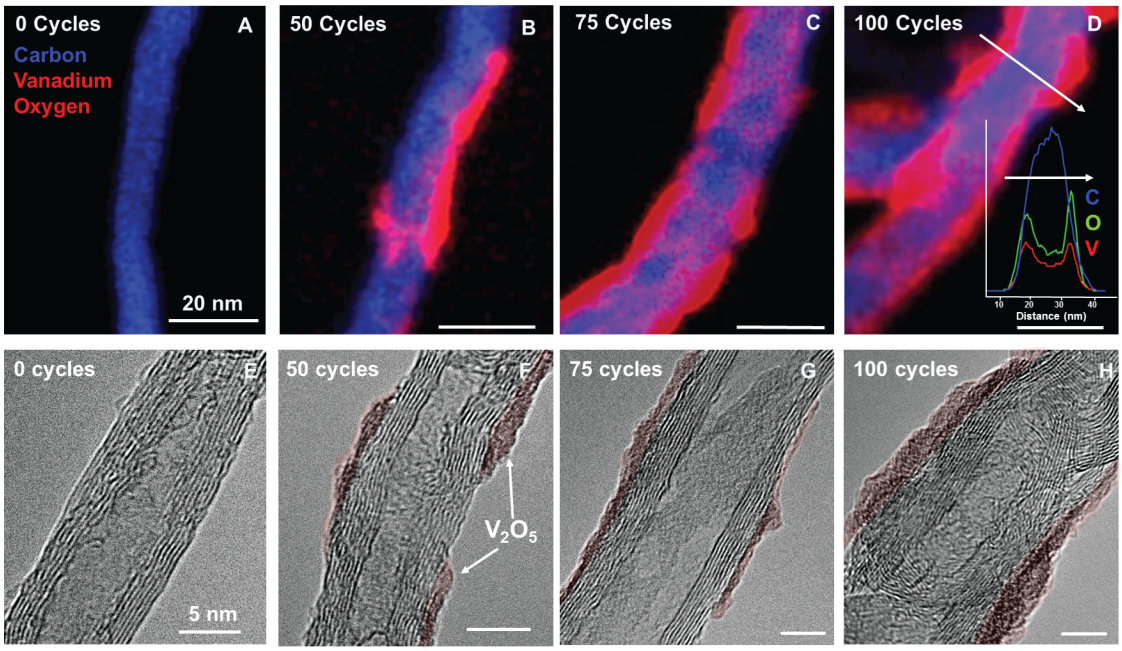

Figure 5.2- **A-D** STEM EDS elemental maps of MWCNTs with various numbers of ALD cycles of V_2O_5 0, 50, 75 and 100 respectively with carbon mapped as blue and both vanadium and oxygen as red (all scale bars 20 nm). Inset into Figure 5.2**D** is a line scan across the 100 cycle coated MWCNT with intensity plotted for carbon, vanadium, and oxygen. **E-H** high resolution TEM images of ALD conditions shown corresponded STEM EDS maps shown above, V_2O_5 highlighted with red shading, all scale bars 5 nm.

TEM images revealing layer-by-layer growth of disconnected islands until ~ 75-100 cycles when the V_2O_5 coatings appear continuous across CNT surfaces at thicknesses lower than those on flat surfaces measured using ellipsometry[55] as shown in Figure 5.2 (<4

nm compared to 7.4 nm at 100 cycles), as a result of lower seeding density on the surface of MWs compared to the native oxide on the wafers. To verify the spatial distribution of V_2O_5, a line scan included on the STEM EDS map (Figure 5.2D) demonstrates the V_2O_5 coating present on the exterior of the CNT evidenced by the bimodal distribution of oxygen and vanadium on the CNT edges.

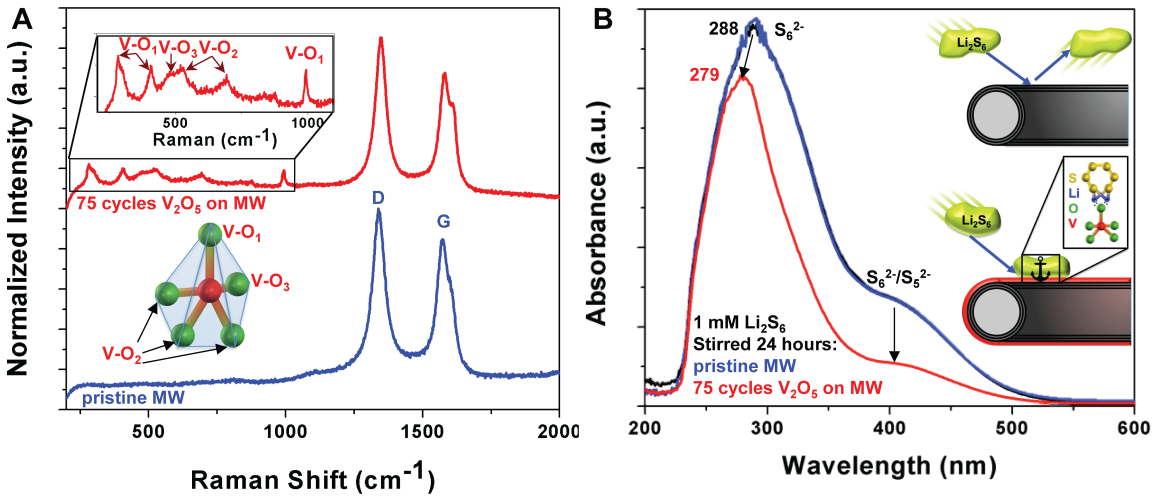

Figure 5.3. A Raman spectroscopy of pristine MWs and MWs coated with 75 cycles of V_2O_5, **B** UV-Vis spectroscopy of 1mM Li_2S_6 in DOL:DME before and after a 24 hour stir with pristine MW and MWs coated in 75 cycles of V_2O_5 (added MWs were removed with centrifuging). Inset in to Figure 5.3**B** is a schematic representation of the interaction between MWs and Li_2S_6 species.

To characterize the V_2O_5 coated CNTs, Raman spectroscopy with a 532 nm laser was carried out on ALD coated and uncoated CNTs (Figure 5.3A). In pristine CNTs, two prominent peaks near 1350 cm^{-1} and 1600 cm^{-1} correspond to the D (sp^3 carbon) and G (sp^2 carbon) peak with the high D peak intensity indicative of defects, ideal for ALD coatings as seed sites. CNTs coated with 75 cycles (5.5 nm) of V_2O_5 exhibit similar Raman

signature as the uncoated CNTs, but also exhibit several Raman modes in the 200 to 1000 cm^{-1} range attributed to crystalline V_2O_5. The inset of Figure 5.3A indicates Raman peaks correlating to the specific V-O stretches shown in the unit cell schematic.[185] Overall, Raman spectroscopy verifies the presence of crystalline V_2O_5 that has been highlighted in previous modeling efforts.[184]

In order to verify the exterior polysulfide anchoring capability of the V_2O_5 coating, UV-Vis spectroscopy experiments were performed to investigate the binding of polysulfides in 1 mM solutions of Li_2S_6 in DOL:DME (electrolyte solvents) to the electrode surface. The solution was prepared by overnight stirring of elemental sulfur and Li_2S in solvent with proper stoichiometric ratio resulting in a bright yellow solution with absorption features near 288 nm (S_6^{2-}, S_8) and 450 nm (S_6^{2-} and S_5^{2-}).[183] Notably, undetectable change was observed in the absorption profile when treated with uncoated CNTs in contrast to a significant drop in peak intensity and shift in position for V_2O_5 coated CNTs. The decrease in absorption is associated with the strong binding of V_2O_5 to Li_2S_6[184] and verifies the anchoring effect of the V_2O_5 in comparison to uncoated CNTs. Additionally, the shift of the prominent peak to lower wavelength (279 nm) reflects a peak position approaching dissolved elemental sulfur,[183] which when present in the solution has a much lower binding energy with V_2O_5 (~0.8 eV) in comparison to Li_2S_6 (~3.7 eV).[184] Schematic representation of this result (Figure 5.3B) illustrates the anchoring effect between a V_2O_5 unit cell and Li_2S_6 in contrast to a passive nonbinding surface of uncoated CNTs.

As our results verify exterior anchoring of polysulfides enabled by ALD coatings, the hollow interior of a CNT provides an ideally suited free volume for sulfur containment

that is both confined to a high aspect ratio geometry and fully electrically accessible through the conductive CNT interior layers. However, the most widespread approach to infiltrate sulfur into carbon materials (melt infiltration) relies on thermal processing of bulk sulfur with carbon materials to produce sulfur-carbon composites, where sulfur is tethered to external carbon surfaces. In turn, this widespread technique is not well adapted to target the filling of sulfur into CNT interior cavities,[170, 186] and is time and energy intensive due to the necessity to maintain melt temperatures under overnight durations. To overcome this, we developed a vapor phase process (Figure 5.4A) that leverages the thermodynamic concepts of the capillary effect to enable targeted filling of the CNT pores with sulfur. The capillary of MWCNTs provides sulfur condensate formation with concave shape indicative of a negative pressure difference facilitating sulfur filling of CNTs as the high pressure sulfur vapor will prefer to form liquid at a lower pressure inside the capillary of the tube. Similarly, droplet formation on the outer surface of the CNT is improbable due to its convex nature indicative of a positive pressure gradient – providing no thermodynamic conditions to sustain nucleation and growth of droplets on CNT exteriors. Notably, the surface tension of the sulfur droplet inside the CNT will also retain the negative radius of curvature inside the capillary (Fig. 5.4A) and lead to rapid filling of the CNT mediated through the vapor pressure. The duration of the filling is therefore limited by migration of enough sulfur vapor to the opening of a CNT to initiate a drop.

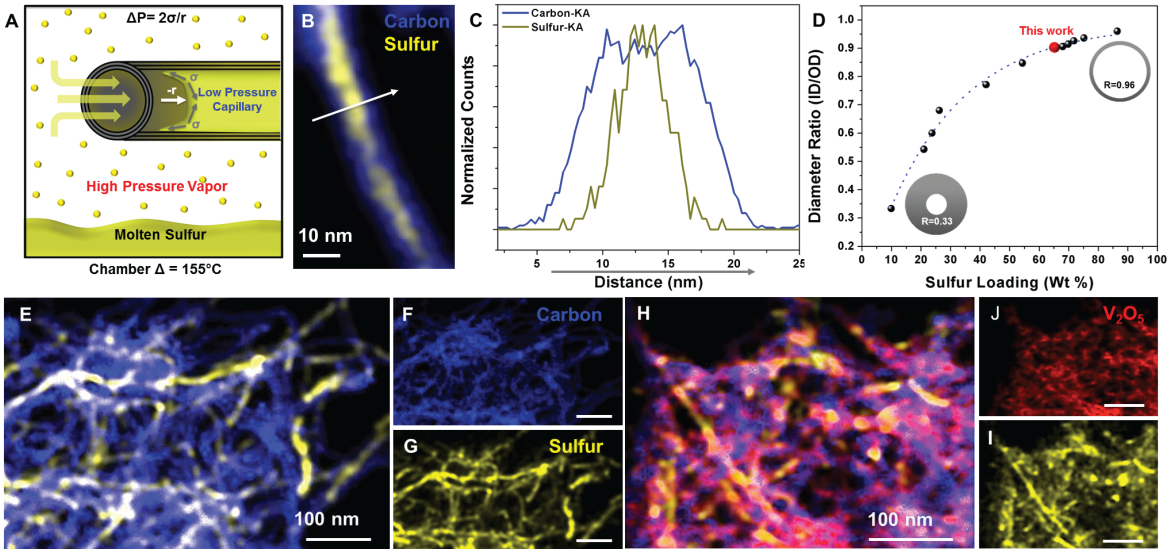

Figure 5.4- A Schematic depiction of sulfur infiltration process, **B** STEM EDS elemental map of carbon (blue) and sulfur (yellow) for a filled MWCNT, **C** line scan of indicated cross portion of Figure 5.4B. **D** Sulfur loading for various CNT geometries, **E-G** STEM EDS elemental map of pristine MWCNTs filled with sulfur and individual carbon **F** and sulfur **G** maps; **H-I** STEM EDS elemental maps of sulfur filled MWCNTs with 75 cycles of V_2O_5 and corresponding individual maps of sulfur *I* and vanadium and oxygen both mapped red **J.**

To characterize the sulfur-filled CNTs, STEM EDS elemental mapping was carried out on isolated sulfur-filled CNTs to characterize the location and presence of sulfur (Figure 5.4B). Line scans corresponding to this EDS map (Figure 5.4C) indicates a distribution of sulfur with maximum concentration in the middle of the CNT. This confirms the principle of capillary induced filling of CNTs, and notably reaches ~ 65 wt.% sulfur loading in the CNT material framework after only 45 minutes of thermal treatment at 155ºC (as opposed to an *overnight* treatment at the same temperature with melt infiltration). Whereas this is comparable sulfur loading to that typically achieved with melt infiltration, the use of vapor infiltration and CNTs eliminates need for conductive

additives and binders. Additionally, the capability to modulate both the number of walls and diameter (n, m ratio)[187] in a CNT presents a unique pathway to increase loading without compromising the integrity of the confinement or electrical accessibility (Figure 5.4D). The theoretical loadings of CNTs of different densities or ratio of ID/OD (inner diameter to outer diameter) were calculated based on previous studies. The factors altering this ratio are the number of walls and wrapping (n, m ratio and armchair, chiral or zig-zag) of the CNT. The loadings in Figure 5.4D were calculated with assumption of complete tube filling with each geometric condition. The relationship between loading and inner/outer diameter ratio fits an exponential decaying trend fitted to equation 3 where y_0 is 0.985 representing the highest ratio of inner outer diameter, A is -0.9371, and w_1 is 26.6, the rapidly approached loading. The fit had an R^2 of 0.99.

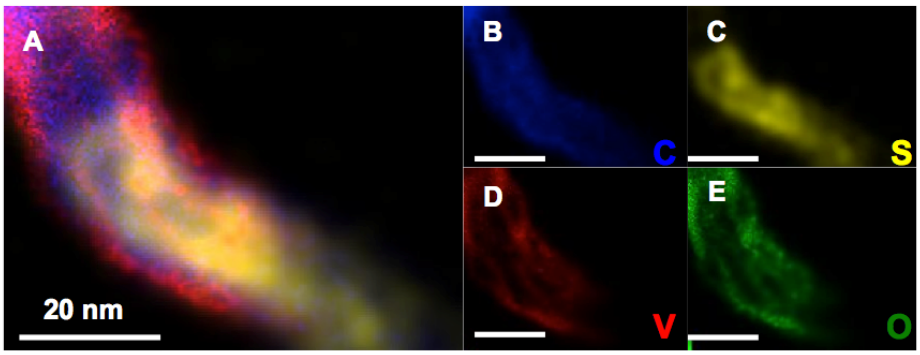

Figure 5.5- STEM EDS of sulfur filled MWCNT with 75 ALD cycles of V_2O_5 at the exterior **A** composite with elemental carbon-blue, sulfur-yellow, vanadium-red and oxygen-green, and individual element maps **B-E.**

Elemental maps of zoomed-out regions (Figures 3 E-G for uncoated, Figure 5.4 H-J for V_2O_5 coated with 75 ALD cycles) demonstrate uniform filling of sulfur achieved on

the interior of the CNTs even in the presence of the V_2O_5 anchoring layer formed on the surface. A high-resolution map of sulfur filled CNT with 5.5 nm (75 cycles) of V_2O_5 is provided in Figure 5.5.

As all experiments until this point support the mechanistic roles of polysulfide anchoring enabled by ALD surface coatings and interior containment and confinement of sulfur – both of which are critical ingredients for stable lithium-sulfur batteries, we performed electrochemical testing of these materials as cathodes in lithium-sulfur batteries. Galvanostatic charge-discharge at a slow rate of 0.1 C (C = 1675 mA/g) was carried out for 50 cycles on four sets of cathodes treated with 0 (uncoated), 50 (3.7 nm), 75 (5.5 nm), and 100 (7.4 nm) ALD cycles (Figure 5.6A).

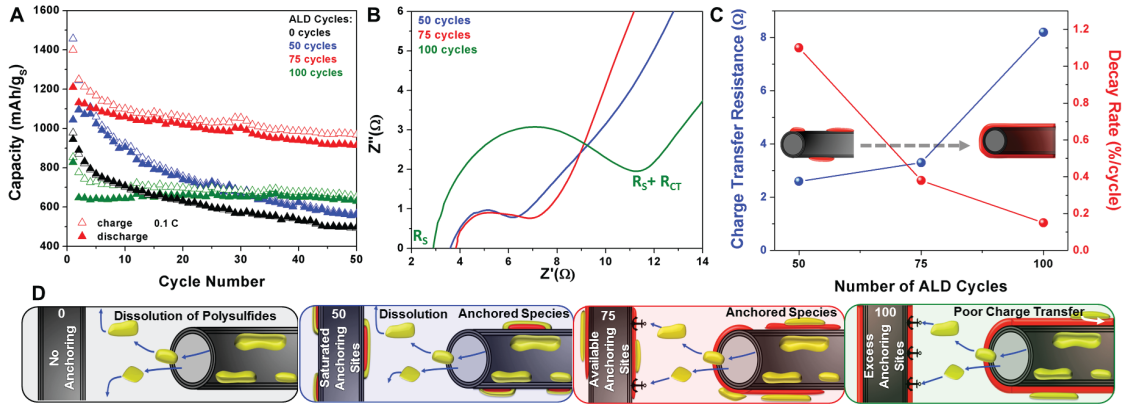

Figure 5.6- A Galvanostatic charge/discharge cycling at 0.1 C for 50 cycles with various ALD thicknesses of V_2O_5, **B** electrochemical impedance spectroscopy of V_2O_5 coated cathodes with thickness corresponding to 50, 75 and 100 ALD cycles, and taken after one complete cycle, **C** charge transfer resistance (R_{CT}) obtained from EIS measurement and galvanostatic charge discharge decay rate per cycle for each ALD thickness , **D** schematic representation of device performance with the different thicknesses of ALD V2O5 coating that ranges from (left) rapid capacity fade due to polysulfide dissolution to (right) good polysulfide retention but poor performance due to charge transfer resistance. 75 cycles, which forms an incomplete coating on the CNT, is observed to balance capacity, durability, and charge transfer resistance.

The corresponding charge discharge profile of each cathode is shown in Figure 5.7.

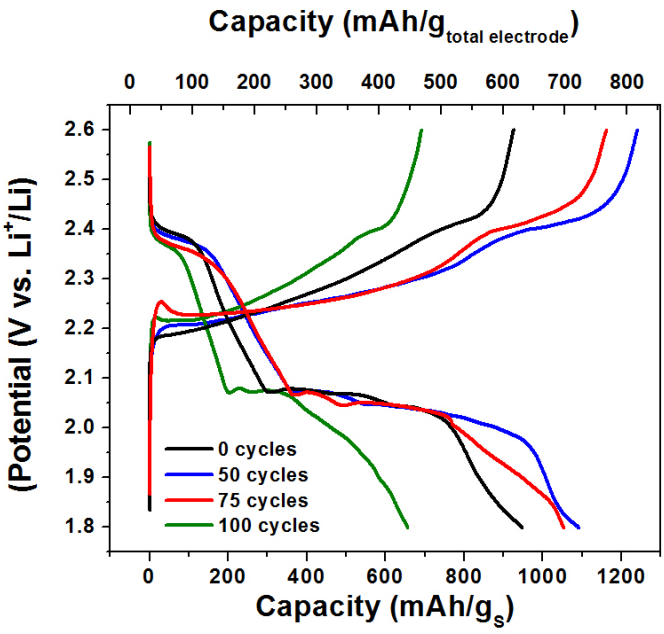

Figure 5.7- 2nd galvanstatic charge discharge cycle of cathodes with various number of ALD cycles (0- MW, 50, 75, 100). The observed sloping plateau from ~1.95-1.8 is the lithiation of V_2O_5 forming the γ phase.[188] This could be limited by cutting off the discharge before this reaction initiates.

For uncoated CNTs, initial discharge capacity is 945 mAh/g_s, but this capacity decays to ~ 600 mAh/g after only ~ 25 charge-discharge cycles, emphasizing the loss of active sulfur mass despite the interior confinement in the CNTs. With the thinnest application of V_2O_5 coating (~3.4 nm, 50 cycles), initial capacity increases to 1043 mAh/g_S as a result of initial slowing of self-discharge effects, but exhibits no noticeable effect on the polysulfide binding to mitigate capacity fade since V_2O_5 islands rapidly saturate (Figure 5.6C). However, with a modest coating of 75 cycles (5.5 nm) of V_2O_5, the maximum initial capacity is 1209 mAh/g_S, and exhibits stable cycling with over 3X lower capacity decay

(Figure 5.6C) compared to the thinnest V_2O_5 coatings (uncoated and 50 cycles). Finally, for the thickest V_2O_5 coating tested (7.4 nm, 100 ALD cycles), initial capacity is the lowest measured, 826 mAh/g_S, with the corresponding lowest capacity decay rate of all V_2O_5 coating thicknesses studied.

In order to elucidate the reason for the diminished initial capacity with 100 ALD cycles, electrochemical impedance spectroscopy (EIS) was carried out to examine the resistive elements in the system. Upon device fabrication each device had virtually equivalent spectra, since sulfur is confined in the CNTs for all electrodes. However, after one complete charge and discharge cycle polysulfide exterior anchoring is activated and the EIS spectra (Figure 5.6B) show district differences in the charge transfer resistances (R_{CT}) of the devices. Here, the R_{CT} is the real impedance (resistance) at the edge of the characteristic semicircle minus the series resistance (R_S) or resistance of the device where imaginary impedance is zero. The R_{CT} reveals the electronic barrier between the active sulfur material and the current collector. In the initial state since all the sulfur was contained in the CNT, this probed the CNT/sulfur interaction and all cathodes were identical, but exterior anchoring of polysulfides is initiated after the first cycle and differences observed directly relate to the V_2O_5 coating. As the coating transitions from seeding (50 cycles) to conformal (100 cycles) there is a distinct trade off (Figure 5.6C) between enhanced polysulfide anchoring (lower decay rate) and poor electrically accessibility through the coating (increased charge transfer resistance).

The device performance trends reveal a consistent picture between the importance of fine-tuning an anchoring layer to achieve the best cycling stability and the highest reversible capacity simultaneously, which is achieved with 75 ALD cycles of V_2O_5 (~5.5

nm). The minimal decay rates observed with 75 and 100 V_2O_5 coating cycles underline the mechanistic role of the polar oxide coating in mitigating polysulfide shuttling, but also opposes the idea that very strong polysulfide binding is undesirable in that it results in dissociation of polysulfides into Li^+ and S_x^{2-} and sulfur dissolution.[184] On the other hand, the lowest initial reversible capacity is achieved with the thickest ALD coating (100 cycles) where TEM imaging confirms a complete, conformal layer formed on the CNTs with <4 nm coating thickness and EIS reveals enhanced charge transfer resistance as the metal oxide anchoring layer impedes electronic conductivity between the conductive CNT and the active material limiting the reversible capacity, despite exceptional cycling characteristics. This balance between anchoring induced cycling stability and charge-transfer enabled polysulfide conversion is illustrated schematically in Figure 5.6D for each condition.

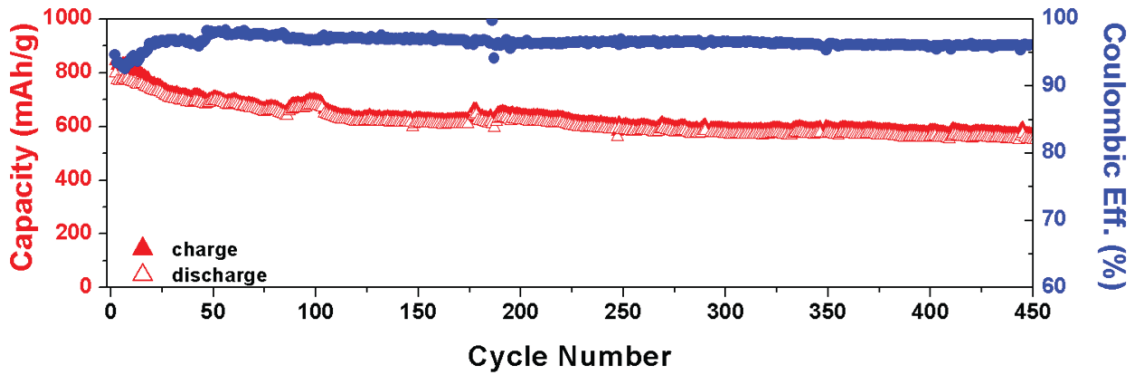

Figure 5.8. Durability tests over 450 cycles at 0.2 C using galvanostatic charge/discharge cycling on ideal sample prepared with 75 ALD cycles of V_2O_5. This indicates ~ 73% capacity retention after 450 cycles.

Finally, as our work highlights the condition of 75 ALD cycles of V_2O_5 as the optimum condition to balance storage capacity and cycling capability, an extended cycling study was carried out over 450 consecutive cycles (Figure 5.8) at a faster cycling rate of 0.2 C. The initial discharge capacity was 800 mAh/g (67% retention at twice the rate-) with 87% capacity retained at 100 cycles, and 74% capacity retained at completion of cycling at 450 cycles. This extended cycling performance confirms the synergy of CNT sulfur interior confinement and CNT sulfur exterior anchoring that elucidates the fine balance of conductive nature and polar binding surfaces for high performance sulfur cathode materials.

5.4 Conclusion

In summary, we present a route to transform a CNT into a precisely engineered nanoscale building block for lithium sulfur battery cathodes by utilizing the interior for fast capillary filling of sulfur, and providing a highly polar V_2O_5 anchoring layer on the exterior to mitigate polysulfide shuttling. This enables both good initial conversion of the loaded sulfur due to the sulfur proximity close to the conductive CNT interior, and retention of sulfur due to an incomplete V_2O_5 anchoring layer coating that optimizes the number of polar binding sites that have direct electrical connectivity to the CNT exterior. Our results verify the independent mechanistic roles of polysulfide surface anchoring of the V_2O_5 layer, and interior filling of the CNTs based on comprehensive optical characterization and elemental mapping in the TEM. Finally, we carry out device measurements that demonstrate a fine balance of decreased capacity fade using thicker (> 3 nm) V_2O_5 coatings, at the expense of a lower initial capacity limited by the insulating

nature of the polar binding layer. Our work highlights an optimal thickness for V_2O_5 with 75 ALD cycles (island-like ~ 2 nm coating) that maintains > 1200 mAh/g initial capacity at rates of 0.1 C, and sustains 87% and 73% capacity retention at 0.2 C after 100 and 450 cycles respectively. Collectively, our work gives promise to overcoming polysulfide shuttling to enable stable lithium-sulfur cathodes using nanoscale design routes and atomic layer deposition.

Chapter 6

High Areal Capacity Lithium Sulfur Battery Cathode by Site-Selective Vapor Infiltration of Hierarchical Carbon Nanotube Arrays

6.1 Introduction

Lithium sulfur batteries have emerged to be a promising battery chemistry for realizing heightened energy density and lowered price ($/kWh), which is critical for transportation and stationary (grid) storage applications.[129] This is due to an energy density about 6 times the theoretical limit of Li-ion technology with the two-electron transfer per active sulfur atom and the low-cost and abundance of elemental sulfur.[13] However, the necessity of a passive host material to buffer the volume expansion of sulfur upon lithiation and to provide a conductive matrix for the insulating sulfur has presented challenges to reaching the full potential of this conversion system.[12] Additionally, dissolution of high order polysulfides (HOPs), a paramount challenge that bottlenecks commercial viability, has drawn the focus of the majority of research in the area. This failure mechanism occurs as the elemental sulfur (stored as S_8 molecules) converts incrementally upon discharge to Li_2S_8, Li_2S_6, and Li_2S_4 products at ~2.3V, which are all soluble in commonly used ether-based electrolytes, prior to the lower voltage (~2.05 V) conversion to insoluble, high-energy Li_2S_2 and Li_2S products. Rapid dissolution of these initial HOPs results in active mass loss, anode fouling, and device failure.[79] However,

advances in electrode confinement,[21, 23, 143, 189] electrostatic polar binding materials,[49, 134, 164] and electrolyte additives[82] have proven highly effective.

As the significant research advances demonstrated for Li-S batteries has enabled strides toward commercial viability, direct comparison with Li-ion performance metrics is required.[18] Although reported cathodes can demonstrate gravimetric performances over 5 times that of Li-ion batteries, the typically thin (~1-2 mg_S/cm^2) electrodes cannot compete with areal capacities of 3-5 mAh/cm^2 common in Li-ion cells.[190] The insulating nature of active sulfur presents a significant challenge when attempting to develop thick or high areal loading cathodes capable of competing with Li-ion areal capacities and maintaining synergy of high throughput manufacturing practices used in the Li-ion battery industry.[150] Without comparable or better areal capacity than conventional Li-ion cells, sulfur cathodes will require a higher ratio of expensive and heavy current collector materials in the device architecture that can undermine the high gravimetric storage properties of sulfur.[12]

To enhance the conductivity of highly loaded sulfur electrodes, CNTs have emerged as a promising host. CNTs boast desirable traits including long-range conductivity, impressive mechanical strength, low density, and high aspect ratio geometries.[12] Vertically aligned CNTs uniformly infiltrated with sulfur are of particular interest for a sulfur cathode architecture providing high surface area, 1-D orientation enabling long-axis conductivity, and ease of electrolyte penetration.[12, 18] However, success of this architecture has been limited by the widely used infiltration method of melt diffusion that yields poor uniformity of sulfur deposits, destruction of the CNT array morphology, and agglomeration.[80] Such non-ideal and uncontrollable sulfur deposits lead

to poor sulfur utilization and ineffective confinement of soluble high order polysulfides.[61] Further efforts in CNT cathodes have attempted to mitigate failure by developing non-vertically aligned structures[191-192] and composites with other carbon nanomaterials[193-194] for enhanced structural integrity, or modified (partially unzipped[195] and porous[192]) and functionalized CNTs for enhanced polysulfide binding.[171, 193, 196-198] One of the more successful efforts by Jin *et. al.* employed a sulfur filled tube-in-tube CNT scaffold developed by way of chemical vapor deposition on an anodized alumina scaffold (200 nm pore size), coated with copper nanoparticles (~5 nm CNT growth), enabling sulfur mass loading of 68 wt.%, high discharge capacity, and strong rate capability, but with areal loading of only 2 mg/cm^2.[170] The work requires complex material processing and suffers from un-optimal CNT size preventing electrolyte penetration and reversible volume expansion.

In this study, we overcome past issues of (i) sulfur uniformity and utilization in pre-assembled or grown CNT arrays and (ii) scaling CNT-based sulfur cathodes to achieve high areal performance and thick electrode architectures. This is achieved by combining a site-selective vapor phase sulfur infiltration route (< 1 hr, 175°C) with a novel hierarchical CNT growth process that provides two populations of CNT diameters hierarchically distributed through a thick electrode architecture to simultaneously enable electrical access and mechanical integrity (large CNTs) and high gravimetric sulfur loading with high areal sulfur utilization (small CNTs). The vapor infiltration technique compliments this electrode architecture by temperature- and time-programmed sulfur loading to target sulfur filling of one or both of these populations. Whereas this enables a range of gravimetric and areal loading dictated by the combined hierarchical CNT and

vapor phase infiltration parameters, we demonstrate the capability to achieve simultaneous high gravimetric ~1100 mAh/g_S and areal 6.5 mAh/cm^2 capacity at 0.1 C with excellent rate capability using this technique.

6.2 Experimental Details

6. 2.1 CNT Scaffold Synthesis

CNTs were synthesized using the floating catalyst chemical vapor deposition (CVD) technique.[199-200] 1cm^2 thermally oxidized silicon substrates are placed inside a 24 mm diameter tube furnace and heated to 750°C under flow Ar and H_2 at 500 and 50 sccm, which remain flowing throughout the growth. To initiate CNT synthesis, a 10 wt % solution of ferrocene in xylenes was injected into the furnace held at 750 °C by a programmable syringe pump at a rate of 1.0 mL/h. The first generation of CNTs was carried out over 1 h.

In order to develop the second CNT growth, ALD was used to deposit alumina within the parent CNT forest. The precursor gases of water vapor and trimethylaluminum (TMA) were each introduced for 100 cycles at a processing temperature of 200 °C. The gaseous ALD precursors penetrate and deposit deep into the parent CNT forest rather than depositing on only the exterior forest surfaces. ALD alumina is known to promote the synthesis of small-diameter CNTs by stabilizing catalyst particles from Ostwald ripening and catalyst deactivation.[201-202] Utilizing these conditions, the nominal rate of alumina deposition is ~1.2 Å/cycle, leading to a coating ~12 nm thick for an ideal process. However, the low seeding density of the ALD chemistry on the CNT surfaces led to sparse formation of nanoparticles and continuous seeding that yields a low density of

alumina particles coated on the CNTs with diameters less than 12 nm. The alumina-coated CNTs were then subjected to a second round of floating catalyst CVD CNT synthesis using identical conditions to those used to create the first-generation forest but over half the time duration (30 min).

6.2.2 Sulfur Composites

Three different sulfur/CNT composites were developed using isothermal vapor infiltration.[69] The first was developed using only a single growth CNT array. This sample was suspended ~1mm above a sulfur reservoir (Sigma Aldrich 99.998%) in a small stainless steel vessel (modified CR 2032 coin cell) and heated to 175°C in an oven to establish an isothermal system maintaining sulfur vapor pressure of 78 Pa. This condition was maintained for 10 hours to obtain fully sulfur coated CNTs resulting in mass loading of 60 wt.% sulfur and areal of 3 mg_S/cm^2. The second composite was developed on a hierarchical CNT scaffold, where only the smaller second generation CNTs were infiltrated with sulfur. This selective coating was achieved through shorter duration vapor infiltration of only 1 hour. This composite also reached mass loading of 60 wt.% sulfur areal of ~6 mg_S/cm^2. The final composite was developed by carrying out the same condition infiltration on a hierarchical scaffold to achieve complete infiltration of both the small and large CNTs allowing high mass loading of 75 wt. % S areal of ~9 mg_S/cm^2.

6.2.3 Material Characterization

Scanning Electron Microscopy (Zeiss) Transmission Electron Microscopy (TEM) and Scanning Transmission Electron Microscopy Energy Dispersive X-Ray Spectroscopy (STEM EDS) (Osiris) were preformed, as well as Raman Spectroscopy (Renishaw). Due to the thickness of the cathode, STEM imaging was achieved by dislocating small portions

of material from the forest by abrading a copper grid across the CNT surface performed STEM EDS mapping.

6.2.4 Electrochemical Characterization

The electrodes were directly employed as cathodes in a CR 2032 stainless steel coin cell (MTI) with a lithium foil anode, 2400 Celgard separator wetted with 1M LiTFSi (Aldirch 99.95%), 0.25M $LiNO_3$ (Aldrich 99.99%) in a 1:1 mixture of DME (Aldrich, 99.5%) and DOL (Aldrich 99.8%). The coin cell and electrolyte were prepared in an argon glove box (MBraun) with <0.5 ppm O_2. Galvanostatic charge/discharge was carried out using an MTI 8 channel battery analyzer.

6.3 Results and Discussion

In order to develop a high-performance hierarchical CNT scaffold, the floating catalyst chemical vapor deposition (CVD) method was utilized to develop first and second generations.[199-200] A short (100 cycle) atomic layer deposition (ALD) coating of alumina was applied after the first generation to promote the synthesis of additional small-diameter CNTs from the sidewalls of the existing CNT array. These alumina particles stabilize CNT catalyst particles from Ostwald ripening and catalyst deactivation.[201-202] Schematic illustration of first vertically aligned CNT growth, (Figure 6.1A), followed by ALD (Figure 6.1B) and finally growth of second generation branched small-diameter CNTs, (Figure 6.1C) are shown in Figure 6.1. The alumina nanoparticle morphology depicted uniformly at the exterior of primary CNTs (Figure 6.1B), develops from the low seeding density of the ALD chemistry on the CNT surfaces.

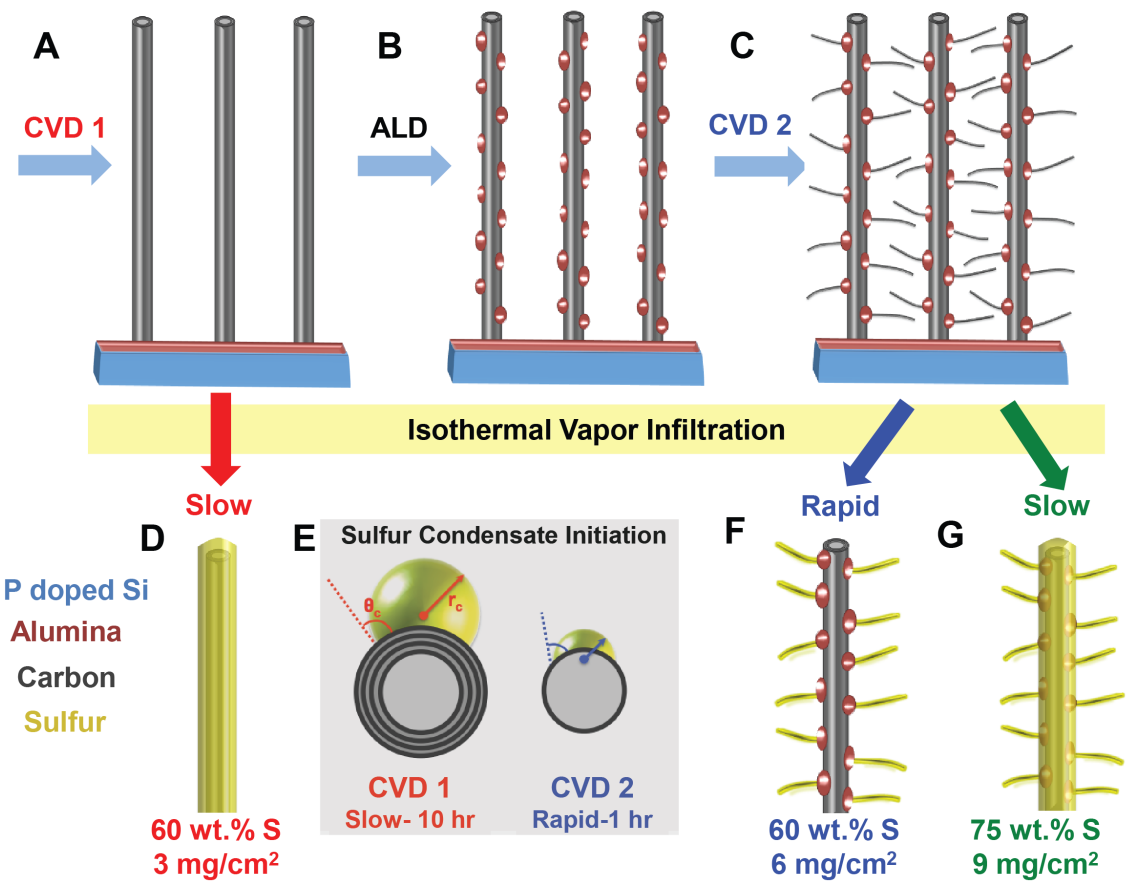

Figure 6.1- Schematic representation of sulfur cathode fabrication. Three types of sulfur cathodes were developed using novel isothermal vapor infiltration. The first comprises large primary CNTs **A** coated thickly with sulfur **D**. The second employs additional synthesis steps to yield small diameter CNT branches on thin submonolayer ALD coatings **B-C**. Site selective vapor infiltration of sulfur based on capillary filling thermodynamics illustrated in **E** are then used to target primary CNTs **D**, "branched only" CNTs in the hierarchical material **F** and both primary and branched CNTs **G**.

The CNTs were then controllably infiltrated with sulfur in the vapor phase at 175°C. The CNTs were situated at a distance from a bulk sulfur liquid, and sulfur condensation initiated from the vapor phase in an isothermal environment. The proper volume of vapor accumulated to form a drop of critical radius, dictated by the diameter of the carbon nanotube (Figure 6.1E).[69, 78] Since the larger CNTs require significantly larger

volume accumulation, the probability of droplet formation is lowered, slowing this process to ~10 hours, whereas the smaller diameter CNTs infiltrate in ~ 1 hour. This enables programmable sulfur infiltration with nucleation energetics governed by the diameter of the populations of CNTs. Based on the programmable deposition, three different sulfur condensate morphologies were developed in the CNT arrays to verify and understand the mechanistic role of structural hierarchy.

The first cathode type is developed by slow (10 hour) sulfur infiltration of only primary, single-growth (large diameter) CNT arrays, producing a thick sulfur coating on the surface of vertically aligned CNTs (Figure 6.1D). This sample is referred to as "primary only" to designate that the primary CNT layer is infiltrated with sulfur. The second cathode type is developed through fast (1 hour) infiltration of sulfur on hierarchical CNTs arrays, enabling selective thin coating on only second generation (small diameter) CNT "branches" (Figure 6.1F). This sample is designated as the "branch only" cathode. Finally, the last cathode is produced by slow (10 hour) infiltration of the hierarchical CNT array, which produced the highest mass loading, but combined both thick sulfur coating on the large diameter CNTs and thin accessible coatings on the small diameter CNTs. (Figure 6.1G). These three different sulfur infiltrations result in sequential enhancement of areal sulfur loadings with 3 mg/cm^2, 6 mg/cm^2 and 9 mg/cm^2 respectively, in accordance with enhanced scaffold filling, and correlated to mass loadings of 60, 60, and 75 wt.%. Although the second cathode type has double the areal loading of the first, it possesses the same mass loading due to the enhanced carbon host mass from the secondary CNT generation. However, introduction of the secondary growth enhances structural rigidity of the scaffold by 5X,[70] promising better accommodation of sulfur volume expansion for

stronger rate capability and cycling performance. The three types of cathodes allow for direct comparison of different CNT-based cathodes, where the first cathode represents theoretically ideal sulfur cathode geometry, the second utilizes our hierarchical design to enhance electrical conductivity and structural rigidity, and the last combines the two for assessment of ultra-high loadings.

To further investigate the synthesized CNT materials, scanning electron microscopy was used. Figure 6.2A shows the vertically aligned orientation of the primary multi-walled CNTs produced by floating catalyst growth at the p-doped silicon substrate. This primary growth results in array thickness of ~150 μm and areal loading of ~1 mg_{CNT}/cm^2. SEM imaging following the second generation growth confirms a uniform distribution of small-diameter CNTs nucleating from alumina catalyst supports residing on the first-generation CNTs. The alumina nanoparticles are <12 nm in diameter and remain thin enough to maintain electrical connectivity between parent and secondary CNT generations.[70] The particles are effective in supporting floating catalysts at the surface of primary CNTs, enabling small diameter growth, while preventing Ostwald ripening and catalyst deactivation. This branch growth mechanism at alumina nanoparticle supports is dominant in the second generation as no additional primary growth is observed at the p-doped silicon substrate.[70] Over the second growth process ~2 mg_{CNT}/cm^2 is produced, resulting in a hierarchical CNT array of ~3 mg_{CNT}/cm^2.

After rapid isothermal sulfur vapor processing of the hierarchical CNT scaffold, STEM EDS mapping was used to confirm selective sulfur deposition at the small diameter second growth CNTs. Composite elemental maps of carbon and sulfur show strong carbon signature (blue) across the large diameter CNTs with minimal sulfur response (yellow).

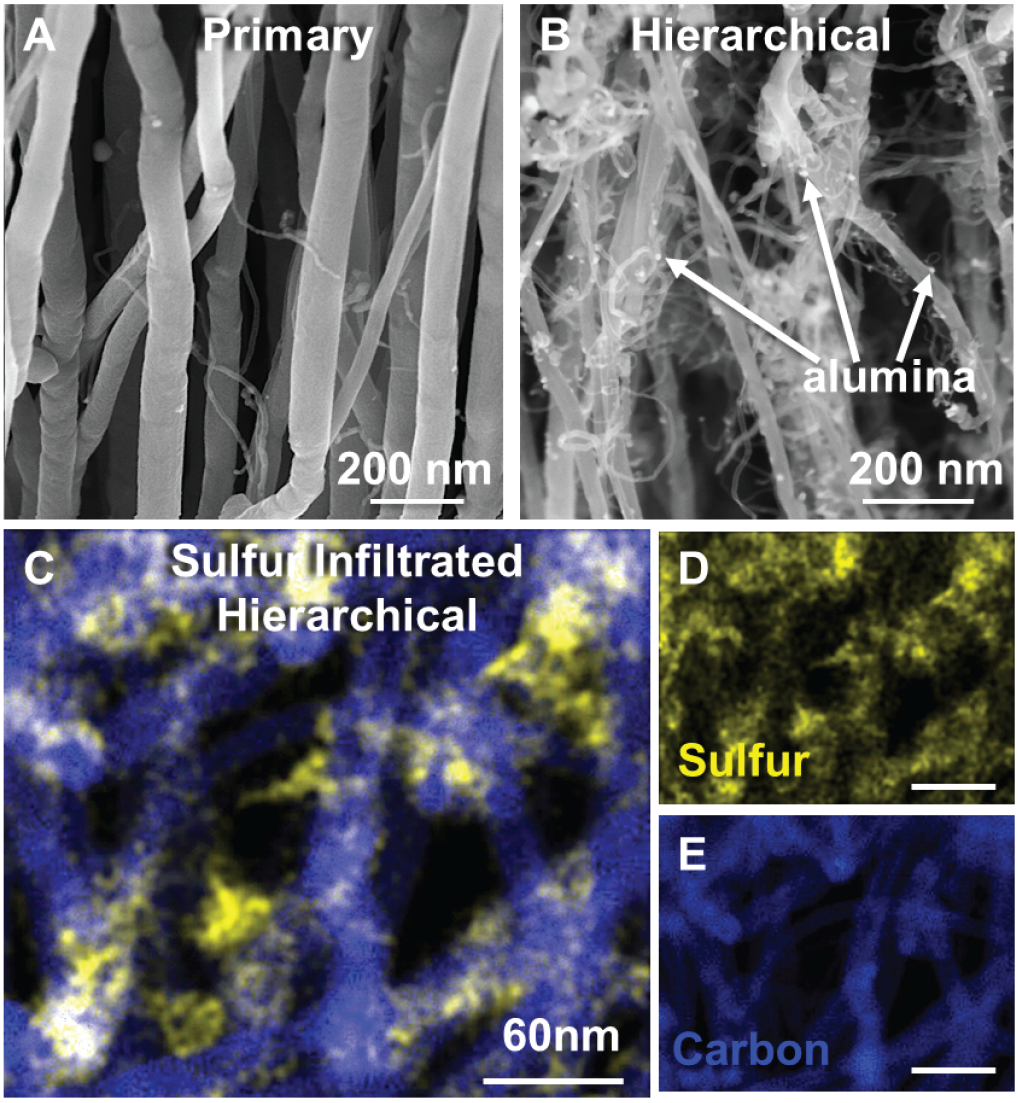

Figure 6.2- **A**. SEM image of primary CNTs and **B**. SEM image of final hierarchical CNT structure with thin ALD coated alumina dots that seed the small diameter CNTs labeled. **C**. STEM EDS composite elemental map showing carbon (blue) and sulfur (yellow) signature following rapid isothermal vapor phase infiltration, with individual carbon and sulfur maps shown in **D** and **E** respectively.

However, smaller diameter CNT clusters are observed in proximity to strong sulfur signature in elemental maps. The observed morphology and composition agrees well with our understanding of the sulfur vapor infiltration in the CNT forest, since the small CNTs

are infiltrated uniformly and thick coating at the larger diameter CNTs is not observed.

Directly following the vapor infiltration, the CNT scaffolds were assembled in coin cells (CR 2032) with lithium metal anodes, without need of excess processing with solvents or additive. The electrodes were electrically isolated using polymer separator (Celgard 2400) wetted with electrolyte (1M LiTFSI, 0.25M $LiNO_3$ in 1:1 DME:DOL). Our hierarchical scaffold with selective infiltration of "branch" CNTs (branch only, 60 wt.% S) was directly compared to the "primary" vertically aligned CNT scaffold (large diameter only, 60 wt.% S) using galvanostatic constant current discharge. An extreme overpotential (>300 mV) in the primary only cell limits the device capacity to less than half that of the "branch only" sample over the typical sulfur cathode voltage window (Figure 6.3A). This high overpotential observed with the "primary" vertically aligned cathode is a result of thick insulating sulfur coatings, required to achieve high mass loading on the charge carrying CNTs. In this arrangement, if conversion occurs at the sulfur surface contacting the electrolyte, high electrical resistance through the sulfur layer to the CNT will inhibit charge transfer required for reversible performance. This behavior is illustrated schematically in Figure 6.3B and further confirmed through electrochemical impedance spectroscopy (EIS).

EIS spectra of as-fabricated primary CNT and branched CNT devices are plotted on significantly different scales in Figure 6.3C, because of the drastic variance in magnitude between the two responses. The "branch only" cathode's entire device response occurs below the initially detected resistance in the "primary only" cathode (same scale plot found in the SI). The equivalent series resistance (ESR), or the first recorded point, indicative of the resistance between the two opposing current collectors of the device is ~3

times greater in the primary cathode compared to the branch cathode due to less ideal electrode-electrolyte interaction.[70]

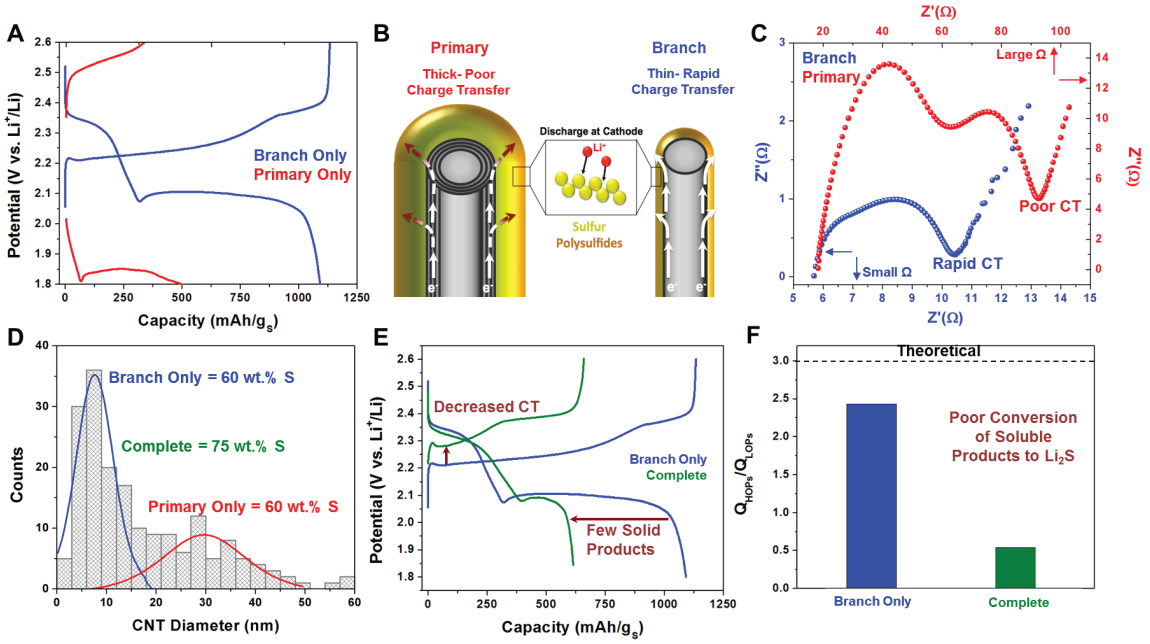

Figure 6.3- A. Galvanostaic charge discharge curves at 0.1 C for sulfur cathodes from infiltration of "primary only" and "branch only" CNTs. **B**. Schematic illustration of mechanism underlying the high overpotential for primary only CNTs in **A**. **C**. Electrochemical impedance spectroscopy over frequency range 0.05 Hz-1MHz on both "primary only" and "branch only" cathode types with axis at top right and bottom left respectively. **D.** Size distribution plot generated from TEM analysis of hierarchical CNT materials with labeled distributions indicative of the different CNT diameters in each generation. **E.** galvanostatic charge discharge profiles of branch only infiltrated and completely infiltrated CNTs. **F.** comparison of capacity contribution in the upper voltage discharge plateau (HOPs) to the capacity contribution in the lower voltage one (LOPs) emphasizing the role of hierarchy for better sulfur utilization and reversibility.

Additionally, the charge transfer resistance, or real impedance observed before the final linear increase after subtracting the ESR, is ~15 times higher in the "primary only" cathode. The significantly enhanced charge transfer resistance is a direct consequence of the thicker sulfur coating as illustrated in Figure 6.3B, and explains the extremely high

overpotential in galvanostatic cycling. The direct comparison of these two cathodes with equivalent mass loadings confirms that our hierarchical CNT design is far superior in device performance due to enhanced charge transfer and decreased sulfur thickness.

Our results emphasize that the high performance in the hierarchical CNT cathodes is due to the ability to command a branched and bimodal distribution of CNT diameters (Figure 6.3D) that enable electrical accessibility through thick electrode geometries and still maintain high sulfur utilization through optimal sulfur thickness in small-diameter CNTs. Whereas researchers have focused on lithium-sulfur cathode development to achieve either the highest areal loading or the highest gravimetric loading, our results emphasize the importance of balancing these to maintain high conversion and utilization of sulfur, through careful attention to sulfur morphology or ideal interaction with the conducting host. The sulfur conversion's (discharge capacity with respect to sulfur mass in the cathode) correlation to sulfur morphology is further evident in comparison of a "branch only" infiltrated hierarchical cathode to a completely infiltrated hierarchical cathode (Figure 6.3E). Whereas both samples indicate better performance than the "primary only" infiltrated CNTs, the "branch only" infiltration process yields a lower overpotential and significantly improved sulfur conversion ratio. By comparing the capacity of the low voltage plateau where the low order polysulfides (LOPs) are reduced from the higher voltage plateau (HOPs) capacity, the degree of cathode failure as a result of polysulfide dissolution can be assessed.[203] At theoretical maximum, the lower voltage LOPs conversion should deliver 3X the capacity of the HOPs conversion. When only the branch CNTs were infiltrated, a high performance ratio of ~2.5 is observed, indicating the thin layer resulting from isothermal infiltration is ideal for mitigating dissolution.

However, with a cathode having both parent and branch components fully sulfur infiltrated, the ratio is drastically diminished to ~ 0.5. Although the entire cathode is accessible as confirmed by an almost theoretical conversion of the HOPs (401 compared to 419 mAh/g_S theoretically), suboptimal surface area is provided for the final discharge product. Since much of the active sulfur remains dissolved in the electrolyte at completion of the discharge, the species are subsequently attracted to the lithium anode on charge. Additionally, on charging, the large volume occupying high resistance Li_2S products deposited on the larger CNTs are difficult to convert due to charge transfer limitations causing enhanced overpotential observed in Figure 6.3E. This is not the case for the "branch only" sulfur infiltration process where adequate surface area is available to accommodate thin coatings of sulfur that remain electrically accessible to enable fast conversion kinetics that sustains high sulfur utilization. This implies a critically important point for sulfur cathode design, in that sulfur conversion and utilization, parameters often disregarded in efforts to achieve the highest mass and areal loading, are dictated by the morphological properties of the sulfur coating on the carbon host material. In this manner, we highlight the hierarchical CNT with "branch only" infiltration to have the highest "quality" of sulfur infiltration, and this is the basis of further extensive device testing (Figure 6.4).

Figure 6.4A shows galvanostatic charge discharge curves from the first, second and fifth cycle at 0.1 C for the "branch only" cathode. The bottom axis indicates gravimetric capacity and the top axis indicates areal capacity. The corresponding discharge and charge capacities for 50 cycles, including these first 5 cycles from Figure 6.4A, are shown in Figure 6.4B. Over the first 8 cycles, capacity fade to ~78% retention of

initial discharge capacity and the subsequent behavior shows slowed decay (~0.4% per cycle).

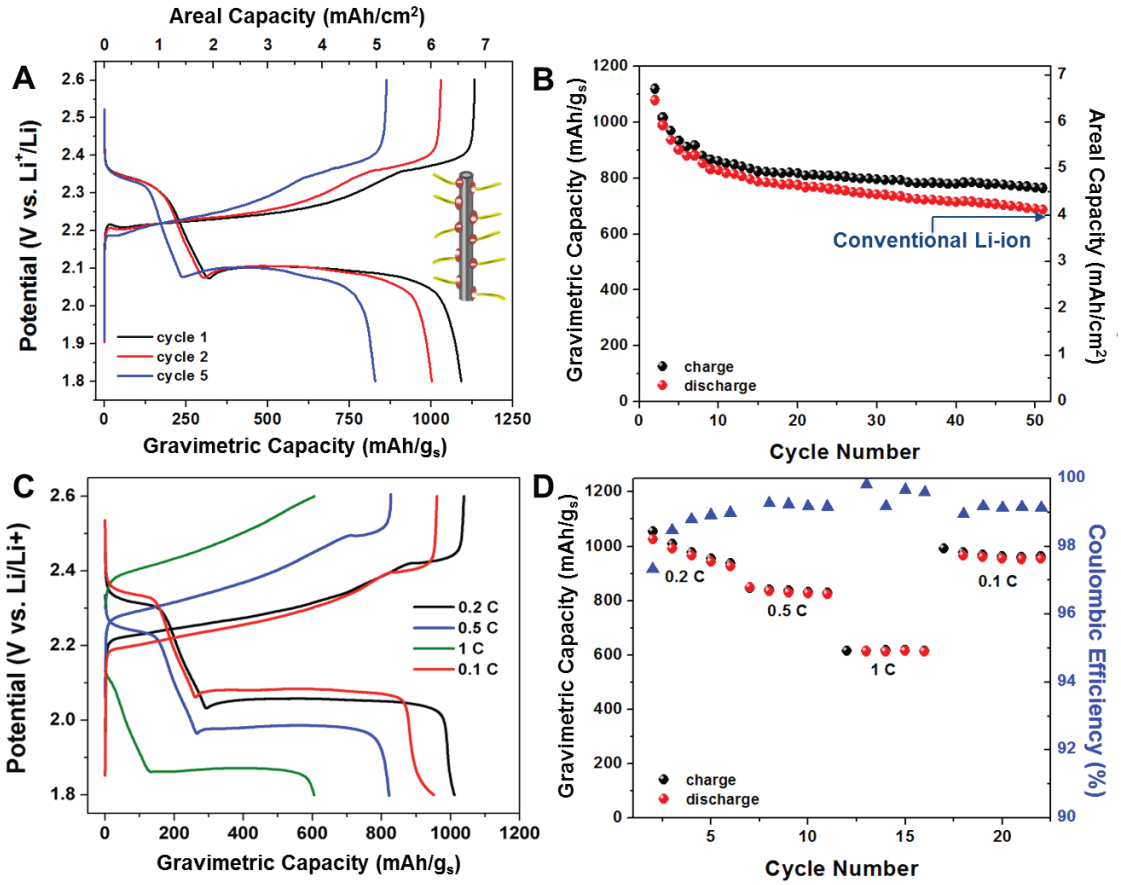

Figure 6.4- **A.** Galvanostatic charge discharge profiles acquired at rate of 0.1 C with inset schematic of "branch only" infiltration, **B.** cycling behavior of the cathode at 0.1 C with areal capacity shown at the right y-axis, **C.** charge discharge profiles at various cycling rates, **D.** rate capability for 5 cycles each with Coulombic efficiency shown as blue triangles correlating to the right y-axis.

Over the examined cycle range, the areal capacity remains over 4 mAh/cm^2 and sustaining areal performance was competitive with state-of-the-art Li-ion with significantly enhanced specific performance. In addition to the scaffold's impressive performance at the slow

charging rate 0.1 C, a cathode was tested over 5 cycles at higher rates of 0.2 C, 0.5 C and 1 C followed by the slow 0.1 C rate to assess its performance under higher currents. The galvanostatic charge discharge profiles at these rates are shown in Figure 6.4C and the corresponding charge and discharge capacities over the duration of the test are shown in Figure 6.4D. Notably about 60% of the discharge capacity is maintained even as the current is enhanced by 10X. The scaffold geometry allows for rapid transport of lithium and uninhibited charge transfer due to a low series resistance (~ 5.5 Ω) and is therefore ideal for high rate performance. This complete electrochemical characterization confirms the high performance of our hierarchical CNT scaffold design. The cathode delivers a high sulfur conversion capacity, 1092 mAh/g_S, competitive areal capacity of 6.5 mAh/cm^2, and impressive rate capability with 60% capacity retention at 10X the rate (1 C).

Overall, a key device outcome is that the sulfur morphology on the host carbon scaffold plays a critically important role to dictate the sulfur conversion and utilization, which are just as necessary as high loading methodologies to achieve high performance cathodes.[42, 171, 193, 204-211] Notably, as the most common method to prepare sulfur cathodes is melt diffusion, in which liquid sulfur is melt coated into bulk powders of carbons with uncontrolled distribution, until now careful and mechanistic characterization of the role of sulfur morphology in the resulting battery performance has been impossible. Here, we emphasize that vapor infiltration enables programmable and site-selective sulfur coatings that are necessary to achieve high sulfur utilization in solid sulfur-carbon composite cathodes and the site selectivity can be engineered through controllably synthesized hierarchical CNT materials with well-defined CNT diameter distributions that dictate condensation energetics. The balance of areal and mass performance of our design is

presented in Figure 6.5A compared with state of the art (studies from within the past two years, with specific references in SI) studies using various methods to prepare solid cathodes without use of externally fixed additional layers.

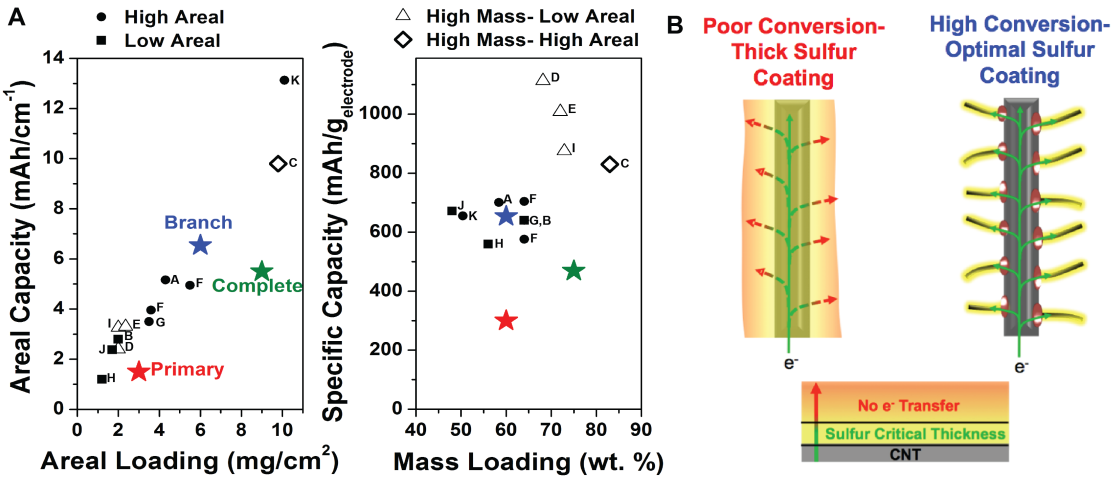

Figure 6.5- A. Comparison of finding from this study to other composite sulfur cathodes, emphasizing the importance of structural cathode design and high sulfur utilization in thick electrodes. Left panel shows trend of increasing areal capacity with areal loading revealing our branch cathode among the best performing solid cathodes. Right panel shows total electrode capacity (sulfur, host, and additive mass included) with respect to electrode sulfur loading. Our branch cathode proves competitive due to high sulfur utilization and controlled site-selective sulfur infiltration. **B**. Schematic explanation of the advantage of the hierarchical CNTs in developing effective thick sulfur electrodes, especially with ability to selectively infiltrate the small second generation CNTs.

Whereas the "fully infiltrated" hierarchical CNT material yielded the most appealing gravimetric and areal sulfur loading (75 wt.% and 9 mg/cm^2), the sulfur utilization is low compared to others, due to the thick sulfur coating on the parent CNTs (Figure 6.5B). However the "branch" cathode boasts impressive areal capacity and completive sulfur utilization as a direct result of optimal sulfur thickness (Figure 6.5B). This emphasizes that

one must pay heed to the quality of the sulfur coating to achieve high areal performance sulfur cathodes, and our work highlights that combining the bottom-up material design capable through CNT synthesis routes with vapor phase infiltration is a highly promising avenue to accomplish this goal.

6.4 Conclusion

Here we study the role of sulfur morphology to produce high areal capacity sulfur cathodes by combining a bottom-up growth strategy to produce hierarchical networks of thick CNT forests with programmable vapor phase sulfur infiltration. We demonstrate the function of a hierarchical CNT material to achieve this goal, where small diameter branched CNTs provide a high surface area for electrically addressable sulfur coating, and larger diameter parent CNTs provide conductive "highways" connecting the sulfur-infiltrated CNT branches to the collector. By utilizing the precise control of the vapor phase infiltration process, we demonstrate that programmed infiltration only into the smaller diameter CNTs is necessary to maintain high sulfur conversion and utilization, whereas routes that lead to thicker coatings on the larger diameter CNTs present charge transfer barriers and lowers sulfur utilization. Overall, this work overcomes the lack of sulfur coating control in the melt diffusion method and highlights that "quality over quantity" is of practical importance particularly in the design of thick electrodes with high areal capacity. We show the combination of bottom-up methods to pre-fabricate controlled carbon networks (e.g. CNT growth) combined with the controlled energetics

dictating capillary condensation in nanopores through vapor infiltration can unlock a route to high quality sulfur coatings over thick cathode architectures.

Chapter 7

A Sugar Derived Room Temperature Sodium Sulfur Battery with Long Term Cycling Stability

Adapted From: R. Carter, L. Oakes, A. Douglas, N. Muralidharan, A.P. Cohn, and C.L. Pint, "A sugar derived room temperature sodium sulfur battery with long term cycling stability," Nano Lett., 17, 1863-1869 (2017) *with permission from American Chemical Society*.

7.1 Introduction

The sodium beta battery was developed in the 1960's by Ford Motor Company under the promise that it could deliver the cost and performance metrics required for battery-powered electric vehicles.[212] This battery design involves a sodium anode, a sulfur cathode, a beta-alumina solid separator and operation at temperatures > 300ºC. The high temperature enables sodium wetting on the beta alumina, diffusion of sodium ions to the cathode, and the molten cathode to sustain a soluble media for sodium polysulfide species. Despite the loss of interest in electric vehicles in the mid-nineteenth century, the sodium-beta battery emerged as a staple low-cost battery system that remains commercially available today and routinely used for commercial load-leveling applications.[2] However, despite its excellent material cost/performance ratio,[4] the high operation temperature prohibits its practicality in applications that currently command the rechargeable battery market and operate at room temperature, leaving these systems only useful for niche applications.[14] Nonetheless, the capability to design a battery with the cost/performance

metrics of a sodium beta battery, but with stable room temperature operation could be disruptive to current battery powered technologies[4] and specifically provide a practical path toward stationary grid storage with lifetime energy cost below 1 ¢/kWh. Compared to battery markets for portable electronics or mobile systems where gravimetric performance and safety dictate feasibility over other metrics, batteries for residential or commercial stationary storage require low-cost, long lifetime, and good rate accessibility to yield lifetime cost-per-unit-energy of $< \sim 0.12$ ¢/kWh *after* coupling with an energy generation source, such as photovoltaic cells – requiring a battery cost < 0.01-0.02 ¢/kWh in (optimistic) current market conditions. Unlike current lithium-ion batteries, room-temperature sodium-sulfur batteries give promise for stationary units displaying all of these metrics and exhibiting energy density comparable to or better than current lithium-ion batteries.

In recent years, the protégé for room temperature sodium sulfur batteries, lithium-sulfur batteries, have emerged as an appealing replacement for current lithium-ion batteries boasting a 2-electron transfer per sulfur atom, delivering 6X the energy density of Li-ion, and overcoming cost and safety issues of conventional cobalt-containing cathodes. As significant research has addressed key issues such as polysulfide shuttling that limits cycling stability, continued challenges remain, including anode stability that must be addressed with consumable lithium nitrate additives,[82] and routes that can intersect conventional battery manufacturing facilities and enable high areal loadings.[12] Whereas bottlenecks remain to reach a battery with 500 Wh/kg energy density – a critical goal of Li-S battery technology, in this work we highlight that the rational design of a sodium-sulfur battery with a competitive energy density to Li-ion batteries can overcome current

bottlenecks challenging Li-S batteries, enabling a key platform for future grid scale stationary storage units where cost trumps energy density in market feasibility. The similar discharge mechanisms of the alkali metals involve incremental discharge from elemental sulfur (stored as S_8 molecules) through intermediate products (M_2S_8, M_2S_6, M_2S_4; M=Li or Na), which are soluble in the commonly used organic electrolytes, to the final products M_2S_2 and M_2S, which are insoluble.[10, 12, 14] Particular challenges with room temperature sodium sulfur batteries compared to lithium sulfur batteries are the greater volume expansion (260% for Na vs. 80% for Li),[14] low measured Coulombic efficiencies due to instability at both the anode and cathode,[10, 213-216] and poor understanding of soluble discharge products.[10] Additionally, whereas manufacturing costs must be minimized in stationary cells, functional electrode materials must involve cheap, if any, processing and from bulk forms of sodium, sulfur, and/or carbon.

One emerging strategy for mitigating soluble products in lithium-sulfur batteries is by microporous confinement, where all sulfur is stored in the system as molecules limited to the sizes S_{2-4}, where S_4 is the larges sulfur molecule permitted in the material interior, by controlling the size of pores in the host. Confinement efforts for lithium sulfur batteries were abandoned because the necessary micropore size (<1 nm) limits sulfur mass loadings to under 50 wt.%,[21-24, 75] and higher loadings (>70%) are necessary to reach appropriately high gravimetric energy density that dictates their use as advanced Li-ion carriers.[12] However, early sodium sulfur batteries without confinement (elemental S_8 cathodes) yield poor sulfur conversion[73-74, 213, 216-219] unless additional device elements including interlayers or dense solid electrolytes adding excessive mass, volume, and cost are employed.[214-215, 220-222] Whereas microporous confinement lowers the overall energy

density since higher voltage conversion of soluble products is excluded, effective implementation of the strategy can still deliver 2X the energy density of Li-ion and significant reliability is gained.[14] Initial confinement works have shown significantly improved sulfur conversion and cyclability[71, 76-77, 192, 223-225], but all suffer from low Coulombic efficiency due to an unstable anode-electrolyte interface.

In this work we realize this promising approach by demonstrating a microporous confinement cathode for a room temperature sodium sulfur battery based on processing store-bought table sugar and infiltrating sulfur into micropores using scalable isothermal vapor phase infiltration. The confinement strategy mitigates polysulfide shuttling at the cathode and is assembled with a glyme-based electrolyte, which provides a stable sodium-electrolyte interface[6] that overcomes low Coulombic efficiency. The stability of both electrodes delivers significantly enhanced Coulombic efficiency (>98%) over previous works on Na-S batteries (50-80%).[10, 14] We demonstrate a platform that exhibits exceptional durability over 1500 cycles while still delivering above 300 mAh/g_S at high rates of 1C.

7.2 Experimental Details

7.2.1 Preparation of Carbon Spheres

Table sugar (Whole Foods) was dissolved in nanopure(MP) water to form a 5% sucrose solution, which was placed in round bottom flask and sulfuric acid (Sigma) was added to a 5 M concentration. This solution was refluxed at 120°C for 10 h. The solution initially changes color from yellow to orange to red to brown to dark brown. The resulting blackish

suspension was centrifuged and washed with nanopure water until a pH of 7 indicated removal of the sulfuric acid. The material was then dried at100°C in air for 24h. The material was then pyrolized at 850°C in a tube furnace at low pressure under Ar flow of 200 sccms for 2 hours. The resulting black powder was then infiltrated with sulfur by assembling a vessel with the obtained powder (~1mg) in a stainless steel pan adjacent a pan containing an excess (~10mg) of sulfur powder (99.998% Sigma) inside a high pressure sealed vessel; we used a modified coin cell (CR 2032 MTI). This system was then placed inside a furnace heated to 175°C for 1 hour. By massing the powder before and after infiltration a loading of 35 wt.% sulfur was obtained.

8.2.2 Characterization

The material was prepared into electrodes by first making slurries of active material, carbon black (C45 MTI) and CMC binder (Aldrich) at a 80:10:10 ratio in NMP. This material was drop cast onto SS discs (MTI) and dried in under vacuum overnight. The electrodes were employed as cathodes in a CR 2032 stainless steel coin cell (MTI) with a sodium metal anode (Strem), 2400 Celgard separator wetted with 1M $NaPF_6$ (Strem), 0.25M $NaNO_3$ (Aldrich 99+%) in a TEGDME (99+% Acros). The coin cell and electrolyte were prepared in an argon glove box (MBraun) with <0.5 ppm O_2. Galvanostatic charge/discharge was carried out using an MTI 8 channel battery analyzer. Cyclic Voltamagrams were obtained using Nova Autolab. Scanning Electron Microscopy (Zeiss), Transmission Electron Microscopy (TEM) and Scanning Transmission Electron Microscopy Energy Dispersive X-Ray Spectroscopy (STEM EDS) (Osiris) were preformed, as well as Raman Spectroscopy (Renishaw). Ex-stiu Raman studies were carried out by coin cell first coin cell deconstruction followed by assembly of o-ring

sealed glass slides containing the fully discharged cathode. This material was then scrapped into TEGDME and drop cast onto a TEM grid in the glovebox. Air exposure was limited until loading into the microscope.

7.3 Results and Discussion

To realize a microporous sulfur-confining host, we processed table sugar into microporous carbon-sulfur composite materials. Here, as received sugar ($C_{12}H_{22}O_{11}$) was controllably dehydrated in a 5M solution of sulfuric acid at 120°C for 10 hours to leave behind only amorphous carbon (Figure 7.1A). This process controllably utilizes the violent exothermic reaction between pure sulfuric acid and sugar for higher precision at the nanoscale. The rinsed amorphous carbon precipitate was pyrolized under low pressure Ar flow for 2 hours at 850°C[226-227] leaving carbon spheres of ranging diameter (50-500 nm) seen in Figure 7.1B and 1C containing micropores (Figure 7.1D) with size of ~ 0.5 nm, agreeing well with other reports of sugar-derived microporous carbons.[22, 226-227] Some more visually apparent pores of size agreeing with FFT are indicated with double arrows in Figure 7.1D. Finally, the prepared carbon powder is infiltrated with sulfur by low temperature (175°C) isothermal vapor phase process[69] lasting 1 hour and resulting in 35 wt.% sulfur completely confined in the micropores of the carbon spheres. Whereas this is a lower mass ratio of sulfur than that required for high energy lithium-sulfur batteries, the cathode stability enabled by microporous confinement combined with a stable anode-electrolyte interface enables a moderate energy density and long-term stability necessary for a practical stationary battery system.

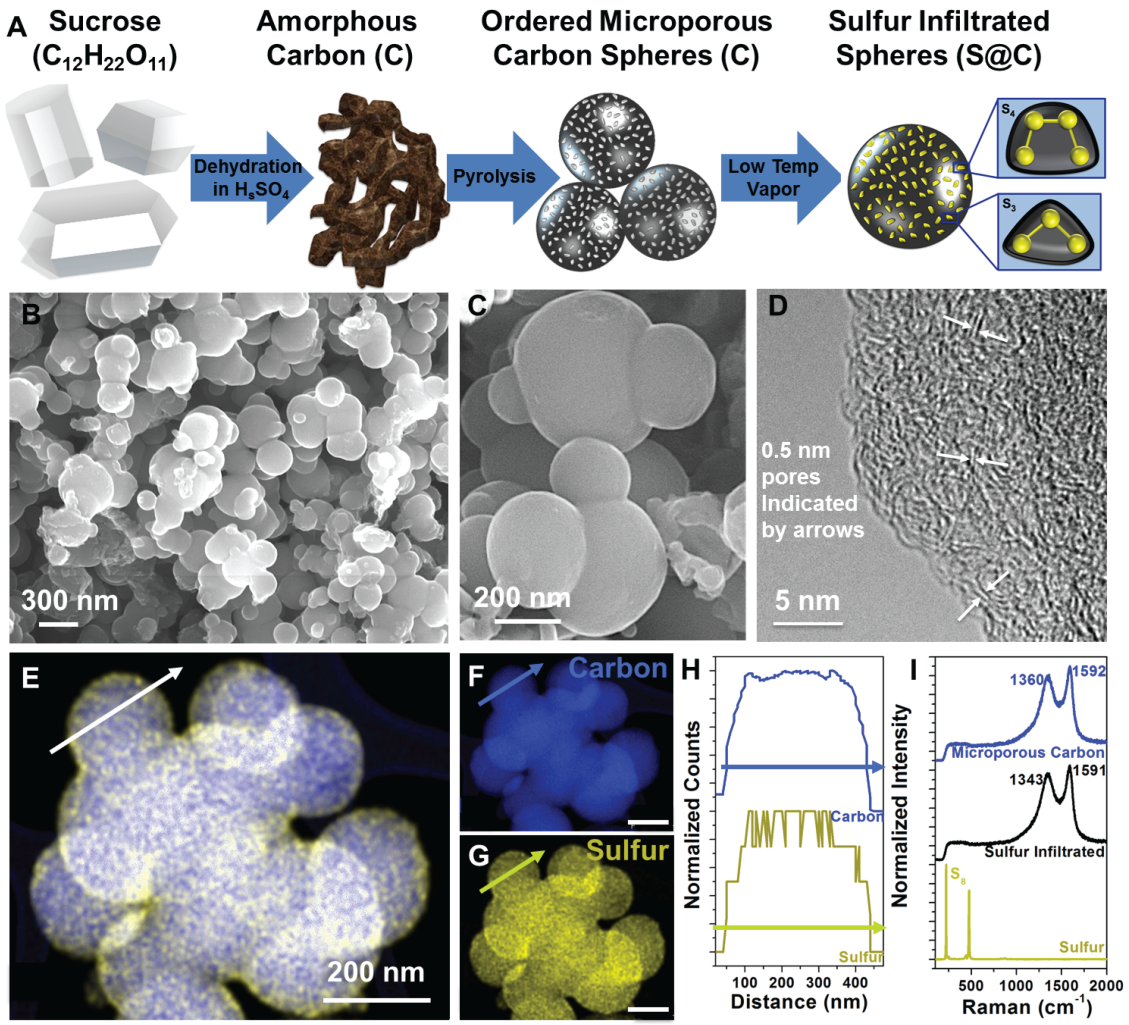

Figure 7.1. **A**. Schematic representation of the material processing steps of using sucrose (sugar) to produce microporous sodium sulfur battery cathodes. Scanning electron microscope (SEM) image of microporous carbon with spheres at **B** low and **C** higher magnification. **D.** TEM image showing morphology of micropores inside the carbon spheres, **E.** STEM EDS composite map with carbon (blue) and sulfur (yellow). **F-G** individual element maps and H. linescan across the diameter of a microporous carbon sphere infiltrated with sulfur**, I.** Raman spectroscopy of microporous carbon sulfur infiltrated spheres and as received sulfur powder.

This infiltration method is significantly more scalable and less expensive compared to other methods that traditionally employ long (>20 hr) melt techniques[22-23, 71] to ensure pore

infiltration or use high temperature (>300°C) loadings for depolymerization of sulfur vapor.[77, 223] Confinement in this electrode configuration is expected to promote only a transition from the largest S_4 molecules to Na_2S_2 and Na_2S sequentially, eliminating soluble products from the mechanism and preventing direct interaction between active sulfur and electrolyte.[10] This is because the pores are also too small to accommodate the solvent molecule (~ 0.7 nm in diameter).[228-229] In turn, the metal ion (only ~ 0.2 nm in diameter) must desolvate at the surface of the microporous host and transport independently to the sulfur, forming a quasi solid-state reaction at the cathode as opposed to the typical conversion battery configuration were ions transport through the electrolyte until reaching an active site before desolvating and readily converting.[22-23] Notably, whereas this technique specifically targets micropores due to the high free energy that drives capillary insertion of sulfur, higher loadings can be achieved by enhancing microporous volume or utilizing different strategies. Our previous work has achieved >80 wt.% loading in sulfur cathodes where the confinement mechanism isn't required.[69]

In order to verify uniform infiltration of sulfur, STEM EDS elemental mapping was utilized. By visual inspection of the composite map revealing spatial distribution of carbon and sulfur (Figure 7.1E), the signature of both elements are uniform across the material. The individual element maps of carbon in blue (Figure 7.1F) and sulfur in yellow (Figure 7.1G) show no differentiating features when in direct comparison and a uniform distribution of sulfur intensities (Figure 7.1G) across individual spheres, affirming the effectiveness of the isothermal vapor process in infiltrating the entirety of the spheres without build up at the surface. A line scan (Figure 7.1H) spanning the diameter of a sphere reveals a hill shaped response for both elements, indicative of the sphere geometry

with highest signal at the middle and no signal at the exterior on each extremity of the line. Carbon and sulfur are detected throughout the sphere with minimal variation in intensity, emphasizing the complete and uniform penetration of sulfur through the material.

Raman spectroscopy was used to compare as prepared microporous carbon to sulfur infiltrated carbon and verify absence of S_8 molecules (Figure 7.1I). With 532 nm laser excitation the microporous carbon powder reveals defective carbon with characteristic G (sp^2 hybridized), and D (sp^3 hybridized) peaks at 1360 cm^{-1} and 1592 cm^{-1} respectively, and an I_D/I_G ratio of 0.91. This response along with the TEM image of the microporous morphology (Figure 7.1D) provides evidence of microporous pore size with disordered, partially graphitized carbon present. After sulfur infiltration, the spectra is observed to red shift by 17 cm^{-1} in the D peak, indicating both that sulfur that is primarily stored in defect sites (sp^3 hybridized carbon) where the spacing is largest and that an intimate interaction between sulfur and carbon defects exists. Additionally, no characteristic S_8 peaks were detected in the infiltrated material, indicating the sulfur is stored as smaller molecules without crystalline order and fully contained in the carbon material.

Upon verification of uniform sulfur infiltration and ideal microporous structure the powder is slurry-cast into cathodes and assembled into coin cells with sodium metal anodes. As opposed to using traditional organic carbonate electrolytes,[10] coin cells were assembled using $NaPF_6$ salts dissolved in tetraglyme as electrolyte. Building on previous studies that emphasize sodium anode stability during the reversible plating reaction in glymes,[6] this electrolyte was chosen to overcome the unstable SEI formation on Na metal

anodes observed in carbonate-based electrolytes, which is critical to achieving good cycling performance. The discharge/charge behavior is first examined using cyclic voltammetry over the extended range of 0.5 V to 2.7 V beginning with discharge from OCV of ~1.7 V at scan rate of 50 μV/s (Figure 7.2A). Two peaks are detected on charge and discharge correlating to the two distinct transitions in the system to Na_2S_2 at ~1.7 V and Na_2S at ~0.9 V.[71] The second transition is prominent on the first discharge cycle and begins to match the intensity on first charge in subsequent cycles. These transitions are schematically illustrated on the voltammagram. An initial state and fully charged state of S_4 is depicted. However there a range of molecule sizes from S_2-S_4 depending on the slight variation of pore size and shape throughout the material. S_4 is the largest molecule present, as confirmed by the presence of a two-step transition below the voltage where high order polysulfides form and geometric agreement with previous theoretical studies.[71] The S_4 requires full transition through both peaks on cycling. Smaller molecules will iterate through the appropriate transitions within the curve. Galvanostatic charge discharge of the material was carried out at various rates over the voltage range of 0.8 V to 2.6 V with representative profiles shown in Figure 7.2B. On first discharge at the slow rate of 0.1 C (C = 1675 mA/g_S) the material reaches 91% of theoretical capacity and visual distinction between the two reaction plateaus, correlating to the peaks in Figure 7.2A, is present. Additionally, similar to the observation in CV measurements, the transition to Na_2S recedes during cycling. This could be attributed to poor volume expansion accommodation in the material due to the native confinement in microporous volumes.

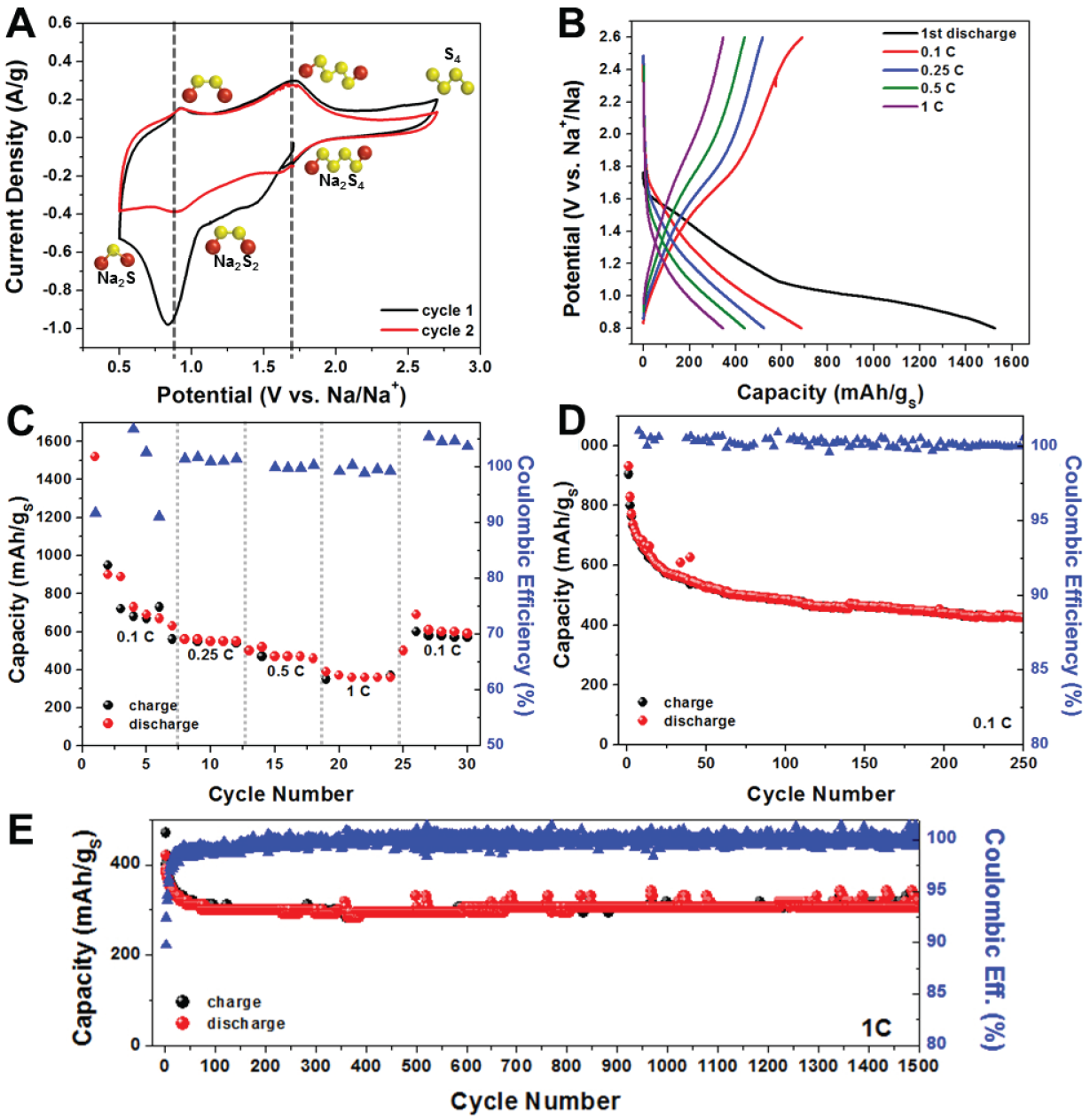

Figure 7.2- A. Cyclic voltammetry of sulfur cathode at 50 μV/s with sodium/sulfur interactions pictorially represented, **B** galvanostatic charge/discharge profiles at various charging rates, **C.** capacity and Coulombic efficiency with > 5 cycles at each rate, **D** 250 cycles at 0.1 C with discharge and charge capacity plotted at each cycle and coulombic efficiency plotted as blue triangles with axis at the right, and **E**. 1500 cycles at 1 C in same format as **D**.

Nonetheless, stable capacity and shapes of the CV and galvanostatic charge/discharge profiles suggest final discharge product of $Na_2S_{1.5}$ corresponding to ~160% expansion is sustained by the material and its sodium storage capacity far surpasses elemental sulfur cathodes limited to the discharge product Na_2S_3[10] or half the sodium stored in our system. This stable discharge product results and reversible capacity (700 mAh/g_S) and is capable of energy density of ~180 Wh/kg when considering entire electrode mass (sulfur, microporous carbon, binder, carbon black, and ideal sodium anode). This metric emphasizes the competitive nature of this approach in relation to state-of-the-art commercial batteries after implementing extremely simplistic manufacturing methods.

Additionally, impressive rate capability exists as verified by reversible capacity of 370mAh/g_S at high rates of 1C, which emphasizes over 50% retention of capacity at 10X the rate. Notably, at all rates the Coulombic efficiency remains >98% (Figure 7.2C), which is quite remarkable compared to the extremely low Coulombic efficiencies ranging from 50-80% with elemental sulfur cathodes.[10] We attribute the high Coulombic efficiency to stable SEI formation at the sodium metal-electrolyte interface due to the glyme electrolyte as well as the quasi-solid state nature of the reaction where sodium ions transport through the resilient carbon material and react without contact with the glyme at the cathode.

Durability tests at 0.1 C (Figure 7.2D) and 1 C (Figure 7.2E) rates were also carried out. At 0.1 C, a decay to ~60% capacity retention in the first 20 cycles is followed by stable behavior (~0.1% decay per cycle) for 230 subsequent cycles. The cathode tested at higher rates revealed similar behavior but after initial decay exhibited extremely stable capacity with 306 mAh/g_S delivered at cycle 1500. With respect to the entire mass of the

electrode, the cathode delivers 87 mAh/g after 1500 cycles at 100% depth of discharge (DOD), which is impressive mass specific performance especially with the moderate loading of 35 wt. % active sulfur. This is amplified based on the premise that this material template is based on sugar, sulfur, and sodium and shows proof of concept for this approach to produce viable grid scale battery cathodes. In all cases, after the initial decay of reversible capacity, the Coulombic efficiency remained >98%.

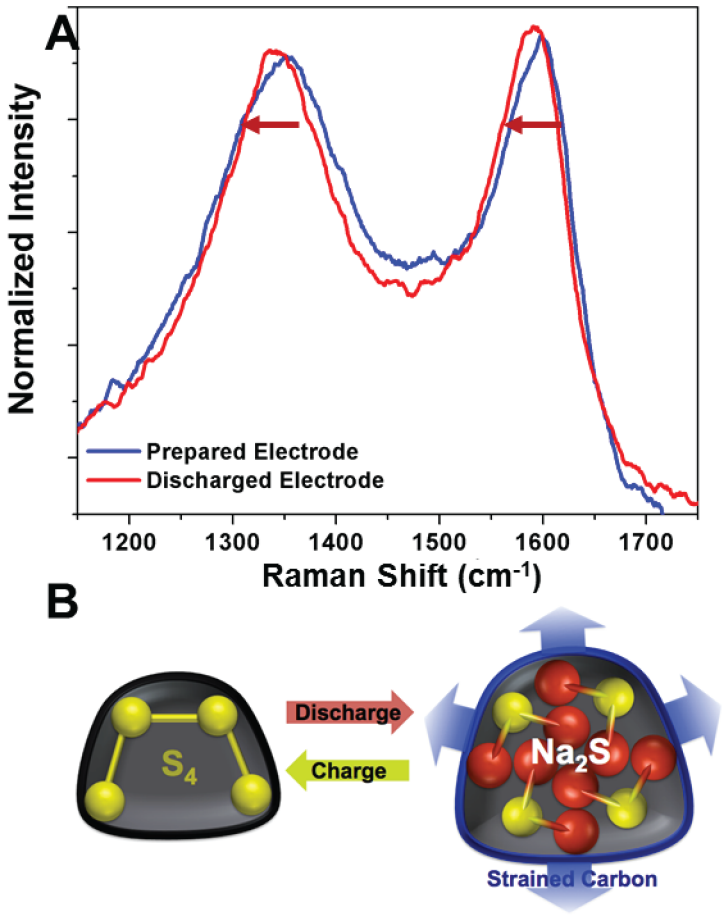

Figure 7.3- A. Raman spectroscopy of an as-prepared slurry-cast electrode and fully discharged cathode **B.** schematic representation of discharge mechanism inside a micropore which results in a strained carbon host.

In order to gain further insight into the behavior of the material during discharge, a cathode was cycled 20 times to reach the stable regime and then fully discharged cathode and examined using Raman spectroscopy and STEM EDS mapping. The electrode was retrieved from a discharged coin cell, sealed in an airtight window, and compared to an as-prepared electrode (Figure 7.3A). The discharged material revealed significant redshift of both the D and G carbon peaks of 12 and 14 cm^{-1} respectively (Figure 7.3A). The final red shift of the D peak is >25 wavenumbers with combination of sulfur infiltration seen in Figure 7.1I and sodiation inside the carbon material (Figure 7.3A). The red shift of both peaks indicates strong tensile stress in the carbon as a result of the volume change as each sulfur attempts to store 2 sodium ions, theoretically leading to a 260% volume expansion (Figure 7.2B). In order to support the observation of tensile force of the material as a result of sodium induced volume expansion, STEM EDS was used to verify uniform confinement of sodium throughout the material. The composite map in Figure 7.4A shows the distribution of sodium, sulfur, and carbon in a cluster of discharged spheres. Line scans taken across the largest sphere shows sodium distributed throughout, with a response revealing the combined presence of the electrolyte (fluoride and phosphorous) and sulfur, verifying its presence and reactivity with sulfur. The individual element maps with carbon mapped blue (Figure 7.4C), sulfur yellow (Figure 7.4D) and sodium red (Figure 7.4E) further emphasize the uniform loading of sulfur throughout the carbon and the complete penetration of sodium on the interior of the microporous carbon with some apparent dried electrolyte across the surface. This *ex-situ* characterization helps to verify the ability of sodium to fully access the microporous spheres (TEM), as well as significant

tensile stress in the system as the material accommodates sodium ions on discharge (Raman spectroscopy).

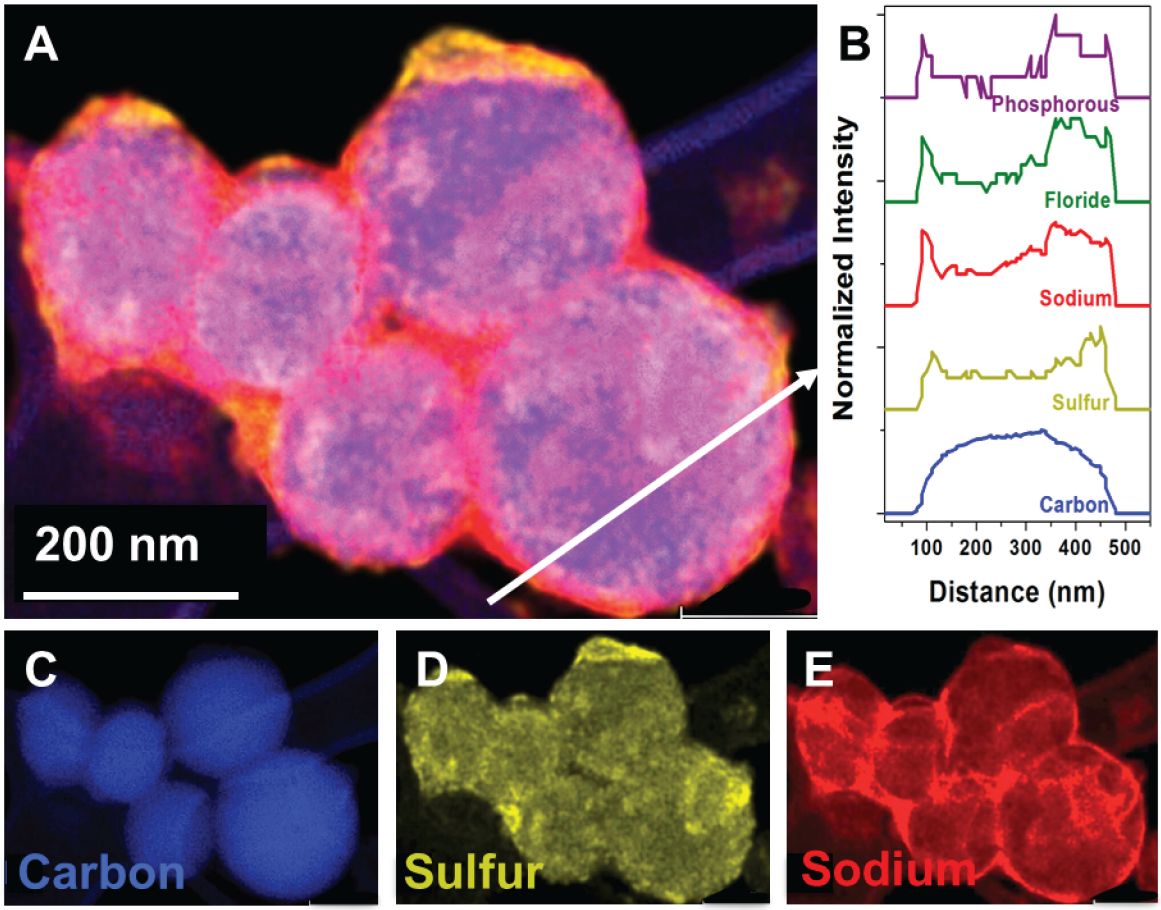

Figure 7.4- A. STEM EDS composite map of fully discharged microporous carbon spheres with carbon (blue), sulfur (yellow), and sodium (red), **B.** linescan across the diameter of a microporous sphere with phosphorous (purple) and flouride (green) signatures arising from the electrolyte salt and carbon, sulfur and sodium intensity plotted, **C-E** individual element maps for carbon, sulfur, and sodium.

7.4 Conclusion

Overall, our work demonstrates the capability to produce a room temperature sodium sulfur battery based on combined electrode components of sodium, sulfur, and processed table sugar. Compared to other approaches, the high Coulombic efficiency, microporous confinement of discharge products, and electrolyte that leads to a stable SEI on the sodium anode gives rise to high performance with stable cycling over 1500 cycles at high rates of 1C where a capacity > 300 mAh/g_S is maintained compared to reversible capacities at slow rates of 0.1 C where > 700 mAh/g_S is measured. This work presents an attractive platform for future battery design, both for a cheap alternative to lithium-ion batteries where the competitive cathode gravimetric capacity in sugar derived sulfur cathodes rivals that of cobalt-containing cathodes in lithium-ion batteries, and a practical stationary grid storage system where excellent rate performance, cyclability, and simplicity of materials leads to promise for lifetime cost per kWh that can be significantly lower than conventional power generation.

Chapter 8

Conclusions and Future Outlook

8.1 Conclusions

Herein I have demonstrated unique material design strategies and a significantly improved composite processing technique to enable high performance sulfur conversion batteries. Perhaps the most lauded success of this dissertation was the realization of a simple rapid isothermal vapor processing technique, which allows sulfur composite processing without destruction of nanoengineered electrode materials. This process enabled demonstration of two unique carbon nanotube based lithium sulfur battery cathodes and one of the first highly stable, low-cost sodium sulfur battery cathodes operating at ambient temperature.

The early experiments in this dissertation (Chapter 2) present a porous silicon templating strategy, used to fabricate mesoporous carbon material tested as sulfur host in a lithium sulfur battery. The solubility of polysulfides produced during battery operation inherently causes host-less sulfur cathodes to fail rapidly, but this high aspect ratio interconnected carbon host effectively confines the solubilized species to deliver impressive retention over cycling (~ 0.2% decay/cyle of 250 cycles). The confinement is mostly attributed to the material's structure but FTIR characterization also reveals oxygen functional groups at the surface of the porous carbon, as a result of the high pH material processing. Previous works have shown that oxygen groups of this type enable

electrostatic binding with the highly polar lithium polysulfides to provide anchoring of the material at the surface, preventing migration out of the host. Although modulation of the surface functionalization is not enabled in this system, the anchoring behavior is a promising technique for preventing polysulfide migration in Li-S cells.

Ultimately, the performance of the porous silicon templated mesoporous carbon based Li-S cathode is challenged by the conventional composite processing technique, melt infiltration. The use of bulk sulfur liquid to load nanoscale features with sulfur, results in poor uniformity and compromise of the host's conductivity. The shortcomings of the conventional composite processing technique motivated development of extremely simple, rapid (<1 hr), low temperature (175°C), isothermal vapor infiltration technique capable of completely disrupting the accepted method in the field with highly improved characteristics. This process allows nondestructive sulfur processing of pre-formed host materials. Additionally, as described and characterized in chapter 4, the improved loading technique not only allows significant performance improvement of simplistic carbon host materials but also demonstrates ultra-high mass loadings (>80 wt.% S) and dramatically decreases process time and energy requirement (60X throughput at equivalent temperatures), when directly compared with melt infiltration.

With realization of improved composite processing, allowing nondestructive sulfur loading into host materials, this work utilized this loading technique to demonstrate one of the first effective uses of carbon nanotubes for Li-S cathode. Although, CNTs were proposed as the most promising candidates for high mass loading sulfur cathodes, as a result of their high surface area, low density, mechanical strength, and high conductivity, melt infiltration compromises the electrical interconnection of CNT hosts. Since the

innovative vapor infiltration process presented here preserves electrical conductivity of the host, Chapter 2 utilizes electrophoretic deposition to rapidly and cleanly assemble highly electrically interconnected CNT electrodes on various current collectors. These electrodes, ideal candidates for sulfur hosts (chapter 5 and 6) also demonstrate high performance as pure carbon electrodes of various types (supercpacitor, Li-ion anode and Li-air cathode).

With demonstrated ability to interior confine sulfur in CNTs using isothermal vapor capillary filling, Chapter 5 further modifies the CNT electrode building block to obtain ultra-stable cycling behavior (~0.06% decay/cycle over 450 cycles). An ultra-thin, exterior coating of polysulfide anchoring V_2O_5 is applied to the CNTs using atomic layer deposition, so that solubilized species exiting the ends of the CNTs are reactivated by electrostatic binding at the anchoring layer. The high degree of control provided by ALD, reveals optimal binding layer thickness with 75 deposition cycles (~ 3 nm of V_2O_5), where thicker layers inhibit charge transfer to the exterior anchored materials and thinner layers saturate with polysulfides early in device cycling.

With demonstration of a high mass specific performance Li-S battery cathode using the ideal carbon nanotube building block material, Chapter 6 assembles CNTs into hierarchical scaffolds and vapor loads them with sulfur to demonstrate a packaging level sulfur loading while maintaining high mass specific performance. The tree-like scaffolds are developed by two-step floating catalyst growth process, first producing vertical CNT arrays (~ 50 nm diameter) and second producing single walled CNTs (<1nm diameter) from the sidewalls of the first growth. Using isothermal vapor infiltration, the small diameter CNTs are selectively infiltrated, since less vapor accumulation is required at the small diameter CNTs in comparison to the larger parent CNTs. This size dependent

loading allows complete infiltration of the small diameter CNTs without influence to the mechanical rigidity and electrical interconnection of the larger CNTs. This cathode, delivering areal and mass specific performance greater than the conventional Li-ion battery, validates the CNT as a promising host material to enable commercially viable high energy density Li-S cathodes with packaging level sulfur loadings.

With successful demonstration of a high performance CNT based Li-S batteries cathodes using isothermal sulfur vapor loading, Chapter 7 utilizes the infiltration technique to enable one of the first low-cost, high stability room temperature sodium sulfur cathodes. This work develops sucrose derived mircoporous carbon nanospheres isothermally loaded with short chain sulfur. These spherical structures, ~ 200 nm in diameter, are filled throughout with ~ 0.5nm pores and the low temperature (175°C) isothermal vapor is capable of rapidly (1 hr), fully penetrating the spheres to load the material with 35 wt.% sulfur. This material delivers total mass capacity approaching that of the conventional Li-ion battery and exceptional cyclability (only ~0.02% decay/cycle over 1500 cycles), an impressive result for this system, inflated in value by the exceptional low cost of materials.

The culmination of this work brightens the future of sulfur conversion batteries by (1) enabling a highly improved sulfur loading technique that is less energy intensive and nondestructive to host materials, (2) demonstrating the tunable functionality of the carbon nanotube nanoscale building block for optimized sulfur host behavior in Li-S cells and (3) giving promise for realization of a low-cost, highly stable room temperature Na-S battery.

8.2 Future Outlook

Significant future work is motivated by the results presented here. For lithium sulfur batteries the low temperature vapor infiltration process should be further explored in scaffolds designed for ultra-high areal loadings. Carbon nanotube sponges are a likely direction promising success, since interior filling provides uncompromised electrical interconnection on any length scale. Further, in addition to insufficient sulfur loadings for package scale performance, the high electrolyte volume to sulfur mass ratio (v:m), required to accommodate solubilized species in the Li-S system, hinders commercial viability. The use of the microporous confinement strategy, where the conversion reaction is isolated from the electrolyte, can mitigate this challenge. Although abandoned due to low sulfur loadings, it is worth further attention from the field to enable lower density microporous materials, which can subsequently isothermally infiltrated at low cost (rapid and low temperature). Further, these efforts to improve sulfur mass loadings into microporous materials can prove highly valuable for advancement of the room temperature sodium sulfur cell.

With many questions still remaining in the sodium sulfur system, a logical and highly valuable next direction for this chemistry is to utilize *in-situ* characterization techniques to detect and characterize the intermediate products of the system. The distinct absorbance spectra of high order solubilized sodium sulfide solutions gives promise for detection of these solubilized species during external biasing of a modified Na-S cell using UV-vis spectroscopy. Further vibrational spectroscopy like FTIR and Raman can be utilized to examine the active species, intermediate products, and host materials *in-*

operando. I have obtained some initial results in this area, detecting fluctuating intensity of sodium polysulfide signatures with external biasing, giving significant promise to the success of this characterization strategy. Here, if sodium polysulfide products can be isolated with Raman, quantified with UV-vis and correlated to battery discharge features, cathode design can be significantly more educated and the success of the chemistry will be expedited.

Finally, the simplistic mechanism of isothermal sulfur vapor loading leaves the question, can this process be utilized for the fabrication of other material composites? The vapor process is successful in part because of the high vapor pressure of sulfur, tempting experimentation of this process with other low melting point, high vapor pressure materials including alkali metals. The ability to easily manipulate alkali metals in host materials is highly desired for development of high performance metallic anodes. Further this loading mechanism could be valuable for biological applications, where interior confinement is valued. Overall the vapor processing and scalable nanomaterial manipulation demonstrated here for high performance sulfur conversion chemistries, motivates future work of ranging scope and application.

Appendix A

Battery Characterization

The primary battery testing technique used to characterize batteries is galvanostatic charge discharge, where constant current is delivered and drawn for charge and discharge respectively while potential across the cell is measured, over a defined voltage range. Potential across the cell, proportional to the electrochemical potential difference between the electrodes, is increased with charging and decreased with discharging. A region of "flat" or minimally changing voltage over time, typically referred to as a voltage plateau, indicates an electrochemical reaction. Here charges are transferring in the cell to balance external electrical current but the cell potential is unchanged. At the competition of the reaction, cell voltage drops in a linear manner, proportional to the cell resistance (V=IR), until the cell potential approaches a voltage desirable for a new electrochemical reaction to initiate.

This testing allows determination of electrode capacity, cell energy and columbic efficiency. Typically standardized charging currents (C rates) are used for this testing based on the active material theoretical capacity, which is calculated according to equation A.1 where n is the number of electrons transferred in the cell reaction, F is faraday's constant, and M is the active material molar mass.

$$Q = \frac{nF}{M} \quad \text{A.1}$$

The theoretical capacity, typically expressed in units of mAh/g, allows for calculation of currents predicted to deliver specific cycle lengths. Some commonly

assessed charge durations are 10 hr, 1hr, and 0.5 hr, corresponding to 0.1C, 1C and 0.5C, respectively. At these prescribed currents the actual capacity of the cells are calculated using equation A.2 where I is the applied current, t is time of discharge and m is the mass of active material.

$$Q = \frac{It}{m} \quad \text{A.2}$$

This metric also typically expressed in mAh/g can be converted to areal capacity by normalizing to the surface area of the current collector as opposed to the active mass. Further if the capacity of the discharge is divided by the capacity of the charge (equation A.3), the reversibility of the cell reaction can be assessed with a metric referred to as coulombic efficiency.

$$CE = \frac{Q_{discharge}}{Q_{charge}} \text{ A.3}$$

Finally by integrating the discharge curve the cell energy density can be calculated, as shown in equation A. 4.

$$E = \frac{I}{m}\int_0^t V(t)dt \quad \text{A.4}$$

This metric is typically epressed in units of Wh/kg. The energy of the cell can also be normalized to volume for assessment of the cell's volumetric performance (Wh/L). Theoretical energy density assumes constant voltage at the average potential of the desired electrochemical reaction.

Capacity and energy of the cell is typically assessed over any number of iterated galvaonstatic charge discharge cycles to determine performance retention over cycling.

Additional electrochemical characterization techniques like cyclic voltammetry and electrochemical impedance spectroscopy are also vital to cell characterization. Cyclic voltammetry potentiostatically biases cells incrementally at a specific scan rate (V/s) over

a desired range of voltages and detects current flow, to assess reaction voltages and kinetics. Electrochemical impedance applies AC voltage at a range of frequencies and detects magnitude and phase shift of AC current for determination of real and imaginary impedance elements, arising at various interfaces in cell at different time constants.

Appendix B

Reference List for Table 4.1

1. Lee, J. S.; Kim, W.; Jang, J.; Manthiram, A., Sulfur-Embedded Activated Multichannel Carbon Nanofiber Composites for Long-Life, High-Rate Lithium–Sulfur Batteries. *Adv. Energy Mater.* **2017,** *7*, 1601943.
2. Zhou, G.; Tian, H.; Jin, Y.; Tao, X.; Liu, B.; Zhang, R.; Seh, Z. W.; Zhou, D.; Liu, Y.; Sun, J., et al., Catalytic oxidation of Li2S on the surface of metal sulfides for Li–S batteries. *PNAS* **2017,** *114*, 840-845.
3. Song, J. X.; Yu, Z. X.; Gordin, M. L.; Wang, D. H., Advanced Sulfur Cathode Enabled by Highly Crumpled Nitrogen-Doped Graphene Sheets for High-Energy-Density Lithium-Sulfur Batteries. *Nano Lett.* **2016,** *16*, 864-870.
4. Wang, X. L.; Li, G.; Li, J. D.; Zhang, Y. N.; Wook, A.; Yu, A. P.; Chen, Z. W., Structural and chemical synergistic encapsulation of polysulfides enables ultralong-life lithium-sulfur batteries. *Energ. Environ. Sci.* **2016,** *9*, 2533-2538.
5. Cui, Y.; Wu, M.; Scott, C.; Xie, J.; Fu, Y., A binder-free sulfur/carbon composite electrode prepared by a sulfur sublimation method for Li-S batteries. *RSC Advances* **2016,** *6*, 52642-52645.
6. Li, G.; Sun, J.; Hou, W.; Jiang, S.; Huang, Y.; Geng, J., Three-dimensional porous carbon composites containing high sulfur nanoparticle content for high-performance lithium-sulfur batteries. *Nat. Commun.* **2016,** *7*, 10601.
7. Tao, X.; Wang, J.; Liu, C.; Wang, H.; Yao, H.; Zheng, G.; Seh, Z. W.; Cai, Q.; Li, W.; Zhou, G., Balancing surface adsorption and diffusion of lithium-polysulfides on nonconductive oxides for lithium-sulfur battery design. *Nat. Commun.* **2016,** *7*, 11203.
8. Yu, M.; Ma, J.; Song, H.; Wang, A.; Tian, F.; Wang, Y.; Qiu, H.; Wang, R., Atomic layer deposited TiO 2 on a nitrogen-doped graphene/sulfur electrode for high performance lithium–sulfur batteries. *Energ. Environ. Sci.* **2016,** *9*, 1495-1503.
9. Li, R.; Zhang, M.; Li, Y.; Chen, J.; Yao, B.; Yu, M.; Shi, G., Mildly reduced less defective graphene oxide/sulfur/carbon nanotube composite films for high-performance lithium–sulfur batteries. *Physical Chemistry Chemical Physics* **2016,** *18*, 11104-11110.
10. Jin, F.; Xiao, S.; Lu, L.; Wang, Y., Efficient Activation of High-Loading Sulfur by Small CNTs Confined Inside a Large CNT for High-Capacity and High-Rate Lithium–Sulfur Batteries. *Nano Lett.* **2015,** *16*, 440-447.
11. Liang, X.; Hart, C.; Pang, Q.; Garsuch, A.; Weiss, T.; Nazar, L. F., A highly efficient polysulfide mediator for lithium–sulfur batteries. *Nat. Commun.* **2015,** *6*, 5682.
12. Sun, L.; Kong, W.; Jiang, Y.; Wu, H.; Jiang, K.; Wang, J.; Fan, S., Super-aligned carbon nanotube/graphene hybrid materials as a framework for sulfur cathodes in high performance lithium sulfur batteries. *J. Mater. Chem A* **2015,** *3*, 5305-5312.
13. Du, W.-C.; Yin, Y.-X.; Zeng, X.-X.; Shi, J.-L.; Zhang, S.-F.; Wan, L.-J.; Guo, Y.-G., Wet Chemistry Synthesis of Multidimensional Nanocarbon–Sulfur Hybrid Materials

with Ultrahigh Sulfur Loading for Lithium–Sulfur Batteries. *ACS Appl. Mater. Interfaces* **2015,** *8*, 3584-3590.
14. Yuan, G.; Wang, G.; Wang, H.; Bai, J., A novel three-dimensional sulfur/graphene/carbon nanotube composite prepared by a hydrothermal co-assembling route as binder-free cathode for lithium–sulfur batteries. *J. Nanopart. Res.* **2015,** *17*, 1-11.
15. Kim, J. W.; Ocon, J. D.; Kim, H. S.; Lee, J., Improvement of Energy Capacity with Vitamin C Treated Dual-Layered Graphene–Sulfur Cathodes in Lithium–Sulfur Batteries. *ChemSusChem* **2015,** *8*, 2883-2891.
16. Sun, L.; Wang, D.; Luo, Y.; Wang, K.; Kong, W.; Wu, Y.; Zhang, L.; Jiang, K.; Li, Q.; Zhang, Y., Sulfur Embedded in a Mesoporous Carbon Nanotube Network as a Binder-Free Electrode for High-Performance Lithium–Sulfur Batteries. *ACS nano* **2015,** *10*, 1300-1308.
17. Strubel, P.; Thieme, S.; Biemelt, T.; Helmer, A.; Oschatz, M.; Brückner, J.; Althues, H.; Kaskel, S., ZnO Hard Templating for Synthesis of Hierarchical Porous Carbons with Tailored Porosity and High Performance in Lithium-Sulfur Battery. *Adv. Funct. Mater.* **2015,** *25*, 287-297.
18. Zhou, G.; Zhao, Y.; Manthiram, A., Dual-Confined Flexible Sulfur Cathodes Encapsulated in Nitrogen-Doped Double-Shelled Hollow Carbon Spheres and Wrapped with Graphene for Li–S Batteries. *Adv. Energy Mater.* **2015,** *5*, 1402263.
19. Xi, K.; Chen, B.; Li, H.; Xie, R.; Gao, C.; Zhang, C.; Kumar, R. V.; Robertson, J., Soluble polysulphide sorption using carbon nanotube forest for enhancing cycle performance in a lithium–sulphur battery. *Nano Energy* **2015,** *12*, 538-546.
20. Qu, Y.; Zhang, Z.; Zhang, X.; Ren, G.; Lai, Y.; Liu, Y.; Li, J., Highly ordered nitrogen-rich mesoporous carbon derived from biomass waste for high-performance lithium–sulfur batteries. *Carbon* **2015,** *84*, 399-408.
21. Xu, C.; Wu, Y.; Zhao, X.; Wang, X.; Du, G.; Zhang, J.; Tu, J., Sulfur/three-dimensional graphene composite for high performance lithium–sulfur batteries. *J. Power Sources* **2015,** *275*, 22-25.
22. Chen, Y.; Lu, S.; Wu, X.; Liu, J., Flexible Carbon Nanotube–Graphene/Sulfur Composite Film: Free-Standing Cathode for High-Performance Lithium/Sulfur Batteries. *J. Phys. Chem. C* **2015,** *119*, 10288-10294.
23. Guo, J.; Zhang, J.; Jiang, F.; Zhao, S.; Su, Q.; Du, G., Microporous carbon nanosheets derived from corncobs for lithium–sulfur batteries. *Electrochim. Acta* **2015,** *176*, 853-860.
24. Liu, S.; Xie, K.; Chen, Z.; Li, Y.; Hong, X.; Xu, J.; Zhou, L.; Yuan, J.; Zheng, C., A 3D nanostructure of graphene interconnected with hollow carbon spheres for high performance lithium–sulfur batteries. *J. Mater. Chem A* **2015,** *3*, 11395-11402.
25. Wang, C.; Wang, X.; Wang, Y.; Chen, J.; Zhou, H.; Huang, Y., Macroporous free-standing nano-sulfur/reduced graphene oxide paper as stable cathode for lithium-sulfur battery. *Nano Energy* **2015,** *11*, 678-686.
26. Fu, K.; Li, Y.; Dirican, M.; Chen, C.; Lu, Y.; Zhu, J.; Li, Y.; Cao, L.; Bradford, P. D.; Zhang, X., Sulfur gradient-distributed CNF composite: a self-inhibiting cathode for binder-free lithium–sulfur batteries. *Chem. Commun.* **2014,** *50*, 10277-10280.
27. Xi, K.; Kidambi, P. R.; Chen, R.; Gao, C.; Peng, X.; Ducati, C.; Hofmann, S.; Kumar, R. V., Binder free three-dimensional sulphur/few-layer graphene foam cathode

with enhanced high-rate capability for rechargeable lithium sulphur batteries. *Nanoscale* **2014,** *6*, 5746-5753.
28. Cheng, X.-B.; Huang, J.-Q.; Zhang, Q.; Peng, H.-J.; Zhao, M.-Q.; Wei, F., Aligned carbon nanotube/sulfur composite cathodes with high sulfur content for lithium–sulfur batteries. *Nano Energy* **2014,** *4*, 65-72.
29. Yang, X.; Zhang, L.; Zhang, F.; Huang, Y.; Chen, Y., Sulfur-infiltrated graphene-based layered porous carbon cathodes for high-performance lithium–sulfur batteries. *ACS nano* **2014,** *8*, 5208-5215.
30. Zhao, C.; Liu, L.; Zhao, H.; Krall, A.; Wen, Z.; Chen, J.; Hurley, P.; Jiang, J.; Li, Y., Sulfur-infiltrated porous carbon microspheres with controllable multi-modal pore size distribution for high energy lithium–sulfur batteries. *Nanoscale* **2014,** *6*, 882-888.
31. Jung, D. S.; Hwang, T. H.; Lee, J. H.; Koo, H. Y.; Shakoor, R. A.; Kahraman, R.; Jo, Y. N.; Park, M.-S.; Choi, J. W., Hierarchical porous carbon by ultrasonic spray pyrolysis yields stable cycling in lithium–sulfur battery. *Nano Lett.* **2014,** *14*, 4418-4425.

REFERENCES

1. Armand, M.; Tarascon, J. M., Building better batteries. *Nature* **2008,** *451*, 652-657.
2. Dunn, B.; Kamath, H.; Tarascon, J. M., Electrical Energy Storage for the Grid: A Battery of Choices. *Science* **2011,** *334*, 928-935.
3. Bruce, P. G.; Freunberger, S. A.; Hardwick, L. J.; Tarascon, J. M., Li-O-2 and Li-S batteries with high energy storage. *Nat Mater* **2012,** *11*, 19-29.
4. Larcher, D.; Tarascon, J. M., Towards greener and more sustainable batteries for electrical energy storage. *Nat Chem* **2015,** *7*, 19-29.
5. Scrosati, B., Nanomaterials - Paper powers battery breakthrough. *Nat Nanotechnol* **2007,** *2*, 598-599.
6. Seh, Z. W.; Sun, J.; Sun, Y. M.; Cui, Y., A Highly Reversible Room-Temperature Sodium Metal Anode. *Acs Central Sci* **2015,** *1*, 449-455.
7. McCloskey, B. D., Attainable Gravimetric and Volumetric Energy Density of Li-S and Li Ion Battery Cells with Solid Separator-Protected Li Metal Anodes. *J Phys Chem Lett* **2015,** *6*, 4581-4588.
8. Etacheri, V.; Marom, R.; Elazari, R.; Salitra, G.; Aurbach, D., Challenges in the development of advanced Li-ion batteries: a review. *Energ Environ Sci* **2011,** *4*, 3243-3262.
9. Wood, D. L.; Li, J. L.; Daniel, C., Prospects for reducing the processing cost of lithium ion batteries. *J Power Sources* **2015,** *275*, 234-242.
10. Adelhelm, P.; Hartmann, P.; Bender, C. L.; Busche, M.; Eufinger, C.; Janek, J., From lithium to sodium: cell chemistry of room temperature sodium-air and sodium-sulfur batteries. *Beilstein J Nanotech* **2015,** *6*, 1016-1055.
11. Van Noorden, R., Sulphur back in vogue for batteries. *Nature* **2013,** *498*, 416-417.
12. Seh, Z. W.; Sun, Y. M.; Zhang, Q. F.; Cui, Y., Designing high-energy lithium-sulfur batteries. *Chem Soc Rev* **2016,** *45*, 5605-5634.
13. Rosenman, A.; Markevich, E.; Salitra, G.; Aurbach, D.; Garsuch, A.; Chesneau, F. F., Review on Li-Sulfur Battery Systems: an Integral Perspective. *Adv Energy Mater* **2015,** *5*, 1500212.
14. Manthiram, A.; Yu, X. W., Ambient Temperature Sodium-Sulfur Batteries. *Small* **2015,** *11*, 2108-2114.
15. Manthiram, A.; Fu, Y. Z.; Su, Y. S., Challenges and Prospects of Lithium-Sulfur Batteries. *Accounts Chem Res* **2013,** *46*, 1125-1134.
16. Su, Y. S.; Fu, Y. Z.; Cochell, T.; Manthiram, A., A strategic approach to recharging lithium-sulphur batteries for long cycle life. *Nat Commun* **2013,** *4*, 3985.
17. Borchardt, L.; Oschatz, M.; Kaskel, S., Carbon Materials for Lithium Sulfur Batteries—Ten Critical Questions. *Chem. Eur. J.* **2016,** *22*, 7324-7351.
18. Hagen, M.; Hanselmann, D.; Ahlbrecht, K.; Maça, R.; Gerber, D.; Tübke, J., Lithium–Sulfur Cells: The Gap between the State-of-the-Art and the Requirements for High Energy Battery Cells. *Adv Energy Mater* **2015,** *5*, 1401986.
19. Yao, H. B.; Yan, K.; Li, W. Y.; Zheng, G. Y.; Kong, D. S.; Seh, Z. W.; Narasimhan, V. K.; Liang, Z.; Cui, Y., Improved lithium-sulfur batteries with a

conductive coating on the separator to prevent the accumulation of inactive S-related species at the cathode-separator interface. *Energ Environ Sci* **2014,** *7*, 3381-3390.
20. Singhal, R.; Chung, S. H.; Manthiram, A.; Kalra, V., A free-standing carbon nanofiber interlayer for high-performance lithium-sulfur batteries. *J Mater Chem A* **2015,** *3*, 4530-4538.
21. Xu, Y. H.; Wen, Y.; Zhu, Y. J.; Gaskell, K.; Cychosz, K. A.; Eichhorn, B.; Xu, K.; Wang, C. S., Confined Sulfur in Microporous Carbon Renders Superior Cycling Stability in Li/S Batteries. *Adv Funct Mater* **2015,** *25*, 4312-4320.
22. Zhang, B.; Qin, X.; Li, G. R.; Gao, X. P., Enhancement of long stability of sulfur cathode by encapsulating sulfur into micropores of carbon spheres. *Energ Environ Sci* **2010,** *3*, 1531-1537.
23. Xin, S.; Gu, L.; Zhao, N. H.; Yin, Y. X.; Zhou, L. J.; Guo, Y. G.; Wan, L. J., Smaller Sulfur Molecules Promise Better Lithium-Sulfur Batteries. *J Am Chem Soc* **2012,** *134*, 18510-18513.
24. Helen, M.; Reddy, M. A.; Diemant, T.; Golla-Schindler, U.; Behm, R. J.; Kaiser, U.; Fichtner, M., Single step transformation of sulphur to Li2S2/Li2S in Li-S batteries. *Sci Rep-Uk* **2015,** *5*, 12146.
25. Xu, G. L.; Xu, Y. F.; Fang, J. C.; Peng, X. X.; Fu, F.; Huang, L.; Li, J. T.; Sun, S. G., Porous Graphitic Carbon Loading Ultra High Sulfur as High-Performance Cathode of Rechargeable Lithium-Sulfur Batteries. *Acs Appl Mater Inter* **2013,** *5*, 10782-10793.
26. Xu, G. Y.; Ding, B.; Nie, P.; Shen, L. F.; Dou, H.; Zhang, X. G., Hierarchically Porous Carbon Encapsulating Sulfur as a Superior Cathode Material for High Performance Lithium-Sulfur Batteries. *Acs Appl Mater Inter* **2014,** *6*, 194-199.
27. Hoffmann, C.; Thieme, S.; Bruckner, J.; Oschatz, M.; Biemelt, T.; Mondin, G.; Althues, H.; Kaskel, S., Nanocasting Hierarchical Carbide-Derived Carbons in Nanostructured Opal Assemblies for High-Performance Cathodes in Lithium-Sulfur Batteries. *Acs Nano* **2014,** *8*, 12130-12140.
28. Peng, H. J.; Liang, J. Y.; Zhu, L.; Huang, J. Q.; Cheng, X. B.; Guo, X. F.; Ding, W. P.; Zhu, W. C.; Zhang, Q., Catalytic Self-Limited Assembly at Hard Templates: A Mesoscale Approach to Graphene Nanoshells for Lithium-Sulfur Batteries. *Acs Nano* **2014,** *8*, 11280-11289.
29. Sun, Q.; He, B.; Zhang, X. Q.; Lu, A. H., Engineering of Hollow Core-Shell Interlinked Carbon Spheres for Highly Stable Lithium-Sulfur Batteries. *Acs Nano* **2015,** *9*, 8504-8513.
30. Lee, J. T.; Zhao, Y. Y.; Thieme, S.; Kim, H.; Oschatz, M.; Borchardt, L.; Magasinski, A.; Cho, W. I.; Kaskel, S.; Yushin, G., Sulfur-Infiltrated Micro- and Mesoporous Silicon Carbide-Derived Carbon Cathode for High-Performance Lithium Sulfur Batteries. *Adv Mater* **2013,** *25*, 4573-4579.
31. Jayaprakash, N.; Shen, J.; Moganty, S. S.; Corona, A.; Archer, L. A., Porous Hollow Carbon@Sulfur Composites for High-Power Lithium-Sulfur Batteries. *Angew Chem Int Edit* **2011,** *50*, 5904-5908.
32. Shi, J. L.; Peng, H. J.; Zhu, L.; Zhu, W. C.; Zhang, Q., Template growth of porous graphene microspheres on layered double oxide catalysts and their applications in lithium-sulfur batteries. *Carbon* **2015,** *92*, 96-105.

33. Liang, C. D.; Dudney, N. J.; Howe, J. Y., Hierarchically Structured Sulfur/Carbon Nanocomposite Material for High-Energy Lithium Battery. *Chem Mater* **2009,** *21*, 4724-4730.
34. Chen, S. R.; Zhai, Y. P.; Xu, G. L.; Jiang, Y. X.; Zhao, D. Y.; Li, J. T.; Huang, L.; Sun, S. G., Ordered mesoporous carbon/sulfur nanocomposite of high performances as cathode for lithium-sulfur battery. *Electrochim Acta* **2011,** *56*, 9549-9555.
35. Li, X. L.; Cao, Y. L.; Qi, W.; Saraf, L. V.; Xiao, J.; Nie, Z. M.; Mietek, J.; Zhang, J. G.; Schwenzer, B.; Liu, J., Optimization of mesoporous carbon structures for lithium-sulfur battery applications. *J Mater Chem* **2011,** *21*, 16603-16610.
36. Sahore, R.; Estevez, L. P.; Ramanujapuram, A.; DiSalvo, F. J.; Giannelis, E. P., High-rate lithium-sulfur batteries enabled by hierarchical porous carbons synthesized via ice templation. *Journal of Power Sources* **2015,** *297*, 188-194.
37. Wang, D. X.; Fu, A. P.; Li, H. L.; Wang, Y. Q.; Guo, P. Z.; Liu, J. Q.; Zhao, X. S., Mesoporous carbon spheres with controlled porosity for high-performance lithium-sulfur batteries. *Journal of Power Sources* **2015,** *285*, 469-477.
38. Zhou, W. D.; Yu, Y. C.; Chen, H.; DiSalvo, F. J.; Abruna, H. D., Yolk-Shell Structure of Polyaniline-Coated Sulfur for Lithium-Sulfur Batteries. *J Am Chem Soc* **2013,** *135*, 16736-16743.
39. Wang, H. L.; Yang, Y.; Liang, Y. Y.; Robinson, J. T.; Li, Y. G.; Jackson, A.; Cui, Y.; Dai, H. J., Graphene-Wrapped Sulfur Particles as a Rechargeable Lithium-Sulfur Battery Cathode Material with High Capacity and Cycling Stability. *Nano Lett* **2011,** *11*, 2644-2647.
40. Seh, Z. W.; Li, W. Y.; Cha, J. J.; Zheng, G. Y.; Yang, Y.; McDowell, M. T.; Hsu, P. C.; Cui, Y., Sulphur-TiO2 yolk-shell nanoarchitecture with internal void space for long-cycle lithium-sulphur batteries. *Nat Commun* **2013,** *4*, 1331.
41. Liu, S. K.; Xie, K.; Li, Y. J.; Chen, Z. X.; Hong, X. B.; Zhou, L. J.; Yuan, J. F.; Zheng, C. M., Graphene oxide wrapped hierarchical porous carbon-sulfur composite cathode with enhanced cycling and rate performance for lithium sulfur batteries. *Rsc Adv* **2015,** *5*, 5516-5522.
42. Zhou, G. M.; Zhao, Y. B.; Zu, C. X.; Manthiram, A., Free-standing TiO2 nanowire-embedded graphene hybrid membrane for advanced Li/dissolved polysulfide batteries. *Nano Energy* **2015,** *12*, 240-249.
43. Zhang, Q. F.; Wang, Y. P.; Seh, Z. W.; Fu, Z. H.; Zhang, R. F.; Cui, Y., Understanding the Anchoring Effect of Two-Dimensional Layered Materials for Lithium-Sulfur Batteries. *Nano Lett* **2015,** *15*, 3780-3786.
44. Liang, X.; Hart, C.; Pang, Q.; Garsuch, A.; Weiss, T.; Nazar, L. F., A highly efficient polysulfide mediator for lithium-sulfur batteries. *Nat Commun* **2015,** *6*, 5682.
45. Pang, Q.; Kundu, D.; Cuisinier, M.; Nazar, L. F., Surface-enhanced redox chemistry of polysulphides on a metallic and polar host for lithium-sulphur batteries. *Nat Commun* **2014,** *5*, 5759.
46. Yao, H. B.; Zheng, G. Y.; Hsu, P. C.; Kong, D. S.; Cha, J. J.; Li, W. Y.; Seh, Z. W.; McDowell, M. T.; Yan, K.; Liang, Z., et al., Improving lithium-sulphur batteries through spatial control of sulphur species deposition on a hybrid electrode surface. *Nat Commun* **2014,** *5*, 3943.

47. Su, Y. S.; Manthiram, A., A new approach to improve cycle performance of rechargeable lithium-sulfur batteries by inserting a free-standing MWCNT interlayer. *Chem Commun* **2012,** *48*, 8817-8819.
48. Seh, Z. W.; Li, W.; Cha, J. J.; Zheng, G.; Yang, Y.; McDowell, M. T.; Hsu, P.-C.; Cui, Y., Sulphur–TiO2 yolk–shell nanoarchitecture with internal void space for long-cycle lithium–sulphur batteries. *Nat. Commun.* **2013,** *4*, 1331.
49. Carter, R.; Oakes, L.; Muralidharan, N.; Cohn, A. P.; Douglas, A.; Pint, C. L., Polysulfide Anchoring Mechanism Revealed by Atomic Layer Deposition of V2O5 and Sulfur-Filled Carbon Nanotubes for Lithium-Sulfur Batteries. *ACS Appl. Mater. Interfaces* **2017**, 7185-7192.
50. Share, K.; Westover, A.; Li, M.; Pint, C. L., Surface Engineering of Nanomaterials for Improved Energy Storage – A Review. *Chem. Eng. Sci.* **2016,** *154*, 3-19.
51. Carter, R.; Ejorh, D.; Share, K.; Cohn, A. P.; Douglas, A.; Muralidiharan, N.; Tovar, T.; Pint, C. L., Surface Oxidized Mesoporous Carbons Derived from Porous Silicon as Dual Polysulfide Confinement and Anchoring Cathodes in Lithium Sulfur Batteries. *J Power Sources* **2016,** *330*, 70-77.
52. Oakes, L.; Westover, A.; Mares, J. W.; Chatterjee, S.; Erwin, W. R.; Bardhan, R.; Weiss, S. M.; Pint, C. L., Surface engineered porous silicon for stable, high performance electrochemical supercapacitors. *Sci. Rep. UK* **2013,** *3*, 3020.
53. Share, K.; Carter, R.; Nikoleav, P.; Hooper, D.; Oakes, L.; Cohn, A. P.; Rao, R.; Puretzky, A. A.; Geohegan, D. B.; Maruyama, B., et al., Nanoscale silicon as a catalyst for graphene growth; Mechanistic insight from in-situ Raman Spectroscopy. *J. Phys. Chem. C* **2016,** *120*, 14180-14186.
54. Chatterjee, S.; Carter, R.; Oakes, L.; Erwin, W. R.; Bardhan, R.; Pint, C. L., Electrochemical and Corrosion Stability of Nanostructured Silicon by Graphene Coatings: Toward High Power Porous Silicon Supercapacitors. *J Phys Chem C* **2014,** *118*, 10893-10902.
55. Douglas, A.; Muralidharan, N.; Carter, R.; Share, K.; Pint, C. L., Ultrafast triggered transient energy storage by atomic layer deposition into porous silicon for integrated transient electronics. *Nanoscale* **2016,** *8*, 7384-7390.
56. Westover, A. S.; Tian, J. W.; Bernath, S.; Oakes, L.; Edwards, R.; Shabab, F. N.; Chatterjee, S.; Anilkumar, A. V.; Pint, C. L., A Multifunctional Load-Bearing Solid-State Supercapacitor. *Nano Lett* **2014,** *14*, 3197-3202.
57. Westover, A. S.; Freudiger, D.; Gani, Z. S.; Share, K.; Oakes, L.; Carter, R. E.; Pint, C. L., On-chip high power porous silicon lithium ion batteries with stable capacity over 10 000 cycles. *Nanoscale* **2015,** *7*, 98-103.
58. Carter, R.; Chatterjee, S.; Gordon, E.; Share, K.; Erwin, W. R.; Cohn, A. P.; Bardhan, R.; Pint, C. L., Corrosion resistant three-dimensional nanotextured silicon for water photo-oxidation. *Nanoscale* **2015,** *7*, 16755-16762.
59. Cohn, A. P.; Erwin, W. R.; Share, K.; Oakes, L.; Westover, A. S.; Carter, R. E.; Bardhan, R.; Pint, C. L., All Silicon Electrode Photocapacitor for Integrated Energy Storage and Conversion. *Nano Lett* **2015,** *15*, 2727-2731.
60. T., M.; Westover, A.; Carter, R.; Oakes, L.; Douglas, A.; Pint, C. L., Particulate-free porous silicon networks for efficient capacitive deionization water desalination. *Sci. Rep. UK* **2016,** *6*, 24680.

61. Dorfler, S.; Hagen, M.; Althues, H.; Tubke, J.; Kaskel, S.; Hoffmann, M. J., High capacity vertical aligned carbon nanotube/sulfur composite cathodes for lithium-sulfur batteries. *Chem Commun* **2012,** *48*, 4097-4099.
62. Carter, R.; Oakes, L.; Muralidharan, N.; Pint, C. L., Isothermal sulfur condensation into carbon scaffolds: Improved loading, performance, and scalability for lithium sulfur battery cathodes. *J. Phys. Chem. C* **2017**, DOI: 10.1021/acs.jpcc.7b01117.
63. Cohn, A. P.; Oakes, L.; Carter, R.; Chatterjee, S.; Westover, A. S.; Share, K.; Pint, C. L., Assessing the improved performance of freestanding, flexible graphene and carbon nanotube hybrid foams for lithium ion battery anodes. *Nanoscale* **2014,** *6*, 4669-4675.
64. Oakes, L.; Carter, R.; Pint, C. L., Nanoscale Defect Engineering of Lithium-Sulfur Battery Composite Cathodes for Improved Performance. *Nanoscale* **2016,** *8*, 19368-19375.
65. Oakes, L.; Cohn, A. P.; Westover, A. S.; Pint, C. L., Electrophoretic stabilization of freestanding pristine graphene foams with carbon nanotubes for enhanced optical and electrical response. *Mater Lett* **2015,** *159*, 261-264.
66. Oakes, L.; Hanken, T.; Carter, R.; Yates, W.; Pint, C. L., Roll-to-Roll Nanomanufacturing of Hybrid Nanostructures for Energy Storage Device Design. *Acs Appl Mater Inter* **2015,** *7*, 14201-14210.
67. Oakes, L.; Muralidharan, N.; Cohn, A. P.; Pint, C. L., Catalyst morphology matters for lithium-oxygen battery cathodes. *Nanotechnology* **2016,** *27*, 495404.
68. Oakes, L.; Westover, A.; Mahjouri-Samani, M.; Chatterjee, S.; Puretzky, A. A.; Rouleau, C.; Geohegan, D. B.; Pint, C. L., Uniform, Homogenous Coatings of Carbon Nanohorns on Arbitrary Substrates from Common Solvents. *Acs Appl Mater Inter* **2013,** *5*, 13153-13160.
69. Oakes, L.; Carter, R.; Pint, C. L., Nanoscale defect engineering of lithium–sulfur battery composite cathodes for improved performance. *Nanoscale* **2016,** *8*, 19368-19375.
70. Davis, B. F.; Yan, X. Y.; Muralidharan, N.; Oakes, L.; Pint, C. L.; Maschmann, M. R., Electrically Conductive Hierarchical Carbon Nanotube Networks with Tunable Mechanical Response. *Acs Appl Mater Inter* **2016,** *8*, 28004-28011.
71. Xin, S.; Yin, Y. X.; Guo, Y. G.; Wan, L. J., A High-Energy Room-Temperature Sodium-Sulfur Battery. *Adv Mater* **2014,** *26*, 1261-1265.
72. Cohn, A. P.; Muralidharan, N.; Carter, R.; Share, K.; Pint, C. L., An anode-free sodium battery through in-situ plating of sodium metal. *Nano Lett.* **2017,** *17*, 1296-1301.
73. Yu, X. W.; Manthiram, A., Room-Temperature Sodium-Sulfur Batteries with Liquid-Phase Sodium Polysulfide Catholytes and Binder-Free Multiwall Carbon Nanotube Fabric Electrodes. *J Phys Chem C* **2014,** *118*, 22952-22959.
74. Yu, X. W.; Manthiram, A., Highly Reversible Room-Temperature Sulfur/Long-Chain Sodium Polysulfide Batteries. *J Phys Chem Lett* **2014,** *5*, 1943-1947.
75. Niu, S. Z.; Zhou, G. M.; Lv, W.; Shi, H. F.; Luo, C.; He, Y. B.; Li, B. H.; Yang, Q. H.; Kang, F. Y., Sulfur confined in nitrogen-doped microporous carbon used in a carbonate-based electrolyte for long-life, safe lithium-sulfur batteries. *Carbon* **2016,** *109*, 1-6.
76. Chen, Y. M.; Liang, W. F.; Li, S.; Zou, F.; Bhaway, S. M.; Qiang, Z.; Gao, M.; Vogt, B. D.; Zhu, Y., A nitrogen doped carbonized metal-organic framework for high stability room temperature sodium-sulfur batteries. *J Mater Chem A* **2016,** *4*, 12471-12478.

77. Fan, L.; Ma, R. F.; Yang, Y. H.; Chen, S. H.; Lu, B. A., Covalent sulfur for advanced room temperature sodium-sulfur batteries. *Nano Energy* **2016,** *28*, 304-310.
78. Carter, R.; Oakes, L.; Douglas, A.; Muralidharan, N.; Cohn, A. P.; Pint, C. L., A Sugar Derived Room Temperature Sodium Sulfur Battery with Long Term Cycling Stability. *Nano Lett.* **2017,** *17*, 1863-1869.
79. Peng, H. J.; Zhang, Q., Designing Host Materials for Sulfur Cathodes: From Physical Confinement to Surface Chemistry. *Angew Chem Int Edit* **2015,** *54*, 11018-11020.
80. Ji, X. L.; Lee, K. T.; Nazar, L. F., A highly ordered nanostructured carbon-sulphur cathode for lithium-sulphur batteries. *Nat Mater* **2009,** *8*, 500-506.
81. Zheng, G. Y.; Yang, Y.; Cha, J. J.; Hong, S. S.; Cui, Y., Hollow Carbon Nanofiber-Encapsulated Sulfur Cathodes for High Specific Capacity Rechargeable Lithium Batteries. *Nano Lett* **2011,** *11*, 4462-4467.
82. Scheers, J.; Fantini, S.; Johansson, P., A review of electrolytes for lithium-sulphur batteries. *Journal of Power Sources* **2014,** *255*, 204-218.
83. Ji, L. W.; Rao, M. M.; Zheng, H. M.; Zhang, L.; Li, Y. C.; Duan, W. H.; Guo, J. H.; Cairns, E. J.; Zhang, Y. G., Graphene Oxide as a Sulfur Immobilizer in High Performance Lithium/Sulfur Cells. *J Am Chem Soc* **2011,** *133*, 18522-18525.
84. Zhou, W. D.; Wang, C. M.; Zhang, Q. L.; Abruna, H. D.; He, Y.; Wang, J. W.; Mao, S. X.; Xiao, X. C., Tailoring Pore Size of Nitrogen-Doped Hollow Carbon Nanospheres for Confining Sulfur in Lithium-Sulfur Batteries. *Adv Energy Mater* **2015,** *5*, 1401752.
85. Xu, C. M.; Wu, Y. S.; Zhao, X. Y.; Wang, X. L.; Du, G. H.; Zhang, J.; Tu, J. P., Sulfur/three-dimensional graphene composite for high performance lithium-sulfur batteries. *Journal of Power Sources* **2015,** *275*, 22-25.
86. Stobinski, L.; Lesiak, B.; Kover, L.; Toth, J.; Biniak, S.; Trykowski, G.; Judek, J., Multiwall carbon nanotubes purification and oxidation by nitric acid studied by the FTIR and electron spectroscopy methods. *J Alloy Compd* **2010,** *501*, 77-84.
87. Barchasz, C.; Molton, F.; Duboc, C.; Lepretre, J. C.; Patoux, S.; Alloin, F., Lithium/Sulfur Cell Discharge Mechanism: An Original Approach for Intermediate Species Identification. *Anal Chem* **2012,** *84*, 3973-3980.
88. Wei, Y. J.; Tao, Y. Q.; Zhang, C. F.; Wang, J. T.; Qiao, W. M.; Ling, L. C.; Long, D. H., Layered carbide-derived carbon with hierarchically porous structure for high rate lithium-sulfur batteries. *Electrochim Acta* **2016,** *188*, 385-392.
89. Su, Y. S.; Fu, Y. Z.; Cochell, T.; Manthiram, A., A strategic approach to recharging lithium-sulphur batteries for long cycle life. *Nat Commun* **2013,** *4*, 2984.
90. Evers, S.; Nazar, L. F., New Approaches for High Energy Density Lithium–Sulfur Battery Cathodes. *Acc. Chem. Res.* **2013,** *46*, 1135-1143.
91. Evers, S.; Nazar, L. F., New Approaches for High Energy Density Lithium Sulfur Battery Cathodes. *Acc. Chem. Res.* **2012,** *46*, 1135-1143.
92. De Volder, M. F. L.; Tawfick, S. H.; Baughman, R. H.; Hart, A. J., Carbon Nanotubes: Present and Future Commercial Applications. *Science* **2013,** *339*, 535-539.
93. Baughman, R. H.; Zakhidov, A. A.; de Heer, W. A., Carbon Nanotubes - The Route Toward Applications. *Science* **2002,** *297*, 787-792.

94. Yu, M. F.; Files, B. S.; Arepalli, S.; Ruoff, R. S., Tensile Loading of Ropes of Single Wall Carbon Nanotubes and Their Mechanical Properties. *Phys. Rev. Lett.* **2000,** *84*, 5552-5555.
95. Liu, L. Q.; Ma, W. J.; Zhang, Z., Macroscopic Carbon Nanotube Assemblies: Preparation, Properties, and Potential Applications. *Small* **2011,** *7*, 1504-1520.
96. Ericson, L. M.; Fan, H.; Peng, H. Q.; Davis, V. A.; Zhou, W.; Sulpizio, J.; Wang, Y. H.; Booker, R.; Vavro, J.; Guthy, C., et al., Macroscopic, Neat, Single-Walled Carbon Nanotube Fibers. *Science* **2004,** *305*, 1447-1450.
97. Worsley, M. A.; Kucheyev, S. O.; Satcher, J. H.; Hamza, A. V.; Baumann, T. F., Mechanically Robust and Electrically Conductive Carbon Nanotube Foams. *Appl Phys Lett* **2009,** *94*, 073115.
98. Shi, Z.; Chen, X. J.; Wang, X. W.; Zhang, T.; Jin, J., Fabrication of Superstrong Ultrathin Free-Standing Single-Walled Carbon Nanotube Films via a Wet Process. *Adv. Funct. Mater.* **2011,** *21*, 4358-4363.
99. Pint, C. L.; Xu, Y. Q.; Pasquali, M.; Hauge, R. H., Formation of Highly Dense Aligned Ribbons and Transparent Films of Single-Walled Carbon Nanotubes Directly From Carpets. *Acs Nano* **2008,** *2*, 1871-1878.
100. Nanot, S.; Cummings, A. W.; Pint, C. L.; Ikeuchi, A.; Akiho, T.; Sueoka, K.; Hauge, R. H.; Leonard, F.; Kono, J., Broadband, Polarization-Sensitive Photodetector Based on Optically-Thick Films of Macroscopically Long, Dense, and Aligned Carbon Nanotubes. *Sci. Rep.* **2013,** *3*, 1335.
101. Pint, C. L.; Nicholas, N. W.; Xu, S.; Sun, Z. Z.; Tour, J. M.; Schmidt, H. K.; Gordon, R. G.; Hauge, R. H., Three Dimensional Solid-State Supercapacitors From Aligned Single-Walled Carbon Nanotube Array Templates. *Carbon* **2011,** *49*, 4890-4897.
102. Pint, C. L.; Xu, Y. Q.; Moghazy, S.; Cherukuri, T.; Alvarez, N. T.; Haroz, E. H.; Mahzooni, S.; Doorn, S. K.; Kono, J.; Pasquali, M., et al., Dry Contact Transfer Printing of Aligned Carbon Nanotube Patterns and Characterization of Their Optical Properties for Diameter Distribution and Alignment. *Acs Nano* **2010,** *4*, 1131-1145.
103. Dong, P.; Pint, C. L.; Hainey, M.; Mirri, F.; Zhan, Y. J.; Zhang, J.; Pasquali, M.; Hauge, R. H.; Verduzco, R.; Jiang, M. A., et al., Vertically Aligned Single-Walled Carbon Nanotubes as Low-cost and High Electrocatalytic Counter Electrode for Dye-Sensitized Solar Cells. *ACS Appl. Mater. Interfaces* **2011,** *3*, 3157-3161.
104. Kang, S. J.; Kocabas, C.; Ozel, T.; Shim, M.; Pimparkar, N.; Alam, M. A.; Rotkin, S. V.; Rogers, J. A., High-Performance Electronics Using Dense, Perfectly Aligned Arrays of Single-Walled Carbon Nanotubes. *Nat. Nanotechnol.* **2007,** *2*, 230-236.
105. Qu, L. T.; Dai, L. M.; Stone, M.; Xia, Z. H.; Wang, Z. L., Carbon Nanotube Arrays with Strong Shear Binding-on and Easy Normal Lifting-off. *Science* **2008,** *322*, 238-242.
106. Ren, L.; Pint, C. L.; Booshenri, L. G.; Rice, W. D.; Wang, X. F.; Hilton, D. J.; Takeya, K.; Kawayama, I.; Tonouchi, M.; Hauge, R. H., et al., Carbon Nanotube Terahertz Polarizer. *Nano Lett.* **2009,** *9*, 2610-2613.
107. Moore, V. C.; Strano, M. S.; Haroz, E. H.; Hauge, R. H.; Smalley, R. E.; Schmidt, J.; Talmon, Y., Individually Suspended Single-Walled Carbon Nanotubes in Various Surfactants. *Nano Lett.* **2003,** *3*, 1379-1382.
108. O'Connell, M. J.; Boul, P.; Ericson, L. M.; Huffman, C.; Wang, Y. H.; Haroz, E.; Kuper, C.; Tour, J.; Ausman, K. D.; Smalley, R. E., Reversible Water-Solubilization of

Single-Walled Carbon Nanotubes by Polymer Wrapping. *Chem. Phys. Lett.* **2001,** *342*, 265-271.
109. Vaisman, L.; Wagner, H. D.; Marom, G., The Role of Surfactants in Dispersion of Carbon Nanotubes. *Adv. Colloid Interfac.* **2006,** *128*, 37-46.
110. Sun, Z.; Nicolosi, V.; Rickard, D.; Bergin, S. D.; Aherne, D.; Coleman, J. N., Quantitative Evaluation of Surfactant-Stabilized Single-Walled Carbon Nanotubes: Dispersion Quality and its Correlation with Zeta Potential. *J. Phys. Chem. C* **2008,** *112*, 10692-10699.
111. Park, J. G.; Smithyman, J.; Lin, C. Y.; Cooke, A.; Kismarahardja, A. W.; Li, S.; Liang, R.; Brooks, J. S.; Zhang, C.; Wang, B., Effects of Surfactants and Alignment on the Physical Properties of Single-Walled Carbon Nanotube Buckypaper. *J. Appl. Phys.* **2009,** *106*, 104310.
112. Behabtu, N.; Lomeda, J. R.; Green, M. J.; Higginbotham, A. L.; Sinitskii, A.; Kosynkin, D. V.; Tsentalovich, D.; Parra-Vasquez, A. N. G.; Schmidt, J.; Kesselman, E., et al., Spontaneous High-Concentration Dispersions and Liquid Crystals of Graphene. *Nature Nanotechnol.* **2010,** *5*, 406-411.
113. Davis, V. A.; Parra-Vasquez, A. N. G.; Green, M. J.; Rai, P. K.; Behabtu, N.; Prieto, V.; Booker, R. D.; Schmidt, J.; Kesselman, E.; Zhou, W., et al., True Solutions of Single-Walled Carbon Nanotubes for Assembly into Macroscopic Materials. *Nature Nanotechnol.* **2009,** *4*, 830-834.
114. Parra-Vasquez, A. N. G.; Behabtu, N.; Green, M. J.; Pint, C. L.; Young, C. C.; Schmidt, J.; Kesselman, E.; Goyal, A.; Ajayan, P. M.; Cohen, Y., et al., Spontaneous Dissolution of Ultralong Single- and Multiwalled Carbon Nanotubes. *Acs Nano* **2010,** *4*, 3969-3978.
115. Bergin, S. D.; Sun, Z. Y.; Streich, P.; Hamilton, J.; Coleman, J. N., New Solvents for Nanotubes: Approaching the Dispersibility of Surfactants. *J. Phys. Chem. C* **2010,** *114*, 231-237.
116. Bergin, S. D.; Nicolosi, V.; Streich, P. V.; Giordani, S.; Sun, Z. Y.; Windle, A. H.; Ryan, P.; Niraj, N. P. P.; Wang, Z. T. T.; Carpenter, L., et al., Towards Solutions of Single-Walled Carbon Nanotubes in Common Solvents. *Adv. Mater.* **2008,** *20*, 1876.
117. Hernandez, Y.; Nicolosi, V.; Lotya, M.; Blighe, F. M.; Sun, Z. Y.; De, S.; McGovern, I. T.; Holland, B.; Byrne, M.; Gun'ko, Y. K., et al., High-yield production of graphene by liquid-phase exfoliation of graphite. *Nat Nanotechnol* **2008,** *3*, 563-568.
118. Giordani, S.; Bergin, S. D.; Nicolosi, V.; Lebedkin, S.; Kappes, M. M.; Blau, W. J.; Coleman, J. N., Debundling of Single-Walled Nanotubes by Dilution: Observation of Large Populations of Individual Nanotubes in Amide Solvent Dispersions. *J Phys Chem B* **2006,** *110*, 15708-15718.
119. Furtado, C. A.; Kim, U. J.; Gutierrez, H. R.; Pan, L.; Dickey, E. C.; Eklund, P. C., Debundling and Dissolution of Single-Walled Carbon Nanotubes in Amide Solvents. *J. Am. Chem. Soc.* **2004,** *126*, 6095-6105.
120. Ausman, K. D.; Piner, R.; Lourie, O.; Ruoff, R. S.; Korobov, M., Organic Solvent Dispersions of Single-Walled Carbon Nanotubes: Toward Solutions of Pristine Nanotubes. *J Phys Chem B* **2000,** *104*, 8911-8915.
121. Behabtu, N.; Young, C. C.; Tsentalovich, D. E.; Kleinerman, O.; Wang, X.; Ma, A. W. K.; Bengio, E. A.; ter Waarbeek, R. F.; de Jong, J. J.; Hoogerwerf, R. E., et al., Strong,

Light, Multifunctional Fibers of Carbon Nanotubes with Ultrahigh Conductivity. *Science* **2013,** *339*, 182-186.
122. Cho, J.; Konopka, K.; Rozniatowski, K.; Garcia-Lecina, E.; Shaffer, M. S. P.; Boccaccini, A. R., Characterisation of Carbon Nanotube Films Deposited by Electrophoretic Deposition. *Carbon* **2009,** *47*, 58-67.
123. Kamat, P. V.; Thomas, K. G.; Barazzouk, S.; Girishkumar, G.; Vinodgopal, K.; Meisel, D., Self-Assembled Linear Bundles of Single Wall Carbon Nanotubes and Their Alignment and Deposition as a Film in a DC Field. *J. Am. Chem. Soc.* **2004,** *126*, 10757-10762.
124. Gooding, J. J., Nanostructuring Electrodes With Carbon Nanotubes: A Review on Electrochemistry and Applications for Sensing. *Electrochim. Acta* **2005,** *50*, 3049-3060.
125. De Volder, M.; Tawfick, S. H.; Park, S. J.; Copic, D.; Zhao, Z. Z.; Lu, W.; Hart, A. J., Diverse 3D Microarchitectures Made by Capillary Forming of Carbon Nanotubes. *Adv. Mater.* **2010,** *22*, 4384.
126. Girishkumar, G.; McCloskey, B.; Luntz, A. C.; Swanson, S.; Wilcke, W., Lithium - Air Battery: Promise and Challenges. *J. Phys. Chem. Lett.* **2010,** *1*, 2193-2203.
127. Kraytsberg, A.; Ein-Eli, Y., Review on Li-air Batteries-Opportunities, Limitations and Perspective. *J Power Sources* **2011,** *196*, 886-893.
128. Wang, H.; Xie, K.; Wang, L. Y.; Han, Y., All Carbon Nanotubes and Freestanding Air Electrodes for Rechargeable Li-Air Batteries. *Rsc Adv.* **2013,** *3*, 8236-8241.
129. Bruce, P. G.; Freunberger, S. A.; Hardwick, L. J.; Tarascon, J. M., Li-O-2 and Li-S Batteries with High Energy Storage. . *Nat Mater* **2012,** *11*, 19-29.
130. Yin, Y. X.; Xin, S.; Guo, Y. G.; Wan, L. J., Lithium–Sulfur Batteries: Electrochemistry, Materials, and Prospects. *Angew. Chem. Int. Ed.* **2013,** *52*, 13186-13200.
131. Chen, R.; Zhao, T.; Wu, F., From a Historic Review to Horizons Beyond: Lithium–Sulphur Batteries Run on the Wheels. *Chem. Commun.* **2015,** *51*, 18-33.
132. Wild, M.; O'Neill, L.; Zhang, T.; Purkayastha, R.; Minton, G.; Marinescu, M.; Offer, G., Lithium Sulfur Batteries, A Mechanistic Review. *Energ. Environ. Sci.* **2015,** *8*, 3477-3494.
133. Shaibani, M.; Akbari, A.; Sheath, P.; Easton, C. D.; Chakarborty Banerjee, P.; Konstas, K.; Fakhfouri, A.; Barghamadi, M.; Musameh, M. M.; Best, A. S., et al., Suppressed Polysulfide Crossover in Li–S Batteries through a High-Flux Graphene Oxide Membrane Supported on a Sulfur Cathode. *Acs Nano* **2016,** *10*, 7768-7779.
134. Tao, X. Y.; Wang, J. G.; Liu, C.; Wang, H. T.; Yao, H. B.; Zheng, G. Y.; Seh, Z. W.; Cai, Q. X.; Li, W. Y.; Zhou, G. M., et al., Balancing surface adsorption and diffusion of lithium-polysulfides on nonconductive oxides for lithium-sulfur battery design. *Nat. Commun.* **2016,** *7*, 11203.
135. Manthiram, A.; Fu, Y.; Chung, S.-H.; Zu, C.; Su, Y.-S., Rechargeable Lithium–Sulfur Batteries. *Chem. Rev.* **2014,** *114*, 11751-11787.
136. Lacey, M. J.; Jeschull, F.; Edström, K.; Brandell, D., Functional, Water-Soluble Binders for Improved Capacity and Stability of Lithium–Sulfur Batteries. *J Power Sources* **2014,** *264*, 8-14.
137. Urbonaite, S.; Poux, T.; Novák, P., Progress towards commercially viable Li–S battery cells. *Adv. Energy Mater.* **2015,** *5*, 1500118.

138. Cheng, X. B.; Huang, J. Q.; Zhang, Q.; Peng, H. J.; Zhao, M. Q.; Wei, F., Aligned Carbon Nanotube/Sulfur Composite Cathodes with High Sulfur Content for Lithium-Sulfur Batteries. *Nano Energy* **2014,** *4*, 65-72.
139. Du, W. C.; Yin, Y. X.; Zeng, X. X.; Shi, J. L.; Zhang, S. F.; Wan, L. J.; Guo, Y. G., Wet Chemistry Synthesis of Multidimensional Nanocarbon-Sulfur Hybrid Materials with Ultrahigh Sulfur Loading for Lithium-Sulfur Batteries. *Acs Appl Mater Inter* **2016,** *8*, 3584-3590.
140. Helen, M.; Reddy, M. A.; Diemant, T.; Golla-Schindler, U.; Behm, R. J.; Kaiser, U.; Fichtner, M., Single step transformation of sulphur to Li2S2/Li2S in Li-S batteries. *Sci Rep-Uk* **2015,** *5*, 12146
141. Xin, S.; Gu, L.; Zhao, N. H.; Yin, Y. X.; Zhou, L. J.; Guo, Y. G.; Wan, L. J., Smaller Sulfur Molecules Promise Better Lithium-Sulfur Batteries. *J Am Chem Soc* **2012,** *134*, 18510-18513.
142. Xu, Y. H.; Wen, Y.; Zhu, Y. J.; Gaskell, K.; Cychosz, K. A.; Eichhorn, B.; Xu, K.; Wang, C. S., Confined Sulfur in Microporous Carbon Renders Superior Cycling Stability in Li/S Batteries. *Adv Funct Mater* **2015,** *25*, 4312-4320.
143. Zhang, B.; Qin, X.; Li, G. R.; Gao, X. P., Enhancement of Long Stability of Sulfur Cathode by Encapsulating Sulfur into Micropores of Carbon Spheres. *Energ. Environ. Sci.* **2010,** *3*, 1531-1537.
144. Stobinski, L.; Lesiak, B.; Kover, L.; Toth, J.; Biniak, S.; Trykowski, G.; Judek, J., Multiwall Carbon Nanotubes Purification and Oxidation by Nitric Acid Studied by the FTIR and Electron Spectroscopy Methods. *J. Alloy Compd.* **2010,** *501*, 77-84.
145. Yao, H. B.; Yan, K.; Li, W. Y.; Zheng, G. Y.; Kong, D. S.; Seh, Z. W.; Narasimhan, V. K.; Liang, Z.; Cui, Y., Improved Lithium-Sulfur Batteries with a Conductive Coating on the Separator to Prevent the Accumulation of Inactive S-Related Species at the Cathode-Separator Interface. *Energ. Environ. Sci.* **2014,** *7*, 3381-3390.
146. He, B.; Li, W.-C.; Yang, C.; Wang, S.-Q.; Lu, A.-H., Incorporating Sulfur Inside the Pores of Carbons for Advanced Lithium–Sulfur Batteries: An Electrolysis Approach. *Acs Nano* **2016,** *10*, 1633-1639.
147. Evers, S.; Nazar, L. F., Graphene-Enveloped Sulfur in a One Pot Reaction: a Cathode with Good Coulombic Efficiency and High Practical Sulfur Content. *Chem. Commun.* **2012,** *48*, 1233-1235.
148. Sun, L.; Li, M.; Jiang, Y.; Kong, W.; Jiang, K.; Wang, J.; Fan, S., Sulfur Nanocrystals Confined in Carbon Nanotube Network as a Binder-Free Electrode for High-Performance Lithium Sulfur Batteries. *Nano Lett.* **2014,** *14*, 4044-4049.
149. Chung, S. H.; Han, P.; Manthiram, A., A Polysulfide-Trapping Interface for Electrochemically Stable Sulfur Cathode Development. *Acs Appl Mater Inter* **2016,** *8*, 4709-4717.
150. Qie, L.; Manthiram, A., High-Energy-Density Lithium–Sulfur Batteries Based on Blade-Cast Pure Sulfur Electrodes. *ACS Energy Lett.* **2016,** *1*, 46-51.
151. Xu, J. T.; Shui, J. L.; Wang, J. L.; Wang, M.; Liu, H. K.; Dou, S. X.; Jeon, I. Y.; Seo, J. M.; Baek, J. B.; Dai, L. M., Sulfur-Graphene Nanostructured Cathodes via Ball-Milling for High-Performance LithiumSulfur Batteries. *Acs Nano* **2014,** *8*, 10920-10930.
152. Liang, X.; Kaiser, M. R.; Konstantinov, K.; Tandiono, R.; Wang, Z. X.; Chen, C. H.; Liu, H. K.; Dou, S. X.; Wang, J. Z., Ternary Porous Sulfur/Dual-Carbon Architectures for Lithium/Sulfur Batteries Obtained Continuously and on a Large Scale via an Industry-

Oriented Spray-Pyrolysis/Sublimation Method. *Acs Appl Mater Inter* **2016,** *8*, 25251-25260.
153. Zhou, W. D.; Guo, B. K.; Gao, H. C.; Goodenough, J. B., Low-Cost Higher Loading of a Sulfur Cathode. *Adv Energy Mater* **2016,** *6*, 1500046.
154. Wang, J. L.; Yin, L. C.; Jia, H.; Yu, H. T.; He, Y. S.; Yang, J.; Monroe, C. W., Hierarchical Sulfur-Based Cathode Materials with Long Cycle Life for Rechargeable Lithium Batteries. *Chemsuschem* **2014,** *7*, 563-569.
155. Yang, Y.; Zheng, G. Y.; Cui, Y., A Membrane-Free Lithium/Polysulfide Semi-Liquid Battery for Large-Scale Energy Storage. *Energ. Environ. Sci.* **2013,** *6*, 1552-1558.
156. Fan, F. Y.; Woodford, W. H.; Li, Z.; Baram, N.; Smith, K. C.; Helal, A.; McKinley, G. H.; Carter, W. C.; Chiang, Y. M., Polysulfide Flow Batteries Enabled by Percolating Nanoscale Conductor Networks. *Nano Lett.* **2014,** *14*, 2210-2218.
157. Sahore, R.; Levin, B. D.; Pan, M.; Muller, D. A.; DiSalvo, F. J.; Giannelis, E. P., Design Principles for Optimum Performance of Porous Carbons in Lithium–Sulfur Batteries. *Adv Energy Mater* **2016**, 1600134.
158. Wang, Y.; Chen, L.; Scudiero, L.; Zhong, W. H., The Beauty of Frost: Nano-Sulfur Assembly via Low Pressure Vapour Deposition. *Chem. Commun.* **2015,** *51*, 15967-15970.
159. Cui, Y.; Wu, M.; Scott, C.; Xie, J.; Fu, Y., A Binder-Free Sulfur/Carbon Composite Electrode Prepared by a Sulfur Sublimation Method for Li–S Batteries. *RSC Adv.* **2016,** *6*, 52642-52645.
160. Yarom, M.; Marmur, A., Condensation Enhancement by Surface Porosity: Three-Stage Mechanism. *Langmuir* **2015,** *31*, 8852-8855.
161. Li, J.; Armstrong, B. L.; Daniel, C.; Kiggans, J.; Wood, D. L., Optimization of multicomponent aqueous suspensions of lithium iron phosphate (LiFePO 4) nanoparticles and carbon black for lithium-ion battery cathodes. *J. Colloid and Interface Sci.* **2013,** *405*, 118-124.
162. Chen, H.; Qiu, X.; Zhu, W.; Hagenmuller, P., Synthesis and High Rate Properties of Nanoparticled Lithium Cobalt Oxides as the Cathode Material for Lithium-ion Battery. *Electrochem. Commun.* **2002,** *4*, 488-491.
163. Yu, S. H.; Lee, B.; Choi, S.; Park, S.; Hong, B. H.; Sung, Y. E., Enhancement of Electrochemical Properties by Polysulfide Trapping in a Graphene-Coated Sulfur Cathode on Patterned Current Collector. *Chem. Commun.* **2016,** *52*, 3203-3206.
164. Hart, C. J.; Cuisinier, M.; Liang, X.; Kundu, D.; Garsuch, A.; Nazar, L. F., Rational Design of Sulphur Host Materials for Li-S batteries: Correlating Lithium Polysulphide Adsorptivity and Self-Discharge Capacity Loss. *Chem. Commun.* **2015,** *51*, 2308-2311.
165. Hagen, M.; Hanselmann, D.; Ahlbrecht, K.; Maca, R.; Gerber, D.; Tubke, J., Lithium-Sulfur Cells: The Gap between the State-of-the-Art and the Requirements for High Energy Battery Cells. *Adv Energy Mater* **2015,** *5*, 1401986.
166. Gorlin, Y.; Siebel, A.; Piana, M.; Huthwelker, T.; Jha, H.; Monsch, G.; Kraus, F.; Gasteiger, H. A.; Tromp, M., Operando Characterization of Intermediates Produced in a Lithium-Sulfur Battery. *J Electrochem Soc* **2015,** *162*, A1146-A1155.
167. Yang, Y.; McDowell, M. T.; Jackson, A.; Cha, J. J.; Hong, S. S.; Cui, Y., New Nanostructured Li2S/Silicon Rechargeable Battery with High Specific Energy. *Nano Lett.* **2010,** *10*, 1486-1491.

168. Kozen, A. C.; Lin, C. F.; Pearse, A. J.; Schroeder, M. A.; Han, X. G.; Hu, L. B.; Lee, S. B.; Rubloff, G. W.; Noked, M., Next-Generation Lithium Metal Anode Engineering via Atomic Layer Deposition. *Acs Nano* **2015,** *9*, 5884-5892.
169. Guo, J. C.; Xu, Y. H.; Wang, C. S., Sulfur-Impregnated Disordered Carbon Nanotubes Cathode for Lithium-Sulfur Batteries. *Nano Lett.* **2011,** *11*, 4288-4294.
170. Jin, F. Y.; Xiao, S.; Lu, L. J.; Wang, Y., Efficient Activation of High-Loading Sulfur by Small CNTs Confined Inside a Large CNT for High-Capacity and High-Rate Lithium-Sulfur Batteries. *Nano Lett.* **2016,** *16*, 440-447.
171. Ma, L.; Zhuang, H. L. L.; Wei, S. Y.; Hendrickson, K. E.; Kim, M. S.; Cohn, G.; Hennig, R. G.; Archer, L. A., Enhanced Li-S Batteries Using Amine-Functionalized Carbon Nanotubes in the Cathode. *Acs Nano* **2016,** *10*, 1050-1059.
172. Liang, X.; Garsuch, A.; Nazar, L. F., Sulfur Cathodes Based on Conductive MXene Nanosheets for High-Performance Lithium-Sulfur Batteries. *Angew. Chem., Int. Ed.* **2015,** *54*, 3907-3911.
173. Kim, H.; Lee, J. T.; Lee, D. C.; Magasinski, A.; Cho, W. I.; Yushin, G., Plasma-Enhanced Atomic Layer Deposition of Ultrathin Oxide Coatings for Stabilized Lithium-Sulfur Batteries. *Adv. Energy Mater.* **2013,** *3*, 1308-1315.
174. Yu, M. P.; Ma, J. S.; Song, H. Q.; Wang, A. J.; Tian, F. Y.; Wang, Y. S.; Qiu, H.; Wang, R. M., Atomic Layer Deposited TiO2 on a Nitrogen-Doped Graphene/Sulfur Electrode for High Performance Lithium-Sulfur Batteries. *Energy Environ. Sci.* **2016,** *9*, 1495-1503.
175. Yu, M. P.; Yuan, W. J.; Li, C.; Hong, J. D.; Shi, G. Q., Performance Enhancement of a Graphene-Sulfur Composite as a Lithium-Sulfur Battery Electrode by Coating with an Ultrathin Al2O3 Film via Atomic Layer Deposition. *J. Mater. Chem. A* **2014,** *2*, 7360-7366.
176. Han, X. G.; Xu, Y. H.; Chen, X. Y.; Chen, Y. C.; Weadock, N.; Wan, J. Y.; Zhu, H. L.; Liu, Y. L.; Li, H. Q.; Rubloff, G., et al., Reactivation of Dissolved Polysulfides in Li-S Batteries Based on Atomic Layer Deposition of Al2O3 in Nanoporous Carbon Cloth. *Nano Energy* **2013,** *2*, 1197-1206.
177. Yu, M. P.; Wang, A. J.; Tian, F. Y.; Song, H. Q.; Wang, Y. S.; Li, C.; Hong, J. D.; Shi, G. Q., Dual-Protection of a Graphene-Sulfur Composite by a Compact Graphene Skin and an Atomic Layer Deposited Oxide Coating for a Lithium-Sulfur Battery. *Nanoscale* **2015,** *7*, 5292-5298.
178. Li, X.; Lushington, A.; Sun, Q.; Xiao, W.; Liu, J.; Wang, B. G.; Ye, Y. F.; Nie, K. Q.; Hu, Y. F.; Xiao, Q. F., et al., Safe and Durable High-Temperature Lithium-Sulfur Batteries via Molecular Layer Deposited Coating. *Nano Lett.* **2016,** *16*, 3545-3549.
179. Carter, R.; Oakes, L.; Cohn, A. P.; Holzgrafe, J.; Zarick, H. F.; Chatterjee, S.; Bardhan, R.; Pint, C. L., Solution Assembled Single-Walled Carbon Nanotube Foams: Superior Performance in Supercapacitors, Lithium-Ion, and Lithium-Air Batteries. *J Phys Chem C* **2014,** *118*, 20137-20151.
180. Oakes, L.; Hanken, T.; Carter, R.; Yates, W.; Pint, C. L., Roll-to-Roll Nanomanufacturing of Hybrid Nanostructures for Energy Storage Device Design. *ACS Appl. Mater. & Interfaces* **2015,** *7*, 14201-14210.
181. Carter, R.; Oakes, L.; Cohn, A. P.; Holzgrafe, J.; Zarick, H. F.; Chatterjee, S.; Bardhan, R.; Pint, C. L., Solution Assembled Single-Walled Carbon Nanotube Foams:

Superior Performance in Supercapacitors, Lithium-Ion, and Lithium-Air Batteries. *J. Phys. Chem. C* **2014,** *118*, 20137-20151.
182. Musschoot, J.; Deduytsche, D.; Poelman, H.; Haemers, J.; Van Meirhaeghe, R. L.; Van den Berghe, S.; Detavernier, C., Comparison of Thermal and Plasma-Enhanced ALD/CVD of Vanadium Pentoxide. *J Electrochem Soc* **2009,** *156*, P122-P126.
183. Barchasz, C.; Molton, F.; Duboc, C.; Lepretre, J. C.; Patoux, S.; Alloin, F., Lithium/Sulfur Cell Discharge Mechanism: An Original Approach for Intermediate Species Identification. *Anal. Chem.* **2012,** *84*, 3973-3980.
184. Zhang, Q. F.; Wang, Y. P.; Seh, Z. W.; Fu, Z. H.; Zhang, R. F.; Cui, Y., Understanding the Anchoring Effect of Two-Dimensional Layered Materials for Lithium-Sulfur Batteries. *Nano Lett.* **2015,** *15*, 3780-3786.
185. Baddour-Hadjean, R.; Pereira-Ramos, J. P.; Navone, C.; Smirnov, M., Raman Microspectrometry Study of Electrochemical Lithium Intercalation into Sputtered Crystalline V2O5 Thin Films. *Chem. Mater.* **2008,** *20*, 1916-1923.
186. Zheng, G. Y.; Yang, Y.; Cha, J. J.; Hong, S. S.; Cui, Y., Hollow Carbon Nanofiber-Encapsulated Sulfur Cathodes for High Specific Capacity Rechargeable Lithium Batteries. *Nano Lett.* **2011,** *11*, 4462-4467.
187. Laurent, C.; Flahaut, E.; Peigney, A., The Weight and Density of Carbon Nanotubes versus the Number of Walls and Diameter. *Carbon* **2010,** *48*, 2994-2996.
188. Palanisamy, K.; Um, J. H.; Jeong, M.; Yoon, W. S., Porous V2O5/RGO/CNT hierarchical architecture as a cathode material: Emphasis on the contribution of surface lithium storage. *Sci Rep-Uk* **2016,** *6*, 31275
189. Carter, R.; Ejorh, D.; Share, K.; Cohn, A. P.; Douglas, A.; Muralidharan, N.; Tovar, T. M.; Pint, C. L., Surface Oxidized Mesoporous Carbons Derived from Porous Silicon as Dual Polysulfide Confinement and Anchoring Cathodes in Lithium Sulfur Batteries. *J Power Sources* **2016,** *330*, 70-77.
190. Pang, Q.; Nazar, L. F., Long-Life and High-Areal-Capacity Li S Batteries Enabled by a Light-Weight Polar Host with Intrinsic Polysulfide Adsorption. *Acs Nano* **2016,** *10*, 4111-4118.
191. Sun, L.; Wang, D. T.; Luo, Y. F.; Kong, W. B.; Wu, Y.; Zhang, L. N.; Jiang, K. L.; Li, Q. Q.; Zhang, Y. H.; Wang, J. P., et al., Sulfur Embedded in a Mesoporous Carbon Nanotube Network as a Binder-Free Electrode for High-Performance Lithium Sulfur Batteries. *Acs Nano* **2016,** *10*, 1300-1308.
192. Ye, X. M.; Ma, J.; Hu, Y. S.; Wei, H. Y.; Ye, F. F., MWCNT porous microspheres with an efficient 3D conductive network for high performance lithium-sulfur batteries. *J Mater Chem A* **2016,** *4*, 775-780.
193. Ding, Y. L.; Kopold, P.; Hahn, K.; van Aken, P. A.; Maier, J.; Yu, Y., Facile Solid-State Growth of 3D Well-Interconnected Nitrogen-Rich Carbon Nanotube-Graphene Hybrid Architectures for Lithium-Sulfur Batteries. *Adv Funct Mater* **2016,** *26*, 1112-1119.
194. Wu, Y. S.; Xu, C. M.; Guo, J. X.; Su, Q. M.; Du, G. H.; Zhang, J., Enhanced electrochemical performance by wrapping graphene on carbon nanotube/sulfur composites for rechargeable lithium-sulfur batteries. *Mater Lett* **2014,** *137*, 277-280.
195. Jeong, Y. C.; Lee, K.; Kim, T.; Kim, J. H.; Park, J.; Cho, Y. S.; Yang, S. J.; Park, C. R., Partially unzipped carbon nanotubes for high-rate and stable lithium-sulfur batteries. *J Mater Chem A* **2016,** *4*, 819-826.

196. Jin, C.; Zhang, W.; Zhuang, Z.; Wang, J.; Huang, H.; Gan, Y.; Xia, Y.; Liang, C.; Zhang, J.; Tao, X., Enhanced sulfide chemisorption using boron and oxygen dually doped multi-walled carbon nanotubes for advanced lithium–sulfur batteries. *J. Mater. Chem. A* **2016**, DOI: 10.1039/C6TA07620C.
197. Yu, M.; Ma, J.; Song, H.; Wang, A.; Tian, F.; Wang, Y.; Qiu, H.; Wang, R., Atomic layer deposited TiO 2 on a nitrogen-doped graphene/sulfur electrode for high performance lithium–sulfur batteries. *Energ Environ Sci* **2016,** *9*, 1495-1503.
198. Deng, W. N.; Hu, A. P.; Chen, X. H.; Zhang, S. Y.; Tang, Q. L.; Liu, Z.; Fan, B. B.; Xiao, K. K., Sulfur-impregnated 3D hierarchical porous nitrogen-doped aligned carbon nanotubes as high-performance cathode for lithium-sulfur batteries. *Journal of Power Sources* **2016,** *322*, 138-146.
199. Maschmann, M. R.; Ehlert, G. J.; Dickinson, B. T.; Phillips, D. M.; Ray, C. W.; Reich, G. W.; Baur, J. W., Bioinspired Carbon Nanotube Fuzzy Fiber Hair Sensor for Air-Flow Detection. *Adv Mater* **2014,** *26*, 3230–3234.
200. Maschmann, M. R.; Dickinson, B.; Ehlert, G. J.; Baur, J. W., Force sensitive carbon nanotube arrays for biologically inspired airflow sensing. *Smart Mater Struct* **2012,** *21*, 094024.
201. Amama, P. B.; Pint, C. L.; Kim, S. M.; McJilton, L.; Eyink, K. G.; Stach, E. A.; Hauge, R. H.; Maruyama, B., Influence of Alumina Type on the Evolution and Activity of Alumina-Supported Fe Catalysts in Single-Walled Carbon Nanotube Carpet Growth. *Acs Nano* **2010,** *4*, 895-904.
202. Amama, P. B.; Pint, C. L.; Mirri, F.; Pasquali, M.; Hauge, R. H.; Maruyama, B., Catalyst-support interactions and their influence in water-assisted carbon nanotube carpet growth. *Carbon* **2012,** *50*, 2396-2406.
203. Park, J.; Moon, J.; Kim, C.; Kang, J. H.; Lim, E.; Park, J.; Lee, K. J.; Yu, S.-H.; Seo, J.-H.; Lee, J., Graphene quantum dots: structural integrity and oxygen functional groups for high sulfur/sulfide utilization in lithium sulfur batteries. *NPG Asia Mater.* **2016,** *8*, e272.
204. Gu, X. X.; Tong, C. J.; Wen, B.; Liu, L. M.; Lai, C.; Zhang, S. Q., Ball-milling synthesis of ZnO@sulphur/carbon nanotubes and Ni (OH)(2)@sulphur/carbon nanotubes composites for high-performance lithium-sulphur batteries. *Electrochim Acta* **2016,** *196*, 369-376.
205. Hu, G. J.; Xu, C.; Sun, Z. H.; Wang, S. G.; Cheng, H. M.; Li, F.; Ren, W. C., 3D Graphene-Foam-Reduced-Graphene-Oxide Hybrid Nested Hierarchical Networks for High-Performance Li-S Batteries. *Adv Mater* **2016,** *28*, 1603-1609.
206. Jin, F. Y.; Xiao, S.; Lu, L. J.; Wang, Y., Efficient Activation of High-Loading Sulfur by Small CNTs Confined Inside a Large CNT for High-Capacity and High-Rate Lithium-Sulfur Batteries. *Nano Lett* **2016,** *16*, 440-447.
207. Li, G.; Sun, J. H.; Hou, W. P.; Jiang, S. D.; Huang, Y.; Geng, J. X., Three-dimensional porous carbon composites containing high sulfur nanoparticle content for high-performance lithium-sulfur batteries. *Nat Commun* **2016,** *7*, 10601.
208. Lv, D. P.; Zheng, J. M.; Li, Q. Y.; Xie, X.; Ferrara, S.; Nie, Z. M.; Mehdi, L. B.; Browning, N. D.; Zhang, J. G.; Graff, G. L., et al., High Energy Density Lithium-Sulfur Batteries: Challenges of Thick Sulfur Cathodes. *Adv Energy Mater* **2015,** *5*, 1402290.

209. Yang, X. F.; Yu, Y.; Yan, N.; Zhang, H. Z.; Li, X. F.; Zhang, H. M., 1-D oriented cross-linking hierarchical porous carbon fibers as a sulfur immobilizer for high performance lithium-sulfur batteries. *J Mater Chem A* **2016,** *4*, 5965-5972.
210. Liang, X.; Rangom, Y.; Kwok, C. Y.; Pang, Q.; Nazar, L. F., Interwoven MXene Nanosheet/Carbon-Nanotube Composites as Li–S Cathode Hosts. *Adv. Mater.* **2016,** *29*, 1603040.
211. Wu, F.; Ye, Y.; Chen, R.; Zhao, T.; Qian, J.; Zhang, X.; Li, L.; Huang, Q.; Xuedong, B.; Cui, Y., Gluing Carbon Black and Sulfur at Nanoscale: A Polydopamine-Based "Nano-Binder" for Double-Shelled Sulfur Cathodes. *Adv. Energy Mater.* **2017,** *7*, 1601591.
212. Lu, X. C.; Xia, G. G.; Lemmon, J. P.; Yang, Z. G., Advanced materials for sodium-beta alumina batteries: Status, challenges and perspectives. *Journal of Power Sources* **2010,** *195*, 2431-2442.
213. Kohl, M.; Borrmann, F.; Althues, H.; Kaskel, S., Hard Carbon Anodes and Novel Electrolytes for Long-Cycle-Life Room Temperature Sodium-Sulfur Full Cell Batteries. *Adv Energy Mater* **2016,** *6*, 201502185.
214. Yu, X. W.; Manthiram, A., Ambient-Temperature Sodium-Sulfur Batteries with a Sodiated Nafion Membrane and a Carbon Nanofiber-Activated Carbon Composite Electrode. *Adv Energy Mater* **2015,** *5*, 201500350.
215. Yu, X. W.; Manthiram, A., Performance Enhancement and Mechanistic Studies of Room-Temperature Sodium-Sulfur Batteries with a Carbon-Coated Functional Nafion Separator and a Na2S/Activated Carbon Nanofiber Cathode. *Chem Mater* **2016,** *28*, 896-905.
216. Yu, X. W.; Manthiram, A., Na2S-Carbon Nanotube Fabric Electrodes for Room-Temperature Sodium-Sulfur Batteries. *Chem-Eur J* **2015,** *21*, 4233-4237.
217. Ryu, H.; Kim, T.; Kim, K.; Ahn, J. H.; Nam, T.; Wang, G.; Ahn, H. J., Discharge reaction mechanism of room-temperature sodium-sulfur battery with tetra ethylene glycol dimethyl ether liquid electrolyte. *Journal of Power Sources* **2011,** *196*, 5186-5190.
218. Kim, I.; Park, J. Y.; Kim, C.; Park, J. W.; Ahn, J. P.; Ahn, J. H.; Kim, K. W.; Ahn, H. J., Sodium Polysulfides during Charge/Discharge of the Room-Temperature Na/S Battery Using TEGDME Electrolyte. *Journal of the Electrochemical Society* **2016,** *163*, A611-A616.
219. Hwang, T. H.; Jung, D. S.; Kim, J. S.; Kim, B. G.; Choi, J. W., One-Dimensional Carbon-Sulfur Composite Fibers for Na-S Rechargeable Batteries Operating at Room Temperature. *Nano Lett* **2013,** *13*, 4532-4538.
220. Bauer, I.; Kohl, M.; Althues, H.; Kaskel, S., Shuttle suppression in room temperature sodium-sulfur batteries using ion selective polymer membranes. *Chem Commun* **2014,** *50*, 3208-3210.
221. Wenzel, S.; Metelmann, H.; Raiss, C.; Durr, A. K.; Janek, J.; Adelhelm, P., Thermodynamics and cell chemistry of room temperature sodium/sulfur cells with liquid and liquid/solid electrolyte. *Journal of Power Sources* **2013,** *243*, 758-765.
222. Jeong, G.; Kim, H.; Lee, H. S.; Han, Y. K.; Park, J. H.; Jeon, J. H.; Song, J.; Lee, K.; Yim, T.; Kim, K. J., et al., A room-temperature sodium rechargeable battery using an SO2-based nonflammable inorganic liquid catholyte. *Sci Rep-Uk* **2015,** *5*, 12827
223. Wang, J. L.; Yang, J.; Nuli, Y.; Holze, R., Room temperature Na/S batteries with sulfur composite cathode materials. *Electrochem Commun* **2007,** *9*, 31-34.

224. Lee, D. J.; Park, J. W.; Hasa, I.; Sun, Y. K.; Scrosati, B.; Hassoun, J., Alternative materials for sodium ion-sulphur batteries. *J Mater Chem A* **2013,** *1*, 5256-5261.
225. Kim, I.; Kim, C. H.; Choi, S. H.; Ahn, J. P.; Ahn, J. H.; Kim, K. W.; Cairns, E. J.; Ahn, H. J., A singular flexible cathode for room temperature sodium/sulfur battery. *Journal of Power Sources* **2016,** *307*, 31-37.
226. Scherdel, C.; Reichenauer, G., Microstructure and morphology of porous carbons derived from sucrose. *Carbon* **2009,** *47*, 1102-1111.
227. Guo, P. Z.; Gu, Y.; Lei, Z. B.; Cui, Y. Q.; Zhao, X. S., Preparation of sucrose-based microporous carbons and their application as electrode materials for supercapacitors. *Micropor Mesopor Mat* **2012,** *156*, 176-180.
228. Li, Z.; Yuan, L. X.; Yi, Z. Q.; Sun, Y. M.; Liu, Y.; Jiang, Y.; Shen, Y.; Xin, Y.; Zhang, Z. L.; Huang, Y. H., Insight into the Electrode Mechanism in Lithium-Sulfur Batteries with Ordered Microporous Carbon Confined Sulfur as the Cathode. *Adv Energy Mater* **2014,** *4*, 201301473.
229. Kim, H.; Hong, J.; Yoon, G.; Kim, H.; Park, K. Y.; Park, M. S.; Yoon, W. S.; Kang, K., Sodium intercalation chemistry in graphite. *Energ Environ Sci* **2015,** *8*, 2963-2969.